

Epitaxy of ultrathin nickel ferrite films on MgO(001) and SrTiO₃(001)

Masterarbeit vorgelegt im Rahmen der Prüfung
für den Master-Studiengang Materialwissenschaften

Matrikel-Nummer: 953851
Osnabrück, 20. Oktober 2016

Autor: Tabea NORDMANN

Erstprüfender: Prof. Dr. Joachim WOLLSCHLÄGER

Zweitprüfender: Dr. Karsten KÜPPER

Zusammenfassung

Innerhalb dieser Arbeit wird das Wachstum von ultradünnen $\text{Ni}_x\text{Fe}_{3-x}\text{O}_4$ ($0 < x < 1$) Filmen auf $\text{MgO}(001)$ untersucht, um die Parameter für die Herstellung von stöchiometrischen Nickelferritfilmen (NiFe_2O_4) zu finden. Im zweiten Teil der Arbeit wird das Wachstum von stöchiometrischem Nickelferrit auf $\text{SrTiO}_3(001)$ für verschiedene Schichtdicken analysiert.

Die Filme werden durch gleichzeitiges Verdampfen von Eisen und Nickel in einer Sauerstoffatmosphäre von 5×10^{-6} mbar und bei einer Substrattemperatur von 250°C präpariert. Das verwendete Verfahren ist die reaktive Molekularstrahlepitaxie. Das $\text{Ni}/(\text{Fe}+\text{Ni})$ -Verhältnis wird durch die Anpassung der Leistungen der beiden Effusionszellen variiert. Insgesamt werden fünfzehn Filme auf MgO hergestellt, deren $\text{Ni}/(\text{Fe}+\text{Ni})$ -Verhältnisse zwischen 7 % und 60 % liegen und fünf Filme auf SrTiO_3 mit $\text{Ni}/(\text{Fe}+\text{Ni})$ -Verhältnissen zwischen 27 % und 33 % und Schichtdicken zwischen 5 nm und 60 nm. Für alle Filme werden LEED-, XPS-, XRR- und XRD-Messungen durchgeführt.

Die Ergebnisse der LEED-Messungen zeigen für alle Filme ein scharfes (1×1) Beugungsmuster, sodass die Ordnung der Filme an der Oberfläche sehr gut ist. Die Schärfe der Reflexe von den Filmen auf dem Substrat SrTiO_3 , und damit die Ordnung an der Oberfläche, steigt mit zunehmender Schichtdicke.

Für die Untersuchung des Wachstums von $\text{Ni}_x\text{Fe}_{3-x}\text{O}_4$ ($0 < x < 1$) auf MgO haben die XPS Messungen die größte Bedeutung, da die Auswertung der $\text{Fe}3p$ und $\text{Ni}3p$ Spektren die $\text{Ni}/(\text{Fe}+\text{Ni})$ -Verhältnisse und die $\text{Fe}2p$, $\text{Ni}3s$ und $\text{Fe}3s$ Spektren Informationen bezüglich der Oxidationszustände von Eisen und Nickel in den Filmen liefern. Ab einem $\text{Ni}/(\text{Fe}+\text{Ni})$ -Gehalt von 32 % zeigen die Ergebnisse, dass nur Fe^{3+} -Ionen existieren, wie es in stöchiometrischem Nickelferrit sein sollte. Für kleinere Verhältnisse enthalten die Filme sowohl Fe^{3+} -Ionen als auch Fe^{2+} -Ionen und ähneln mit abnehmendem $\text{Ni}/(\text{Fe}+\text{Ni})$ -Gehalt immer mehr dem strukturell gleich aufgebauten Eisenoxid Magnetit. Der Oxidationszustand des Nickels ändert sich für verschiedene $\text{Ni}/(\text{Fe}+\text{Ni})$ -Verhältnisse nicht.

Nach Aussage der XRD- und XRR-Messungen von drei Filmen auf MgO mit $\text{Ni}/(\text{Fe}+\text{Ni})$ -Verhältnissen zwischen 53 % und 60 % bestehen die Filme aus einer einzelnen vollständig kristallinen Schicht und haben einen vertikalen Lagenabstand von 2.07 \AA , der somit 0.7 % kleiner ist als der Lagenabstand von 2.085 \AA im Volumenmaterial [1]. Diese Stauchung in vertikaler Richtung passt zu der Gitterfehlpassung von 1 % zwischen den beiden Materialien, die unter der Annahme von pseudomorphem Wachstums zu einer Dehnung des nicht-auxetischen Nickelferrits in lateraler Richtung führt.

Die Ergebnisse der XPS-Messungen von den Filmen auf SrTiO_3 bestätigen, dass Eisen nur im 3+ Oxidationszustand vorliegt. Aufgrund der relativ großen Gitterfehlpassung von -7 % zwischen SrTiO_3 und NiFe_2O_4 liegt der Schwerpunkt der Messungen auf der Aufklärung struktureller Unterschiede zwischen den verschiedenen Schichtdicken und damit auf den XRD-Messungen. Basierend auf der Gitterfehlpassung würde man pseudomorphes Wachstum der Filme mit einer Stauchung in lateraler Richtung und kompensierend eine Dehnung in vertikaler Richtung erwarten. Im Gegensatz dazu ergeben die XRD-Messungen eine Stauchung in vertikaler Richtung, sodass die Annahme des pseudomorphen Wachstums der Filme auf SrTiO_3 in Frage gestellt werden muss. Für eine Schichtdicke von

5 nm resultiert ein vertikaler Lagenabstand von 2.07 \AA , der mit zunehmender Schichtdicke ansteigt und bei 60 nm Schichtdicke 2.0875 \AA beträgt. Der letzte Wert ist geringfügig größer als der Lagenabstand von 2.085 \AA im Volumenmaterial von Nickelferrit. Das Ergebnis kann dadurch erklärt werden, dass das Ni/(Fe+Ni)-Verhältnis des 60 nm Films bei 28 % liegt und damit die Zusammensetzung in Richtung des Eisenoxids Magnetits verschoben ist, dessen Lagenabstand 2.0975 \AA beträgt. Zusätzlich zum schichtdickenabhängigen vertikalen Lagenabstand wird die Halbwertsbreite (FWHM) der Film-Bragg-Peaks verglichen. Diese nimmt nicht-linear mit zunehmender Schichtdicke ab und deutet darauf hin, dass die Verteilung des vertikalen Lagenabstands schmaler, die Kristallinität in vertikale Richtung mit zunehmender Schichtdicke dementsprechend besser wird.

Die nächsten Schritte sind die Präparation von Nickelferrit Filmen auf SrTiO_3 mit Schichtdicken unterhalb von 5 nm und XRD- und Grazing Incidence XRD-Messungen am Synchrotron für alle Schichtdicken um Informationen über die Struktur der Filme in vertikale und laterale Richtung zu erhalten. Anschließend wird der Fokus der Messungen auf der Charakterisierung der magnetischen Eigenschaften der Filme liegen. Für einen Vergleich der Qualität der mittels RMBE hergestellten Filme mit anderen Präparationstechniken sind außerdem Untersuchungen bezüglich der elektrischen Leitfähigkeit, der Morphologie und der Grenzflächeneigenschaften der Filme notwendig, sodass die Durchführung von VSM, AFM und TEM sinnvoll wäre.

Contents

1. Introduction	1
2. Theoretical background	5
2.1. Crystal structure	5
2.2. RMBE - Reactive molecular beam epitaxy	7
2.3. XRR - X-ray reflectometry	8
2.4. LEED - Low-energy electron diffraction	11
2.5. XPS - X-ray photoelectron spectroscopy	13
2.5.1. Principle	13
2.5.2. Quantitative analysis	14
2.5.3. Spectral features	15
2.6. XRD - X-ray diffraction	19
2.6.1. Principle	19
2.6.2. Bragg peaks	20
3. Investigated materials	25
3.1. Magnesium oxide - MgO	25
3.2. Strontium titanate - SrTiO ₃	26
3.3. Nickel ferrite - NiFe ₂ O ₄	26
4. Experimental setup and sample preparation	29
4.1. Experimental setup of the ultrahigh vacuum system	29
4.1.1. Low-energy electron diffraction	30
4.1.2. X-ray photoelectron spectroscope	31
4.2. X-ray diffractometer	32
4.3. Sample preparation	33
5. Results and discussion of Ni_xFe_{3-x}O₄ (0 < x < 1) films grown on MgO	37
5.1. XPS results	37
5.1.1. Quantitative analysis of the Fe3p and Ni3p peaks	37
5.1.2. Analysis of the Fe2p peak	40
5.1.3. Analysis of the Fe3s peak	44
5.2. LEED results	47
5.3. XRR-Results	49
5.4. XRD results	50
5.4.1. Analysis of the data	50
5.4.2. (002)- and (004)-reflexes	50
5.5. Discussion	53

6. Results and discussion of NiFe₂O₄ films grown on SrTiO₃	57
6.1. XPS results	57
6.2. LEED results	59
6.3. XRR results	60
6.4. XRD results	61
6.5. Discussion	64
7. Conclusion	67
Bibliography	69
A. Appendix	73
A.0.1. XRR data NiFe ₂ O ₄ on MgO	73
A.0.2. XRR data NiFe ₂ O ₄ on STO	73

1. Introduction

In a high developed performance society efficient energy recovery is a topic of significant social relevance. Thermoelectric power generation is often based on the Seebeck effect which is the generation of an electrical voltage due to a temperature gradient [2]. During the last years the research field spintronics and spin calitronics intensified and the spin Seebeck effect (SSE) was observed in magnets where a temperature gradient results in a spin voltage [3].

A promising opportunity to convert wasted omnipresent heat into electricity by utilization of the spin Seebeck effect (SSE) and the inverse spin Hall effect (ISHE) reveals great scientific interest in the research of materials exhibiting these outstanding thermoelectrical effects [4], [5].

Under suitable conditions the spin voltage originating from the SSE can be converted into a charge voltage by the ISHE [6]. Depending on the device structure a transversal and a longitudinal spin Seebeck effect (TSSE and LSSE) can be measured [7]. Because the transversal arrangement where the spin current is aligned perpendicular to the temperature gradient bears the occurrence of parasitic effects like the anomalous Nernst effect (ANE) and the planar Nernst effect (PNE) the longitudinal device construction is favored due to its simplicity in design [6]. The lower the thermal conductivity κ and the electrical resistivity ρ of the used material are, the higher is the efficiency of the thermoelectric generation based on the spin Seebeck effect. The Wiedemann-Franz law ($\kappa_e \rho = l_e T$, with the electronic lorentz number l_e and the absolute temperature T) disables a low thermal conductivity and low electrical resistivity at the same time for a one material system if the thermal conductivity of the material is determined by the electronic contribution κ_e [6].

Using a bilayer system enables the possibility to optimize the requirements for an efficient use of the thermoelectric generation based on the LSSE.

A system consisting of a high quality insulating magnetic layer with a low thermal conductivity and a metal with a low electrical resistivity is promising for an efficient device converting heat into electricity since κ and ρ are freely selectable from the point of the Wiedemann-Franz law [6]. The construction described prior is illustrated in figure 1.1.

Perpendicular to the metal/insulator interface the temperature gradient induced by a heat bath points in z-direction and so the spin current resulting from the LSSE is directed in z-direction as well. In case of soft ferrimagnets an external field H is necessary to align the magnetization in x-direction. The driving force of the process are temperature induced collective excitations of localized magnetic moments in the magnetic insulator. These so called magnons interact with conduction-electron spins in the attached metal and the spin angular momentum is transferred across the interface via s-d exchange interaction [6]. The conduction-electron spin current is converted into a charge current and thereby into an electrical field via the mentioned ISHE. The film thickness has to be in the range of its spin diffusion length since the spin current and the associated electrical

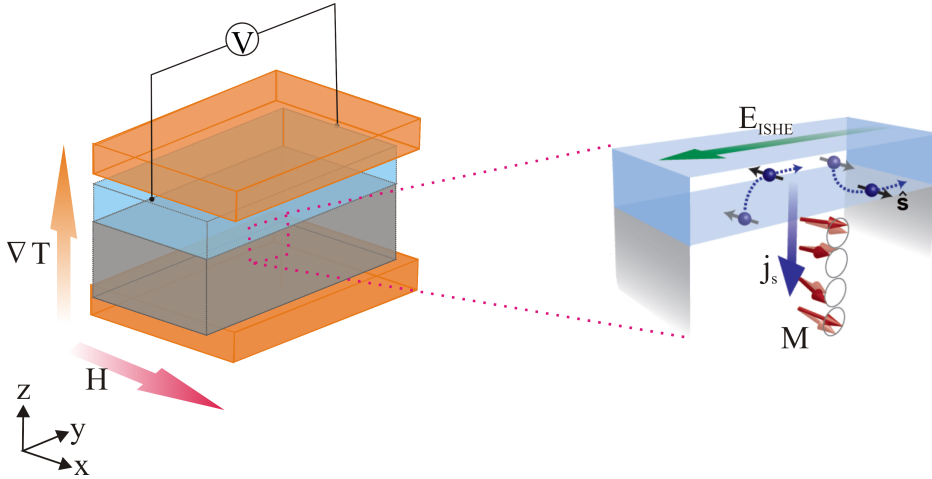


Figure 1.1.: Construction of a thermoelectric device to convert heat into electricity. The magnetic insulator (grey) and the metallic film (blue) are sandwiched by a heat bath (orange) to apply a temperature gradient perpendicular to the metal/insulator interface. An external magnetic field is used to align the magnetic moments along the x-direction in case of soft ferrimagnets. The heat difference generates a spin current j_s parallel to the temperature gradient due to the LSSE. At the interface between the magnetic insulator (often a ferrimagnet) and the metal a spin-angular transfer takes place and inside the metal close to the interface the spin current coming from the spin transfer induces a charge voltage E_{ISHE} originating from the ISHE. Taken and adapted from [6].

field just exist in vicinity to the metal/insulator interface because of spin relaxation [6]. The described thermoelectrical mechanism works up to the Curie temperature T_C of the magnetic insulator. For higher temperatures the ferri- or ferromagnetic insulator becomes paramagnetic and the well ordered arrangement of the magnetic moments and thereby the clearly orientated spin current disappear.

The efficiency of the whole process is determined by the efficiency of the two spin effects and the spin angular transfer efficiency across the interface which is highly influenced by the quality of the crystalline structure and the density of magnetic moments at the interface. Furthermore, the output of the device depends on its size since it has a convenient scaling capability where the value of the temperature induced spin current simply increases with increasing interface area.

Nickel ferrite is a promising material for the use as magnetic insulator layer, because it has a high magnetic permeability, a low electrical conductance and a high Curie temperature of 865 K [8] which enables the applicability up to nearly 600 °.

To reach the aim of an economic recovery of electric energy from wasted heat via LSSE and ISHE fundamental research on the growth of suitable materials like stoichiometric nickel ferrite has to be performed in order to enable the deposition of high quality films with perfect interface properties. In order to use the full capacity of nickel ferrite inside a thermoelectrical device detailed information about different growth methods and the resulting interface and long lasting periodicity properties have to be gained.

Apart from the aspect of thermoelectrical applications ferrite thin films are convenient for

the use in computer memory chips, magnetic recording media, high-frequency microwave devices and frequency filters [9], [10]. As a soft ferrite material [11] nickel ferrite is interesting for the further integration of various passive circuit elements in communication devices working in the microwave range [12].

Studies on the growth of nickel ferrite by several deposition techniques, all having advantages and disadvantages, have already been performed [10]. The growth with pulsed laser deposition (PLD) is widely studied since it exhibits a simple control of the stoichiometry of the films, but it is not applicable for the industrial process due to the small deposition area. Liquid-phase epitaxy has a high deposition rate and area but the films often show inhomogeneities and have a poor surface morphology [1]. Chemical vapor deposition (CVD) has several advantages for the growth of nickel ferrite like relatively high growth rates and large deposition areas but it's difficult to find suitable metal precursors which exhibit a high volatility and thermal stability at the same time [1]. Furthermore, the accurate control of the vapor concentrations for the two metallic components is hard to realize often leading to impurities such as Fe_2O_3 and NiO [13]. Several deposition techniques require post-annealing steps to obtain well structured nickel ferrite thin films with soft magnetic properties [10] which is undesirable for electric circuit integration.

The growth of nickel ferrite by using reactive molecular beam epitaxy (RMBE) has just been studied rarely even though it provides films with a very high crystalline quality as for example for the quite similar structured iron oxide magnetite [14]. The aim of this work is the co-evaporation of nickel and iron in an oxygen atmosphere by using RMBE in order to deposit stoichiometric films of nickel ferrite. Afterwards further work can be done on the optimization of the interface properties. The substrates used in this work are magnesium oxide (001) (MgO) and Nb doped strontium titanate (001) (SrTiO_3 , STO). $\text{MgO}(001)$ exhibits a small lattice mismatch of less than 1% with nickel ferrite indicating the successful growth of nickel ferrite on it. It is used to vary the $\text{Ni}/(\text{Fe}+\text{Ni})$ ratio to find the optimal growth conditions. Next the less fitting substrate STO is used which is a more interesting substrate for nickel ferrite with respect to its magnetic properties [15].

The methods used to characterize the grown films are low-energy electron diffraction (LEED) to classify the level of order and the structure at the surface, x-ray photoelectron spectroscopy (XPS) to determine the film composition and the oxidation state and the chemical surrounding of iron and nickel, x-ray diffraction (XRD) and grazing incidence x-ray diffraction (GIXRD) to qualify the crystalline quality in the bulk material of the film and to quantify the out-of-plane lattice constant and x-ray reflectivity (XRR) to examine the film thickness and its roughness. XPS and LEED are performed in-situ while the other measurements are performed ex-situ at the Universität Bielefeld and the Deutsches Elektronen Synchrotron (DESY) in Hamburg.

Theoretical foundations essential for this thesis are given in chapter 2 while the investigated materials are presented in chapter 3. In chapter 4 the experimental setup and the sample preparation are described. The presentation, analysis and discussion of the experimental results follow in chapter 5 and 6 before the thesis is completed with a conclusion and prospects for further experiments in chapter 7.

2. Theoretical background

This chapter serves as introduction into the theoretical basics concerning the present thesis. First, in chapter 2.1, the notation of crystal structures and the heteroepitaxial growth of thin films are illustrated. Then, in chapter 2.2, the thin film deposition technique reactive molecular beam epitaxy (RMBE) is described. In chapter 2.3, x-ray reflectometry (XRR) is explained which reveals information about the thickness and the roughness of the prepared films. In the next chapter 2.4 low-energy electron diffraction (LEED) and its means for the characterization of the surface structure of crystalline materials is stated. The basics of x-ray photoelectron spectroscopy (XPS) are described in chapter 5.1. XPS is utilized to examine the electronic structure of the occupied states in the surface near region and to determine the stoichiometric composition of the films. With x-ray diffraction (XRD), explained in chapter 2.6, the structure of the films is analyzed in out-of-plane direction.

2.1. Crystal structure

An ideal crystal is defined as an infinite repetition of identical arrangements of atoms. The structure of an ideal crystal is described in terms of a lattice and a basis.

The lattice is defined by three primitive translation vectors \vec{a} , \vec{b} and \vec{c} in a way that the arrangement of the atoms of the crystal looks exactly the same for the observation from point r and point r' , where n , m and k are integers. The set of points r' that fulfil the equation $\vec{r}' = \vec{r} + n\vec{a} + m\vec{b} + k\vec{c}$ define the lattice.

The lattice is just a mathematical construction which turns into a crystal structure when a basis consisting of a single atom or a group of atoms is attached to every lattice point. Thereby the basis is always identical in its composition, arrangement and orientation. The position of the center of an atom j of the basis relative to the associated lattice point is

$$\vec{r}_j = x_j\vec{a} + y_j\vec{b} + z_j\vec{c}, \quad (2.1)$$

where $0 \leq x_j, y_j, z_j \leq 1$.

The three primitive translation vectors generate a parallelepiped which is called primitive unit cell. The primitive unit cell of a crystal structure contains exactly one lattice point and the gapless concatenation of these cells leads to the crystal structure. In figure 2.1 a three-dimensional lattice with the yellow primitive unit cell generated by the three primitive translation vectors is illustrated.

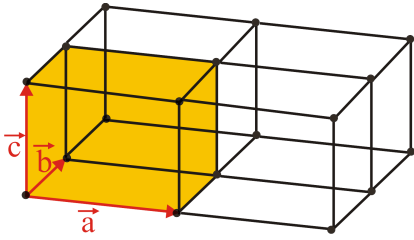


Figure 2.1.: Three-dimensional crystal lattice with a primitive unit cell (in yellow) generated by the three primitive translation vectors \vec{a} , \vec{b} and \vec{c}

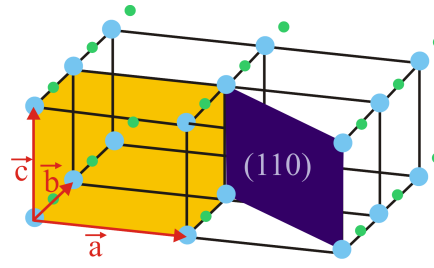


Figure 2.2.: Three-dimensional crystal structure with a diatomic basis (blue and green) which is located at every lattice point. The purple plane is the crystal plane with the Miller indices (110).

The choice of the primitive translation vectors and the basis is ambiguous. There are several primitive and non-primitive unit cells where the first mentioned are minimum volume cells which contain just one lattice point and all equivalent lattice points can be reached through the associated primitive translation vectors. The non-primitive unit cells can contain several lattice points and not all equivalent lattice points can be approached by their translation vectors. 14 different lattices exist in three dimensions.

In order to specify crystal planes the description using Miller indices has proved to be successful. The plane which orientation has to be described is given by three non-collinear points in the plane. The intercepts of the plane with the axes in terms of the translation vectors \vec{a} , \vec{b} and \vec{c} result in three numbers which lead to the indices. The reduced three integers having the same ratio as the reciprocal of the three numbers are the Miller indices (hkl) which describe the orientation of the plane with respect to the origin of the lattice. For an intercept at infinity the corresponding index is zero. If a plane intercepts with the axis on the negative side of the origin, the corresponding index is negative and gets a minus sign above the index $(h\bar{k}l)$. In figure 2.2 the (110)-plane is indicated in purple. In order to describe directions inside a crystal the direction vector is expressed by indices in square brackets, $[hkl]$. Those indices are the set of the smallest integers that have the ratio of the components of a vector, associated to the axis of the crystal. Here, too, the negative component of a direction vector is indicated by a minus located above the index, $[\bar{h}kl]$.

Crystalline surfaces and interfaces are in principal three-dimensional because they have a certain thickness but all symmetry properties are two-dimensional because the surface structure is periodic only in two directions. The description of the lattice and the basis are therefore reduced to two dimensions with the translation vectors \vec{a} and \vec{b} :

$$\vec{r}' = \vec{r} + n\vec{a} + m\vec{b} \qquad \vec{r}'_j = x_j\vec{a} + y_j\vec{b}. \qquad (2.2)$$

The number of possible lattices reduces to five in two dimensions.

Further information can be found in references [16] and [17].

Heteroepitaxial growth of thin films

Epitaxial growth of a thin film on a crystalline substrate is present when the deposited crystalline film has a well-defined orientation with respect to the crystal structure of the substrate. Homoepitaxy is the well-orientated growth of a material on a substrate of the

same material whereas heteroepitaxy describes the epitaxial growth of a material on a substrate consisting of a different material. It's unlikely that both materials have the same lattice constant so in most cases the lattices don't match and there is a lattice misfit ϵ between the two materials which is defined as the relative difference of the materials lattice constants:

$$\epsilon = \frac{a - b}{a}, \quad (2.3)$$

here a is the lattice constant of the substrate material and b the one of the film material. In case of a relatively small lattice misfit the film grows deformed in a way that the elastically strained film adopts the periodicity of the substrate at the interface. Often the lattice constant of the film perpendicular to the interface is distorted to preserve the volume of the unit cell. This kind of growth is called pseudomorphic growth. Large lattice misfits lead to the occurrence of strain relieving dislocations at the film/substrate interface. In order to predict which mechanism dominates in a specific case the free energy densities associated with the two mechanisms have to be considered. The different growth modes for heteroepitaxial growth of thin films are sketched in figure 2.3.

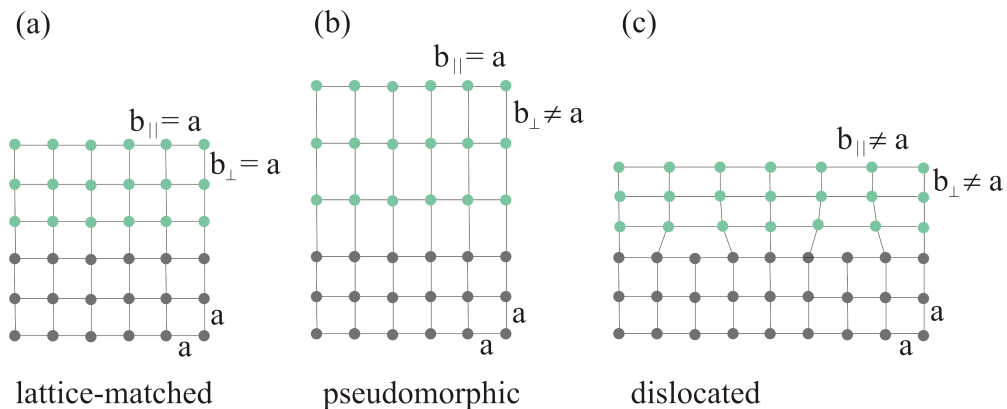


Figure 2.3.: Heteroepitaxial growths modes: (a) lattice-matched growth; (b) strained pseudomorphic growth; (c) relaxed dislocated growth. Taken from [18].

The information of this chapter are based on reference [18].

2.2. RMBE - Reactive molecular beam epitaxy

Reactive molecular beam epitaxy is a method for thin oxide film deposition of single crystals. The molecular beam epitaxy of the pure cation material takes place in an oxygen atmosphere to obtain the oxide of the material. To avoid impurities inside the films the deposition has to happen at a very low background pressure. A pressure of 10^{-6} mbar already leads to a contamination with impurity atoms within a few seconds. So a background pressure of at least 10^{-8} mbar is recommended.

The molecular beam is generated in an effusion cell where a current carrying filament emits electrons. Between this filament and a rod consisting of the cation material a positive high

voltage is applied in order to accelerate the electrons on the rod. The driving in electrons lead to a heating and thereby to a sublimation of the rod atoms and an emission current can be measured between the filament and the rod. Two apertures focus the molecular beam on the sample where the material condenses. For quantification of the evaporated amount a crystal oscillator is mounted behind the second aperture. The oscillator becomes heavier during evaporation so that its oscillations frequency drops. Since the frequency changes are small compared to the start frequency of the oscillator a proportional relation between the change of the frequency and the mass is assumed. After a calibration with a method to measure the film thickness the frequency change serves as prediction of the film thickness. A shutter mounted behind the second aperture can be used to screen the sample from the molecular beam. The setup of an effusion cell is depicted in figure 2.4.

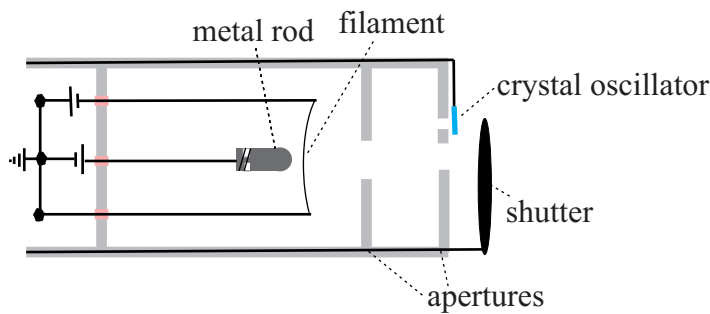


Figure 2.4.: Setup of an effusion cell used for molecular beam epitaxy. A current-carrying filament emits electrons which are accelerated on a projectile constituted of the material to be evaporated. The projectile heats up and its atoms are sublimated and adsorbed on the sample after they have passed through the apertures. The purpose of the crystal oscillator is to quantify the evaporated amount.

2.3. XRR - X-ray reflectometry

X-ray reflectometry (XRR) utilizes the interference of reflected x-rays to determine non-destructively the thickness of thin films and the surface and interface roughness.

The x-rays strike the sample at an incidence angle $\alpha_i \leq 5^\circ$. Against the convention of many diffraction experiments the angle of incidence in this case is the angle between the incoming beam and the surface of the sample (compare figure 2.10). In dependence of the incidence angle the intensity of the reflected x-rays is measured at the angle of reflection $\alpha_r = \alpha_i$.

The reflectivity of a material depends on the complex index of refraction n which is for x-rays constituted by

$$n = 1 - \delta + i\beta. \tag{2.4}$$

The dispersion δ and the absorption β of a material are between 10^{-6} and 10^{-5} for x-rays. A marginal difference between the two refraction indices of the materials of the substrate and the film are made of is the condition for the determination of the film thickness. A difference in the refraction index goes along with a variation in the electron density.

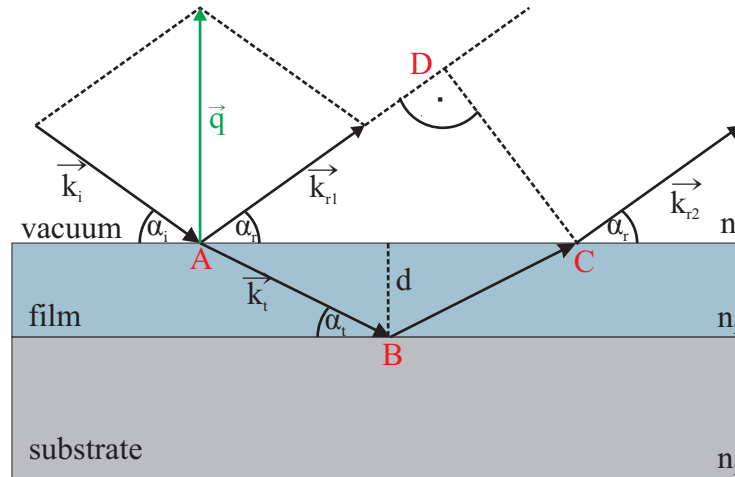


Figure 2.5.: An incoming wave (\vec{k}_i) strikes the sample at the angle α_i , is partly reflected and partly transmitted at the two interfaces (vacuum/film and film/substrate). At the reflection angle $\alpha_r = \alpha_i$ the total reflected radiation is detected. The scattering vector \vec{q} is orientated in the direction of the surface normal.

For small incidence angles occurs total reflection up to a critical angle α_c . The critical angle can be approximated for known materials by using Snell's law:

$$\alpha_c \approx \sqrt{2\delta} \quad (2.5)$$

For incidence angles higher than the critical angle parts of the x-rays penetrate in the material, are reflected at the interface between substrate and film and interfere with the leftover x-rays which have been reflected directly at the interface between vacuum and film.

The path difference Δs of both beams (compare figure 2.10) is

$$\Delta s = n_2 \cdot (\overline{AB} + \overline{BC}) - n_1 \cdot \overline{AD}. \quad (2.6)$$

The refraction indices of different materials are nominal for x-rays so that with these assumption ($n_1 \approx n_2 \approx 1$) the phenomenon of diffraction at the interface during the transmission can be neglected. The path difference then simplifies from geometrical considerations (compare figure 2.10):

$$\Delta s \approx 2 \cdot d \cdot \sin(\alpha_i). \quad (2.7)$$

Here d is the thickness of the film.

Depending on the incidence angle α_i the x-rays interfere constructive or destructive with the result that oscillations exist for the notation of the intensity against the incidence angle.

For two neighboring intensity maxima which occur at the incidence angles $\alpha_{i,m}$ and $\alpha_{i,n}$ the path difference is equivalent to the wave length λ of the used x-rays:

$$\lambda = 2 \cdot d \cdot (\sin \alpha_{i,n} - \sin \alpha_{i,m}). \quad (2.8)$$

Each incidence angle refers to a scattering vector \vec{q} which merely has a component perpendicular to the surface since the incidence angle α_i and the reflection angle α_r are equal. The magnitude of the scattering angle q ¹ can be calculated from the incidence angle α_i and the wave length λ of the x-rays:

$$q = \frac{4\pi}{\lambda} \sin(\alpha_i). \quad (2.9)$$

The difference $\Delta q = q_n - q_m$, which is the scattering vector belonging to the incidence angles $\alpha_{i,m}$ and $\alpha_{i,n}$, can be used to determine the film thickness d :

$$d = \frac{2\pi}{\Delta q}. \quad (2.10)$$

In case of one-layer systems the presentation of the intensity against the scattering vector q provides the film thickness d by analyzing the periodicity Δq of the oscillations (compare figure 2.6).

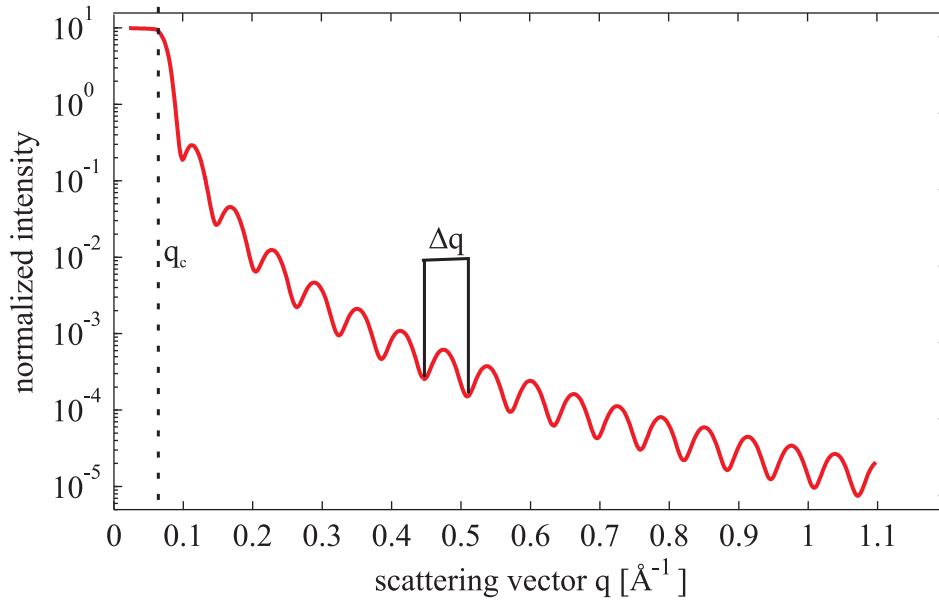


Figure 2.6.: Exemplary reflectivity for a one layer system. Total reflection exists up to a critical angle α_c and its belonging scattering vector q_c . For larger scattering vectors the intensity is reduced due to partly transmitted x-rays. The oscillations originate from the interference of the x-rays reflected at the interfaces vacuum/film and film/substrate. The film thickness d can be calculated from the distance Δq between two oscillations: $d = \frac{2\pi}{\Delta q}$.

In the case of multiple-layer systems, where several interfaces exist, equation (2.10) is not applicable to determine the film thickness. In this instance the path difference between several beams and multiple scattering must be taken into account. The software iXRR,

¹ In this thesis the magnitude of a vector \vec{z} is written as z .

developed in the working group of Prof. Wollschläger, allows the simulation of the reflectivity curve of arbitrary layer systems and the approximation of the measured data. The program determines recursively the reflectivity of the layer by using the Parratt algorithm [19]:

$$R_{j-1,j} = \frac{r_{j-1,j} + R_{j,j+1} \exp(id_j q_j)}{1 + r_{j-1,j} R_{j,j+1} \exp(id_j q_j)} \quad (2.11)$$

d_j is the thickness of the j -th film, q_j the belonging j -th scattering vector and $r_{j-1,j}$ the Fresnel reflection coefficient of the interface between the $(j-1)$ -th and j -th layer. A more detailed description of the program is illustrated in [20].

The basis of information for this chapter are references [21] and [22].

2.4. LEED - Low-energy electron diffraction

Low-energy electron diffraction (LEED) is useful to characterize the surface structure of crystalline materials. The depth, information can be gained from, is about 3-5 monolayers due to the small inelastic mean free path of electrons in solid materials. LEED is applied to prove the cleanness of surfaces and the arrangement of adsorbates. The method is based on the analysis of diffraction patterns which occur through interference of electron waves. The electron waves have the De-Broglie-wavelength

$$\lambda = \frac{h}{\sqrt{2mE}}. \quad (2.12)$$

In order to obtain diffraction patterns the wavelengths of the electrons and the atomic spacings have to be in the same range so the energy of the electrons is 50 - 300 eV ($\lambda \approx 1$ -2 Å).

The concept of the reciprocal space is utilized to describe the phenomenon of diffraction. The lattice points in the reciprocal two-dimensional space are given through the vectors

$$\vec{G}_{hk} = h\vec{a}^* + k\vec{b}^* \quad (2.13)$$

where $h, k \in (0, \pm 1, \pm 2, \dots)$ and \vec{a}^* and \vec{b}^* are direction vectors. The reciprocal direction vectors \vec{a}^* and \vec{b}^* can be calculated from the direction vectors \vec{a} and \vec{b} in real space through:

$$\vec{a}^* = 2\pi \cdot \frac{\vec{b} \times \vec{n}}{|\vec{a} \times \vec{b}|} \quad \vec{b}^* = 2\pi \cdot \frac{\vec{a} \times \vec{n}}{|\vec{b} \times \vec{a}|}. \quad (2.14)$$

Here \vec{n} is the surface normal.

In contrast to the diffraction in three dimensions, where lattice points exist in the reciprocal space, diffraction in two dimensions leads to diffraction rods perpendicular to the surface. A two-dimensional lattice can be interpreted as a three dimensional lattice with an infinite periodicity along the surface normal which means that the lattice points in the reciprocal space are infinitesimal close together.

For constructive interference of the electron waves equivalent to the occurrence of diffraction spots the Laue equations have to be complied:

$$\vec{q} \cdot \vec{a} = 2\pi h \tag{2.15}$$

$$\vec{q} \cdot \vec{b} = 2\pi k \tag{2.16}$$

$\vec{q} = \vec{k}_i - \vec{k}_f$ is the scattering vector, \vec{k}_i the wave vector of the incoming wave, \vec{k}_f the wave vector of the scattered wave and h and k the already in equation (2.13) mentioned Miller indices to label the crystal planes in the crystal lattice. The two-dimensional Ewald construction visualises the Laue equations (compare figure 2.7). Thereby, the surface of the Ewald sphere defines the set of all possible wave vectors of the scattered wave \vec{k}_f . The radius of this sphere is equivalent to the magnitude of the two wave vectors $k_i = k_f$, since the scattering takes place elastically. Diffraction spots exist where the shell of the Ewald sphere and the diffraction rods intersect because there the Laue equations are complied.

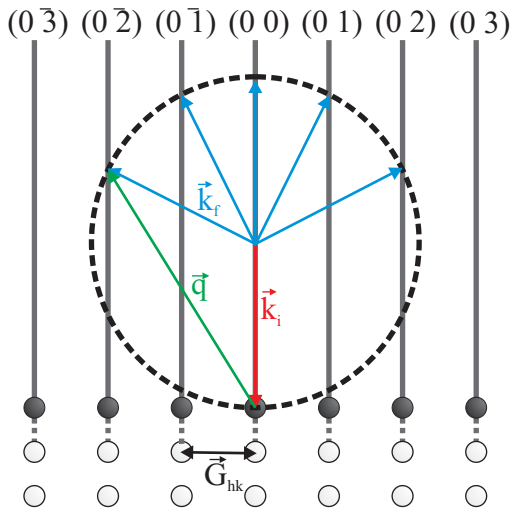


Figure 2.7.: Ewald construction in 2D. \vec{k}_i is the wave vector of the incoming and \vec{k}_f the wave vector of the scattered wave. \vec{G}_{hk} is the lattice vector in the reciprocal space. The shell of the Ewald sphere is defined by the set of all possible wave vectors \vec{k}_f of the scattered wave. The magnitude of the two wave vectors $k_i = k_f$ fix the radius of that sphere. Diffraction spots occur at the intersections between the Ewald sphere and the diffraction rods. Taken from [23].

With increasing electron energy the radius of the Ewald sphere scales up with the result that more diffraction spots emerge because more rods intersect with the shell of the Ewald sphere.

A more detailed description of LEED can be found in references [18] and [24].

2.5. XPS - X-ray photoelectron spectroscopy

2.5.1. Principle

X-ray photoelectron spectroscopy (XPS) is used to examine the electronic structure of occupied states in the surface near region in order to determine the stoichiometry of films and the oxidation states of the contained elements. The photoelectric effect, which was explained by Albert Einstein within his light quantum hypothesis in 1905, provides the basis for this method of measurement.

Core level electrons with the binding energy E_B absorb a (x-ray) photon with the energy

$$E_{Ph} = \hbar\omega \quad (2.17)$$

and leave the sample with the kinetic energy

$$E_{kin} = \hbar\omega - E_B - \phi_S \quad (2.18)$$

when the energy of the photon E_{Ph} is higher than the binding energy E_B of the electron and the work function ϕ_S of the sample. The binding energy E_B is the difference between the Fermi energy E_F and the energy of the orbital the electron had its origin in. The work function ϕ_S is the difference between the vacuum energy and the Fermi energy E_F . When measuring the kinetic energy of the outgoing photoelectrons their binding energy can be calculated. The binding energy is characteristic for the material and the orbital the electron arose from. The analyzer which is used to detect the photoelectrons has a workfunction ϕ_A as well, so the balance of energy changes to

$$E'_{kin} = \hbar\omega - E_B - \phi_A \quad (2.19)$$

according to figure 2.8

Here E'_{kin} is the kinetic energy which is corrected about the value $\phi_A - \phi_S$.

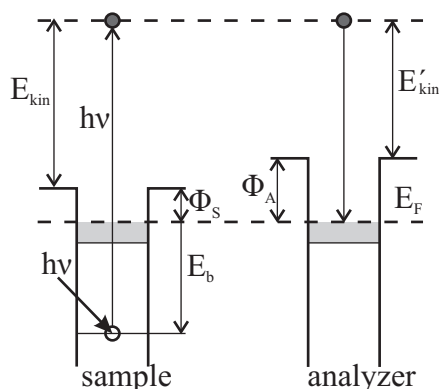


Figure 2.8.: Energy level diagram. An electron with the binding energy E_B absorbs an x-ray photon with the energy $E_{Ph} = \hbar\omega$. The energy of the absorbed photon has been higher than the binding energy E_B of the electron and the work function ϕ_S of the sample material with the result that the photoelectron leaves the sample with the kinetic energy E_{kin} . The electron is detected from the analyzer system with the corresponding work function ϕ_A with the kinetic energy E'_{kin} . Taken from [25].

2.5.2. Quantitative analysis

The penetration depth of x-rays in solids is 1- 10 μm but the mean free path of electrons in solids is about 10 \AA and limits the information depth of XPS to the same value. The reason for the smaller mean free path of electrons in solids compared to the one of x-rays in solids is that the interaction with the solid is higher in case of the electrons. Through the interaction, so the inelastic scattering, of the photoelectrons with cores and dislocations the photoelectrons loose parts or the whole kinetic energy and are shifted to higher binding energies. This effect is continuously and creates a so called inelastic background which has to be subtracted to analyze the stoichiometric composition of the sample. For the current analysis a Shirley background [26] has been subtracted from the primary spectra.

In order to obtain the peak intensities the measured data is approximated with several Gaussian-, Lorentzian- and Voight peaks and adjusted by element and orbital characteristic constants.

In a simplified form the intensity I_i of photoelectrons originating from orbital j from element i is given by

$$I_i = K(E)J\sigma_i^j(h\nu) \int_{z=0}^{\infty} \exp\left(\frac{-z}{\lambda(E) \cos(\theta)}\right) dz \quad (2.20)$$

where K is a term to cover all instrumental and geometric factors and depends on the kinetic energy of the photoelectrons, J the x-ray flux, σ the photoelectric cross-section which depends on the energy $h\nu$ of the incoming x-rays, $\lambda(E)$ the energy dependend inelastic mean free path (IMFP) of the photoelectrons, z the distance into the solid normal to its surface and θ the angle between the sample normal and the direction the photoelectron is emitted to.

In case of a relative comparison of peak intensities several terms cancel out. For a given material, containing element A and B, without a composition gradient in the depth the absolute and relative intensities of an element A are given by:

$$I_A = \frac{A_A^j}{\sigma_A^j(h\nu) \cdot \lambda(E) \cdot K(E) \cdot J} \quad (2.21)$$

$$\frac{I_A}{I_A + I_B} = \frac{A_A^j / (\sigma_A^j(h\nu) \cdot \lambda(E) \cdot K(E))}{A_A^j / (\sigma_A^j(h\nu) \cdot \lambda(E) \cdot K(E)) + A_B^j / (\sigma_B^j(h\nu) \cdot \lambda(E) \cdot K(E))} \quad (2.22)$$

Here A_A^j and A_B^j are the background corrected areas under the peaks belonging to the orbitals j of the elements A and B, $\sigma_A^j(h\nu)$ and $\sigma_B^j(h\nu)$ the belonging cross sections for the photon energy $h\nu$ and $\lambda(E)$ the respective material dependent IMFP of the photoelectrons with the kinetic Energy E .

The theoretical and experimental determinations of IMFP of electrons in solids display distinct variations [27]. The experimental quantification of the values depends on the deposition technique of the solid so a direct calibration for each experimental setup, which is as difficult as an IMFP measurement, is advisable [28]. Several predictive formulas to

calculate the IMFP based on experimental and theoretical data exist [29]. If the analyzed elements have orbitals at quite similar binding energies the uncertainties associated with the use of IMFPs can be avoided, because in that case the IMFPs and also the term K are nearly equal as well and cancel out. The equation 2.22 simplifies to

$$\frac{I_A}{I_A + I_B} = \frac{A_A^j / \sigma_A^j(h\nu)}{A_A^j / \sigma_A^j(h\nu) + A_B^j / \sigma_B^j(h\nu)}. \quad (2.23)$$

The determination of the stoichiometry requires merely the knowledge of the cross sections and the peak areas of the elements.

2.5.3. Spectral features

Several spectral features contain valuable information about the chemical surrounding of the chemical species and their oxidation state even though those features can complicate the quantitative analysis of the spectra.

First of all two types of peaks appear in the spectra: on the one hand core-level photoionization peaks and on the other hand x-ray induced Auger electron emission peaks. In figure 2.9 an example for a spectrum with Auger and photoionization peaks is illustrated.

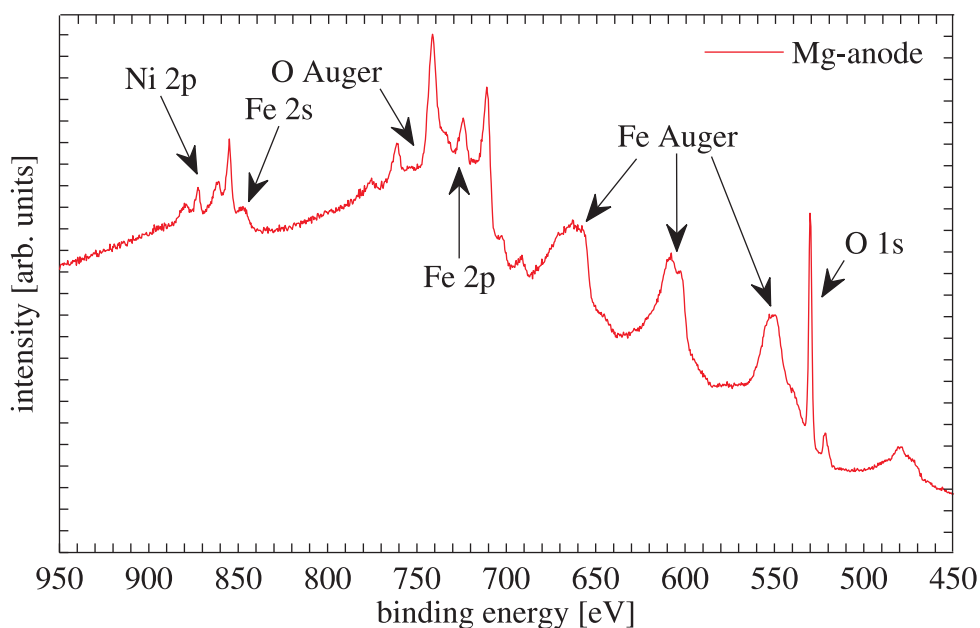


Figure 2.9.: XP-spectrum with Auger and photoionization peaks.

Auger peaks

While for the peaks based on the photoelectric effect there is a correlation between the energy of the x-ray quantum and the binding and kinetic energy of the photoelectron, there is no dependence between the energy of the x-ray quantum and the energy of the Auger electron for the Auger process. During the Auger process a core-level vacancy, in

this case arisen through photoionization, is filled by an electron from a higher level and the energy released because of the energy difference of the two levels is given to one other outer electron or a photon is emitted. In the case that an outer electron gets the released energy it leaves the atom with the same energy which the electron that transferred down lost minus the binding energy of the electron that is ejected from the atom.

So, the kinetic energy of the ejected electron is independent of the energy of the x-ray source and just depends on the energy levels of all involved electrons and is thereby characteristic for the chemical specie as well. When calculating the binding energy of the electrons from their measured kinetic energy with equation 2.19 the Auger peaks appear at different binding energies for different x-ray sources so equation 2.19 can't be used to calculate the binding energy of Auger peaks.

Both the peaks based on the Auger process and the photoelectric effect are tabulated for all chemical elements for the most common x-ray sources. In some cases Auger and photoelectric peaks superimpose and complicate the analysis of the spectra.

Peak width

The peak width is controlled by the lifetime of the core holes, the instrumental resolution and satellite features. The lifetime of core holes can be computed from the Heisenberg uncertainty relationship:

$$\Gamma = \frac{h}{\tau} \quad (2.24)$$

where Γ is the intrinsic peak width, h the Planck constant and τ the core hole lifetime. The intrinsic peak width is larger for inner shell orbitals compared to outer shell orbitals and increases with rising atomic number, since the electron density increases as well thereby increasing the probability of filling the core hole. The energy spread of the x-ray source and the resolution of the analyzer lead to an instrumental induced widening of the photoemission peaks. Satellite features like for example multiplet splitting or shake-up satellites have asymmetric lineshapes and are sometimes, depending on the resolution of the used spectrometer, not resolveable from the main photoemission peak so the peaks become wider.

Chemical shift

The photoemission peaks for the same element but with different oxidation states appear at slightly different binding energies. The explanation for this feature called chemical shift are chemical bondings which change the electrostatic shielding of the nucleus charge, since formal electrons have been added or removed and thereby influence the binding energy of the core-level electrons.

In some cases the shape of a photoemission peak indicates that the peak is composed of a number of subpeaks because one chemical specie is present in different oxidation states which have different chemical shifts. In figure 2.10 the Fe3p peak for the iron oxide magnetite is illustrated which consists of one peak for the Fe²⁺- and one for the Fe³⁺-ions [30].

Apart from the two subpeaks around 55 eV there are two further peaks at the high binding energy side whose origin is explained in chapter 2.5.2.

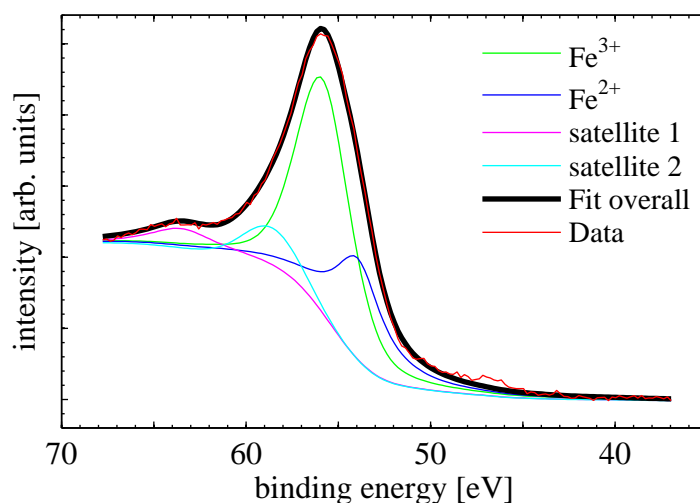


Figure 2.10.: Magnetite Fe3p peak consisting of two subpeaks for Fe^{3+} - (green) and Fe^{2+} - ions (blue). Furthermore, two additional peaks are necessary on the high binding energy side of the Fe3p peak to obtain the correct shape (compare chapter refsubsec:quantitative.)

Shake-up/Shake-off satellites

In figure 2.11 the phenomenon of shake-up/shake-off satellites is displayed in a spectrum of the Ni3p peak. The satellites occur when the photoelectrons loose energy through excitation of valence electrons from an occupied energy level to an unoccupied higher energy level. Most common are those shake-up satellites for aromatic structures or as in this case for transition metals. If the photoelectron transfers enough energy to the valence electron to ionize it into the continuum, the upcoming peak is called shake-off satellite.

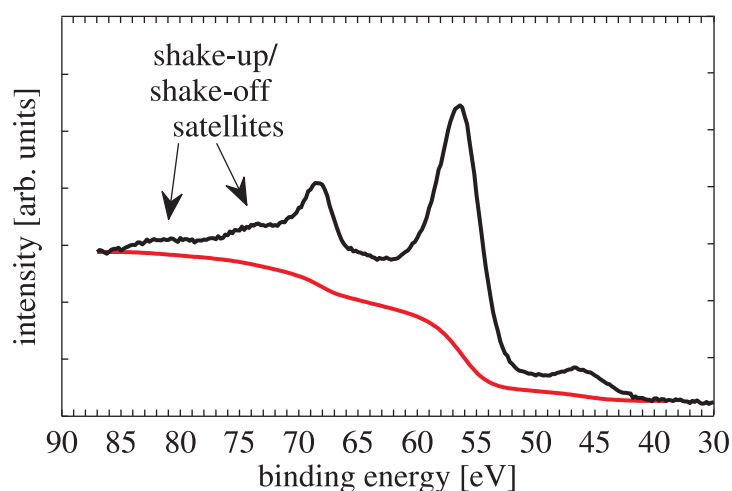


Figure 2.11.: Shake-up/shake-off satellites in the Ni 3p spectra.

Spin-orbit coupling and notation

If the angular momentum quantum number l of an orbital is higher than zero, so it's a p, d or f orbital, the photoemission peak is split in two peaks due to spin-orbit or j-j coupling.

As long as their spin quantum numbers s are different, 'spin up' and 'spin down', two electrons can be in the equivalent state. If a photoelectron leaves the atom the remaining electron can have a 'spin up' or 'spin down' orientation. There is a magnetic interaction between the spin of the electron and its orbital angular momentum which leads to an energy increase or decrease. This energy shift leads to the fact that the two electrons just different in their spin orientation appear at different binding energies in the spectra. The notation for those peaks uses the total angular momentum quantum number $j = l + s$. The notation is nl_j where n is the principal quantum number and for historical reasons the angular momentum quantum number $l = 0, 1, 2, 3$, etc. is replaced by the letters s, p, d, f , etc. For a $2p$ orbital there is a splitting in a $2p_{1/2}$ - and $2p_{3/2}$ -peak. The ratio of their respective degeneracies $2j + 1$ influences the intensities of the two peaks. Complex peak splittings can be found in spectra for transition metal ions and rare earth ions where multiplett splitting arises in p and d levels.

Exchange splitting

Theoretical calculations and experimental results show asymmetries in the XPS spectra of core lines for metals and their compounds [31]. The reason for the asymmetry is an adjustment of the Fermi level to the hole potential, abruptly created by the process of photoemission. Transition metals like iron and nickel reveal large asymmetries. One possible explanation is that the photohole pulls down an empty d state below the Fermi level, where it can be filled by an s electron. In case that the d state isn't filled by an s electron this results in a two-hole state and thereby to a satellite line with higher binding energy. The value of the exchange coupling ΔE_{ex} between a $3s$ hole and the $3d$ electrons for example can be calculated by:

$$\Delta E_{\text{ex}} = \frac{1}{2l + 1} (2S + 1) G^2(3s, 3d). \quad (2.25)$$

Here l is the orbital quantum number ($l=2$), S the total spin of the $3d$ electrons in the ground state and $G^2(3s, 3d)$ the Slater exchange integral [32]. The calculated values for $3d$ metal compounds are more than two times larger than the observed ones so the reason for the splitting can't solely be the spin exchange but also intrashell correlation effects between different electron configurations [33]. The value of the exchange splitting in the $3s$ spectra of metal compounds changes with the oxidation state of the metal. With increasing oxidation state the splitting increases [34]. For iron some experimental obtained splittings are as follows: Fe^{2+} about 5.4 eV , Fe^{3+} about 6.3 eV and about 7 eV for Fe^{4+} [34]. For nickel the splitting in the Ni^{2+} oxidation state is about 4.4 eV .

Charging effects

Isolating materials like MgO often exhibit charging during the XPS measurement, because the holes the liberated photoelectrons leave behind are not filled again. Consequently the binding energies of the orbitals change. With the assumption that the binding energy change has the same value for all orbitals the spectra can be calibrated with the help of the literature value of a peak not showing a chemical shift. For the characterization of iron oxides mostly the $\text{O}1s$ peak is used, because its position hardly changes for the different oxides. The NFO likely iron oxide magnetite and NFO show an $\text{O}1s$ position at $530.0 \pm 0.1 \text{ eV}$ so all spectra in this work are shifted in a way that the $\text{O}1s$ peak lies at

530.0 eV [35], [30]. The charging of the samples on MgO is about 10 eV but there is a small contribution in all spectra at the correct binding energy which probably originates from the also vaporized sample holder. This uncharged contribution on the sample holder which has a percentage between 0 and 25% with regard to the charged content is shifted within the calibration to lower binding energies as well, leading to spectra with the main peak at the correct position and a small peak, probably representing the vaporized sample holder, at a too low binding energy. For quantitative analysis as accurately as possible this uncharged peak has to be considered in addition to the larger charged peak.

The information of this chapter is based on references [18] and [36] where you can find further information.

2.6. XRD - X-ray diffraction

2.6.1. Principle

X-ray diffraction is a method of investigation which can be used to determine the structure of solid crystalline materials. X-rays interact with the electrons bound to the atoms in a sample. In case of crystals the atoms are arranged periodically so that incoming x-rays are diffracted at the electrons in the crystal planes since the atomic spacings and the wavelength of the x-rays are in the same order of magnitude. If the path difference of the diffracted rays is equal to an integer of the wavelength of the x-rays, diffraction maxima occur which are also called Bragg reflexes. The condition for the occurrence of Bragg reflexes is given by Bragg's law

$$2d_{hkl} \sin(\theta) = n\lambda, \quad n \in \mathbb{Z} \quad (2.26)$$

where d_{hkl} is the distance between successive crystal planes, θ the angle between the lattice planes and the incoming or reflected beam, λ the wavelength of the used x-rays and $n = 1, 2, 3, \dots$ the order of diffraction. Bragg's law is illustrated in figure 2.12.

Equivalent to Bragg's law are the Laue equations:

$$\vec{q} \cdot \vec{a} = 2\pi h \quad (2.27)$$

$$\vec{q} \cdot \vec{b} = 2\pi k \quad (2.28)$$

$$\vec{q} \cdot \vec{c} = 2\pi l. \quad (2.29)$$

Here \vec{k}_i and \vec{k}_f are the wavevectors of the incoming and diffracted wave. The difference $\vec{q} = \vec{k}_f - \vec{k}_i$ is the scattering vector. \vec{a} , \vec{b} and \vec{c} are the primitive translation vectors and h , k and l the Miller indices, both introduced in chapter 2.2. The Laue equations are just fulfilled for some special orientated scattering vectors, all other orientations of the scattering vector \vec{q} don't satisfy the Laue equations leading to the absence of Bragg reflexes. The phenomena of diffraction is usually described in the reciprocal space (compare chapter 2.4 for electron diffraction). The reciprocal space is spanned by the three basis vectors

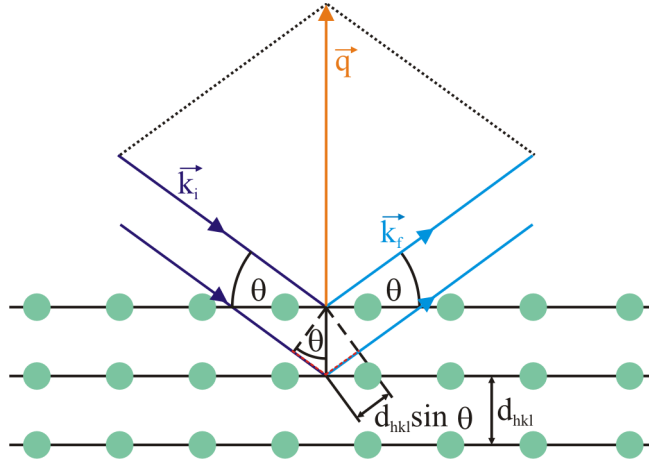


Figure 2.12.: Schematic diagram of x-ray diffraction at an incidence angle θ . The incoming x-rays are partly reflected and transmitted at the lattice planes having a distance d_{hkl} to the neighboring planes. If the path difference, $2 d_{hkl} \sin(\theta)$, between the reflected beams (indicated with the dashed red line) is an integer of the wavelength of the x-rays, the beams interfere constructively and a Bragg reflex occurs. The orientation of the scattering vector $\vec{q} = \vec{k}_f - \vec{k}_i$ is perpendicular to the lattice planes.

\vec{a}^* , \vec{b}^* and \vec{c}^* which can be calculated from the three unit vectors \vec{a} , \vec{b} and \vec{c} in real space and the volume of the unit cell $V_E = \vec{a} \cdot (\vec{b} \times \vec{c})$:

$$\vec{a}^* = 2\pi \frac{\vec{b} \times \vec{c}}{V_E} \quad (2.30)$$

$$\vec{b}^* = 2\pi \frac{\vec{c} \times \vec{a}}{V_E} \quad (2.31)$$

$$\vec{c}^* = 2\pi \frac{\vec{a} \times \vec{b}}{V_E}. \quad (2.32)$$

The scattering vector \vec{q} can be determined by the linear combination of the reciprocal lattice vectors:

$$\vec{q} = H\vec{a}^* + K\vec{b}^* + L\vec{c}^*. \quad (2.33)$$

The Laue equations are satisfied if the values of H, K and L coincide with the Miller indices h, k and l resulting in constructive interference for the according scattering vector. So the periodicity of the crystal lattice in real space is described by the lattice vectors while the periodicity of the diffraction reflexes is indicated by the reciprocal lattice vectors.

2.6.2. Bragg peaks

The Bragg equation and Laue equations just contain the directional description of the constructive interference at a periodical lattice but reveal no information about relative intensities of the reflexes. The relative intensities of the reflexes is influenced by the structure of the unit cell, the scattering ability of the involved atoms and the temperature of the crystal.

For the following, the kinematic approximation is applied meaning that multiple scattering is neglected due to the small interaction between x-rays and solids and that a fixed phase relation exists between the incoming and the scattered wave. Furthermore, the intensity of the x-rays scattered from the atomic nuclei is not considered since their cross section with x-rays is small compared with the one of electrons, causing that the diffracted intensity is dominated by the electron density distribution. For the intensity I of the diffracted x-rays the proportionality 2.34 is valid:

$$I \propto I_0 |G(\vec{q})|^2 |F(\vec{q})|^2. \quad (2.34)$$

Here I_0 is the intensity of the incoming x-rays, $G(\vec{q})$ the lattice factor and $F(\vec{q})$ the structure factor.

The structure factor

$$F(\vec{q}) = \sum_{j=1}^N f_j(\vec{q}) \cdot e^{i\vec{q}\vec{r}_j} \quad (2.35)$$

considers the structure of the unit cell. Here N is the number of atoms in the unit cell, \vec{r}_j the position of the atoms in the unit cell and $f_j(\vec{q})$ the atomar scattering factor of the atom at the position j . The atomar scattering factor $f(\vec{q})$ of an atom is the Fourier transform of the electron density distribution $\rho(\vec{r})$ of the atom:

$$f(\vec{q}) = \int d^3r \rho(\vec{r}) \cdot e^{i\vec{q}\vec{r}}. \quad (2.36)$$

The lattice factor $G(\vec{q})$ takes the symmetry of the crystal into account meaning the summation of the intensity contributions of the unit cells in all three spatial directions. So N_a , N_b and N_c are the numbers of the unit cells in the spatial directions given by the real space unit vectors \vec{a} , \vec{b} and \vec{c} . $G(\vec{q})$ is then given by:

$$G(\vec{q}) = \sum_{n_a=0}^{N_a-1} e^{i n_a \vec{q}\vec{a}} \cdot \sum_{n_b=0}^{N_b-1} e^{i n_b \vec{q}\vec{b}} \cdot \sum_{n_c=0}^{N_c-1} e^{i n_c \vec{q}\vec{c}}. \quad (2.37)$$

The summation of the intensity contributions in one spatial direction (for example in direction \vec{a}) can be described by the geometric series

$$|S_N(\vec{q})|^2 = \left| \sum_{n=0}^{N-1} e^{i n \vec{q}\vec{a}} \right|^2 = \left| \frac{1 - e^{i N \vec{q}\vec{a}}}{e^{i \vec{q}\vec{a}}} \right|^2. \quad (2.38)$$

With the substitution $Z = \vec{q}\vec{a}$ the N-slit function

$$|S_N(\vec{q})|^2 = \frac{\sin^2(N \cdot Z/2)}{\sin^2(Z/2)} \quad (2.39)$$

is obtained which is illustrated in figure 2.13. The n-slit function, also used to describe diffraction at a one dimensional lattice, has N main maxima which distance to each other is a multiple of 2π . The distance of the main maxima reveals information about the

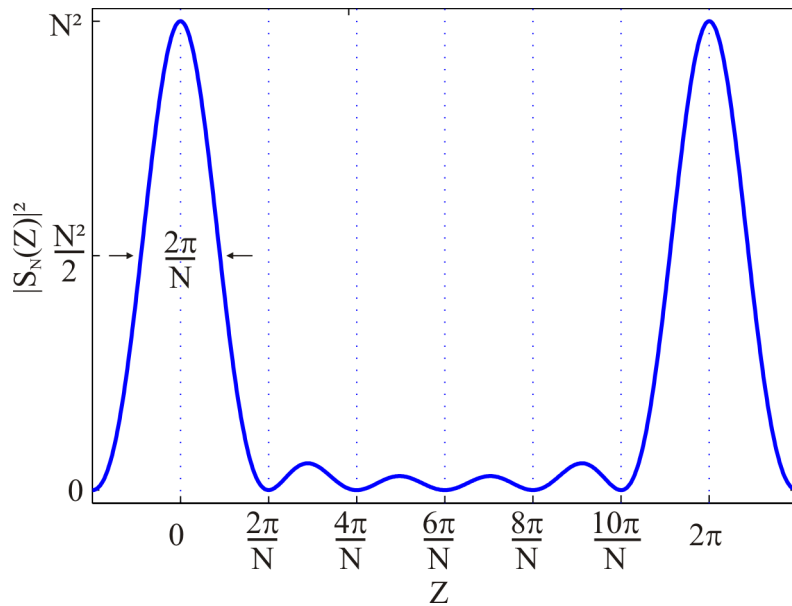


Figure 2.13.: N-slit function for $N = 6$. The main maxima are separated from each other by a multiple of 2π and between them $N - 2$ secondary maxima are present. The full width half maximum (FWHM) contains information about the number of slits and the distance between the main maxima about the distance of the slits. Taken from [37].

distance of the slits in the lattice and the full width half maximum (FWHM) about the number of slits. Between two main maxima $N - 2$ secondary maxima are present (so called fringes or Laue oscillations) which periodicity can be used to determine the number of slits and which manifestation decreases with increasing disorder of the crystal lattice.

Crystals infinitely extended in all three spatial directions reveal sharp diffraction reflexes (compare figure 2.14 a) since the limiting case of $N_1, N_2, N_3 \rightarrow \infty$ leads to δ -distributions for the main maxima.

The diffraction at a two-dimensional monolayer leads to diffraction rods (compare chapter 2.4) because in real space the periodicity along the surface normal is infinite meaning that the diffraction reflexes are infinitesimal close together in the reciprocal space (compare figure 2.14 b). For substrates the translation symmetry can't be assumed as infinite in all three spatial directions but is rather limited in vertical direction leading to a semi-infinite crystal with a more or less rough surface. Furthermore, the adsorption of a material limits the penetration depth of x-rays resulting in the fact that deeper layer contribute less to the diffracted intensity than layers close to the surface. These two effects broaden the reflexes in vertical direction implying that so called crystal truncation rods occur (compare figure 2.14 c). The intensity progression between two Bragg reflexes hence contains information about surface properties. For the diffraction of x-rays at a film deposited on a substrate the roughness at the surface and at the interface film/substrate influences the intensity progression (occurrence of fringes). But in contrast to the case of the infinitely extended and the semi-infinitely extended crystal the finite penetration depths and the according absorption of x-rays don't have to be considered for thin films leading to the diffraction reflexes shown in figure 2.14 d.

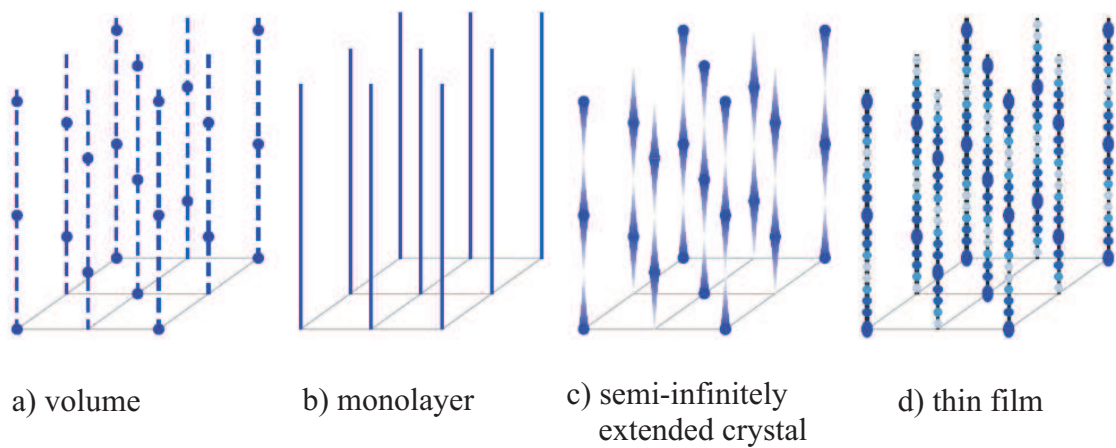


Figure 2.14.: Illustration of the reciprocal space for the diffraction at a) an infinitely extended crystal (volume), b) a two-dimensional monolayer, c) a semi-infinitely extended crystal and d) a thin film. The dashed lines in the depiction for the infinite crystal just indicate the vertical direction for the sharp reflexes. For the monolayer diffraction rods occur because of the reduced translation symmetry. The semi-infinite crystal shows crystal truncation rods in the reciprocal space and the diffraction at thin films leads to oscillations (fringes) between the Bragg reflexes. From the fringes, information about the film quality can be gained. Taken from [38].

The information provided in this chapter is based on references [36] and [39].

3. Investigated materials

This chapter has the function to introduce the investigated materials. The crystalline properties of magnesium oxide (MgO) are described in chapter 3.1 while the equivalent is illustrated for strontium titanate (SrTiO₃, STO) in chapter 3.2 and for nickel ferrite (NiFe₂O₄, NFO) in chapter 3.3.

3.1. Magnesium oxide - MgO

The inorganic salt magnesium oxide consists of magnesium ions Mg²⁺ and oxygen ions O²⁻ with the ratio 1:1. It crystallizes in the sodium chloride structure with the lattice constant $a_{\text{MgO}} = 4.2117 \text{ \AA}$, meaning a out-of-plane layer distance of $c_{\text{MgO}} = a_{\text{MgO}}/2 = 2.10585 \text{ \AA}$. Both kinds of ions build a face-centered cubic crystal lattice which are shifted against each other about half the length of the unit cell. Each oxygen ion is surrounded by six magnesium ions and reversed. The surface unit cell of MgO is a squarish unit cell with the lattice constant $a_s = a_{\text{MgO}}/\sqrt{2}$. In relation to the volume unit cell the surface unit cell is rotated about 45° (compare figure 3.1).

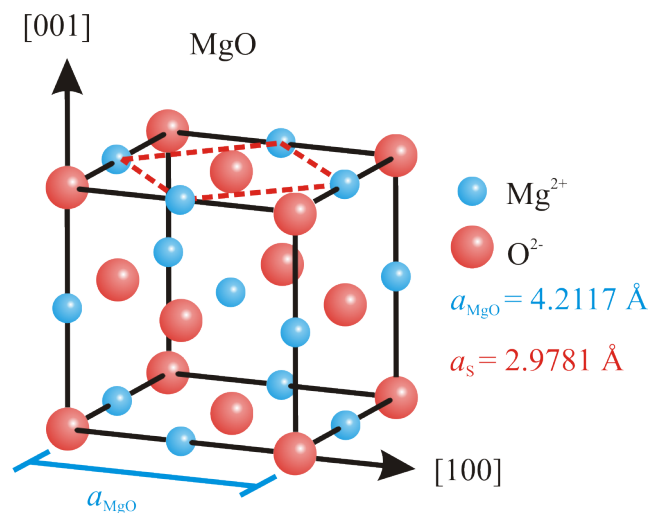


Figure 3.1.: Illustration of the magnesium oxide volume and surface(001) unit cell. Taken from [14].

Magnesium oxide has a band gap of 7.8 eV [40] and is thereby an insulator and transparent for visible light.

3.2. Strontium titanate - SrTiO₃

Strontium titanate (SrTiO₃, STO) crystallizes in the perovskite structure ($A^{2+}B^{4+}O_3^{2-}$) with an cubic unit cell with the lattice constant $a_{\text{STO}} = 3.901 \text{ \AA}$, so a out-of-plane layer distance of $c_{\text{STO}} = a_{\text{STO}}/2 = 1.9505 \text{ \AA}$. [41]. The Ti⁴⁺ cations are located at the body center position and are surrounded by an octahedron of O²⁻ anions which thereby occupy the face center positions of the "cube". The Sr²⁺ cations are in a 12-fold coordination and are located on the corners of the "cube". The unit cell of STO is illustrated in figure 3.2.

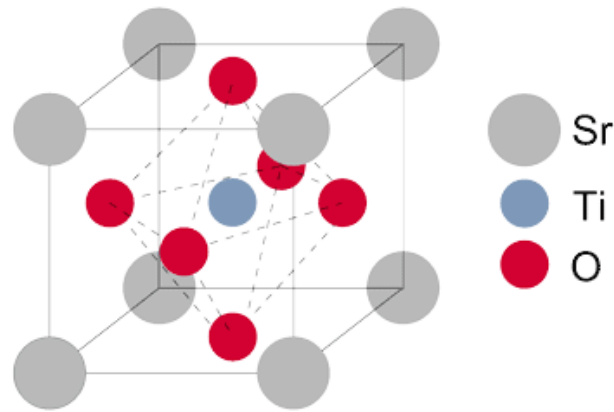


Figure 3.2.: Illustration of the strontium titanate unit cell. Taken from [42].

Strontium titanate has an indirect band gap of 3.25 eV [43] so it's an insulator. To avoid undesirable charging effects during the LEED and XPS measurements the STO substrates are doped with 0.05 wt% Nb making them electrically conducting.

3.3. Nickel ferrite - NiFe₂O₄

Nickel ferrite (NFO) has the same crystal structure like the iron oxide magnetite (Fe₃O₄) where the Fe²⁺ ions are replaced by Ni²⁺ ions. It crystallizes in the inverse spinel structure $A^{3+}[B^{2+}B^{3+}]O_4^{2-}$ with the lattice constant $a_{\text{NFO}} = 8.34 \text{ \AA}$, so a out-of-plane layer distance of $c_{\text{NFO}} = a_{\text{NFO}}/4 = 2.085 \text{ \AA}$ [1]. The unit cell contains 32 oxygen ions in a face-centered cubic arrangement. Out of the 64 tetrahedral sites (A sites) 8 are occupied by Fe³⁺ ions. From the existing 32 octahedral sites (B sites) 8 are occupied by Fe³⁺ ions and 8 by Ni²⁺ ions. The net magnetization is caused by the Ni²⁺ ions due to an antiferromagnetic coupling existing between the Fe³⁺ ions on the octahedral and tetrahedral sites. The lattice constant $a_{\text{NFO}} = 8.34 \text{ \AA}$ of NFO is nearly twice as large as the one from MgO so that the lattice mismatch is 1%. On the assumption of pseudomorphic growth of NFO on MgO the film is under tensile strain in in-plane direction. The lattice mismatch between STO and NFO is about -7%, meaning compressive strain of the NFO in in-plane direction in the case of pseudomorphic growth. In figure 3.3 the NFO unit cell is illustrated.

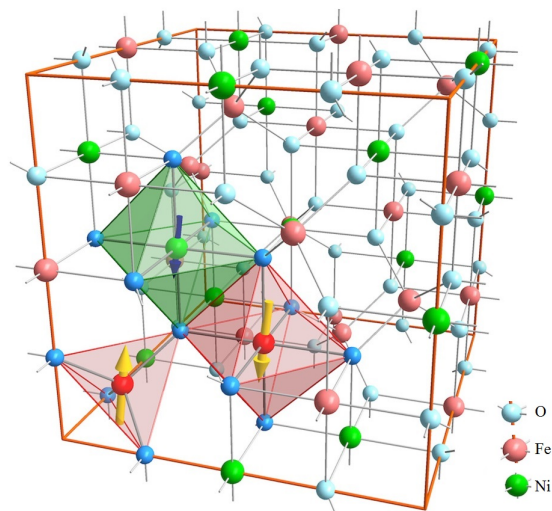


Figure 3.3.: Illustration of the nickel ferrite unit cell. The oxygen ions (blue) build a face-centered cubic crystal lattice. An eighth of the tetrahedral sites are occupied by Fe^{3+} ions (red) and respectively one quarter of the octahedral sites are occupied by Fe^{3+} (red) and Ni^{2+} ions (green). Taken from [15].

4. Experimental setup and sample preparation

The experimental setup up of the ultra high vacuum chamber used to prepare the films and to in-situ measure LEED and XPS is exposed in chapter 4.1 and the setup of the two methods are presented in chapter 4.1.1 and 4.1.2. The setup of the diffractometer used to perform the XRR and XRD measurements is depicted in chapter 4.2. Afterwards in chapter 4.3 the pretreatments of the substrates and the conditions for the film deposition are presented.

4.1. Experimental setup of the ultrahigh vacuum system

The preparation and in-situ characterization of thin films require an ultra high vacuum to avoid impurities inside the films and to ensure the detection of photoelectrons and diffracted electrons since their inelastic mean free path in air is too small to reach the detector or fluorescence screen. The used ultra high vacuum chamber is constituted of four chambers (compare figure 4.1) separated from each other by valves. A shared rotary vane pump pumps all chambers from atmospheric pressure down to about 10^{-3} mbar and serves as backing pump for the turbomolecular pumps which every chamber has on its own. The turbomolecular pumps generate a pressure of down to 10^{-9} mbar which is sufficient for the load lock and the preparation chamber I. The analysis chamber and preparation chamber II have a ion-getter pump and a titanium sublimator in addition which facilitate pressures down to 10^{-10} mbar. More detailed information concerning the pump system are stated in [18].

A transfer system, based on wobble sticks, enables the transportation of the samples between the chambers. Both preparation chambers contain a manipulator the sample is fixed on. It is adjustable in all three spatial directions, can be rotated about 360° and is equipped with a sample heating which is based on a current-carrying filament and a high voltage behind the backside of the sample. Moreover the manipulator has a thermal element to determine the temperature of the sample. Precision valves in both preparation chambers allow the inlet of oxygen in the chambers to provide the oxygen atmosphere for RMBE. Each preparation chamber is equipped with a nickel and iron effusion cell. In case of the preparation chamber I the two effusion cells are perpendicular to each other so the co-deposition has to happen with an incidence angle of 45° to the surface normal. Preparation chamber II has been provided with the two effusion cells belatedly, because the samples prepared in chamber I revealed a film thickness gradient and in chamber II a larger distance between the cells and the sample exist. So, a more homogenous distribution of the nickel and iron atoms on the sample is expected. The analysis chamber includes measuring instruments for XPS and LEED, performed in-situ.

All chambers are equipped with a vacuum gauge to control the present pressure and to adjust the suitable oxygen atmosphere.

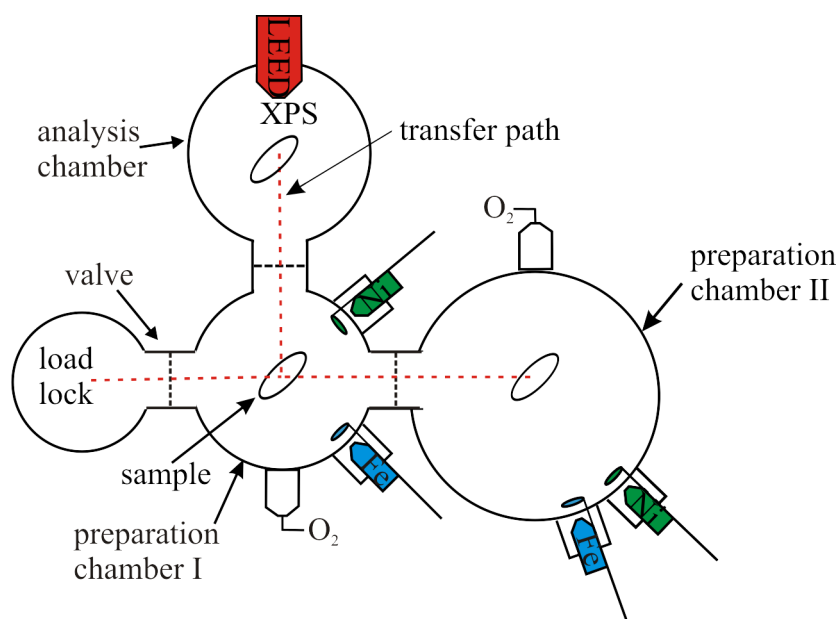


Figure 4.1.: Setup of the ultra high vacuum system. The system consists of four chambers separated by valves including analysis and preparation chambers. With the help of a transfer system the samples can be transported between the preparation chambers and the analysis chamber.

4.1.1. Low-energy electron diffraction

The LEED measurements require an experimental setup inside an ultrahigh vacuum with a pressure less than 10^{-9} mbar. It includes an electron gun with a filament and a Wehnelt cylinder, a lens system, a fluorescence screen, three grids and a sample and is visualized in figure 4.2.

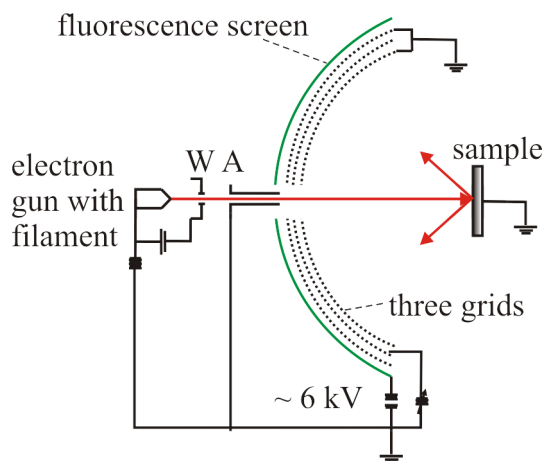


Figure 4.2.: Experimental setup for LEED. A collimated electron beam is generated in the electron gun by emitting electrons from a filament which are accelerated and collimated using an anode and a Wehnelt cylinder W. The lens system A focusses the beam that reaches the sample. The electrons are scattered at the sample, pass through a grid system and the diffraction pattern is displayed at the fluorescence screen and can be recorded with a camera behind the electron gun. Adapted from [23].

Inside the electron gun electrons are emitted from a filament and accelerated and collimated with an anode and a Wehnelt cylinder. Out of them a collimated electron beam with an energy of 0-1000 eV is created and focussed on the sample by using a lens system. Before the scattered electrons reach the fluorescence screen they pass through three grids. The first grid is at earth potential to provide a field-free space after the electron scattering. The second grid has a potential slightly smaller compared to the one of the filament and is meant to reject the inelastically scattered electrons in order to obtain a high spot-to-background contrast. The third grid is at earth potential as well in order to screen the other grids from the high voltage of about 6 kV of the fluorescence screen. The high voltage is necessary to reaccelerate the electrons to a high energy to cause fluorescence of the screen after they have been retarded through the second grid. The diffraction pattern for different electron energies, visible on the screen, is recorded with a camera behind the electron gun.

4.1.2. X-ray photoelectron spectroscope

The experimental setup for x-ray photoelectron spectroscopy is contained in an ultrahigh vacuum with a pressure less than 10^{-9} mbar. It is illustrated in figure 4.3 and includes a non-monochromatic x-ray source, an energy discriminative electron analyzer, an electron detection system and a sample.

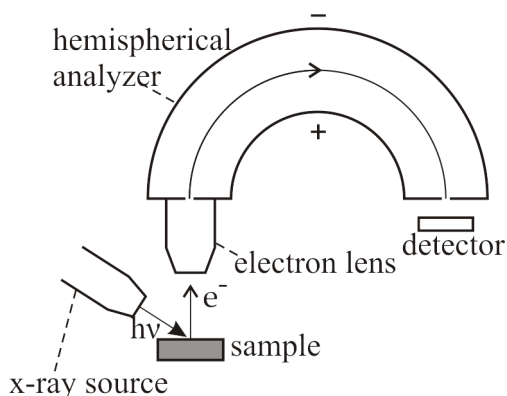


Figure 4.3.: Experimental setup. X-ray photons are emitted on the sample from the x-ray source. Based on the photoelectric effect photoelectrons leave the sample, pass through an electron lens system and an energy discriminative electron analyzer and reach the detection system. Adapted from [25].

The main excitation line of the x-ray source is the $K_{\alpha 1/2}$ line with an energy of 1486.6 eV for the Al-anode and 1253.6 eV for the Mg-anode. The next intensive line is the $K_{\alpha 3}$ line, with an energy shift about 9.8 eV to higher photon energies and an intensity of 6.4% relative to the $K_{\alpha 1/2}$ line. Further less intensive lines are the $K_{\alpha 4}$, $K_{\alpha 5}$, $K_{\alpha 6}$ and K_{β} line which are not considered in this thesis.

A potential difference within the energy discriminative electron analyzer leads the electrons on a circular path which radius depends on the kinetic energy of the photoelectrons and the value of the potential difference. In the used setup an electron lens system accelerates or decelerates the photoelectrons on a fixed kinetic energy instead of changing the difference of potential. The advantage of that mentioned fixed analyzer transmission-mode (FAT-mode) is a constant energy resolution for the whole kinetic energy range.

At the end of the analyzer the detection system, so the channeltrons, are positioned. The channeltrons count the incoming electrons and provide together with the information

In order to perform the XRD measurements at DESY the described setup is used and the angle of incidence and reflection are controlled by OM and TT. In both cases the (00L)-direction is scanned so the angle of incidence and reflection are kept equal by keeping the angle TT twice as big as the angle OM.

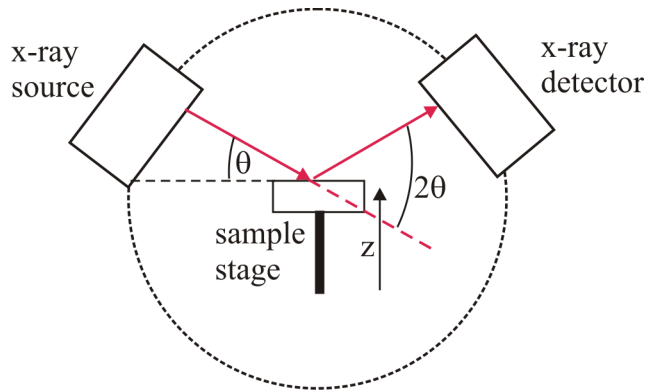


Figure 4.5.: Setup of a 2θ -geometry diffractometer. The x-rays reach the sample with the incidence angle θ and the diffracted intensity is measured with a point detector under the angle 2θ . The alignment of the sample laying on the sample stage is limited to the change of the height z . If the sample surface and the stage are not parallel the misfit has to be corrected by the incidence angle.

The XRR measurements of all samples and the XRD measurements of the samples grown on STO have been done with an x-ray diffractometer at the Universität Bielefeld, where the setup is illustrated in figure 4.5. The incidence angle θ is combined with the detector angle 2θ so whenever the incidence angle is changed about a value the detector moves about the doubled value. In contrast to the setup at DESY the detector is a point detector just movable around the one angle so just the measurement of the (00)-rod is possible with this 2θ -geometry. The sample is placed on the sample stage and is just movable in the center of the beam by changing the height z . If the surface of the sample isn't plane to the sample stage, the misfit can be removed by changing the incidence angle of the x-rays. Further alignment is not possible. The x-rays used in Bielefeld originate from a Cu-anode and the energy of the $K_{\alpha 1}$ line is 8.054 keV resulting in a wavelength of 1.540598 Å.

4.3. Sample preparation

Fifteen samples on MgO with varying Ni/(Fe+Ni) ratios, meaning the preparation of a series of $\text{Ni}_x\text{Fe}_{3-x}\text{O}_4$ ($0 < x < 1$) samples, and nearly constant deposition times, in order to obtain similar film thicknesses, have been prepared by RMBE. Afterwards five samples on STO with varying film thickness have been deposited using the optimized Ni/(Fe+Ni) ratio from the MgO samples, resulting in stoichiometric NiFe_2O_4 on STO.

The monocrystalline MgO substrates have been supplied by CrysTec, have a (001) orientation and a polished surface and are $10 \times 10 \times 0.5 \text{ mm}^3$ in size. The Surface Net GmbH produced the monocrystalline STO substrates which are doped with 0.05 wt% Nb. The size and orientation of the STO substrates are the same as for MgO and the surface is polished as well. Both kinds of substrates are annealed at a temperature of 400°C for one hour in an oxygen atmosphere of $1 \times 10^{-4} \text{ mbar}$ to remove undesirable adsorbates like carbon and oxygen dislocations within the crystal lattice. The accuracy of the crystal

surface structure and its composition are checked by LEED and XPS measurements before the films are deposited on them.

The starting point for the preparation of $\text{Ni}_x\text{Fe}_{3-x}\text{O}_4$ ($0 < x < 1$) has been the iron oxide magnetite (Fe_3O_4) which has the same crystal structure if the Ni^{2+} ions are replaced by Fe^{2+} ions and which growth was examined intensively during the last years [45], [37] in order to find the most suitable growth conditions for both substrates. The growth conditions to deposit $\text{Ni}_x\text{Fe}_{3-x}\text{O}_4$ ($0 < x < 1$) within the work for this thesis are those optimized parameters since the only difference is the replacement of Fe^{2+} ions through Ni^{2+} ions. For the deposition an oxygen pressure of 5×10^{-6} mbar and a substrate temperature of 250°C have been used. The high voltage inside both effusion cells is 1250 V. For the nickel effusion cell the emission currents have reached from 18 to 27 mA, the electric power accordingly from 22.5 to 33.75 W. The iron effusion cell has been used with emission currents between 24 and 31 mA and according electric powers from 30 to 38.75 W. The first five samples (A-E) on MgO have been prepared in the preparation chamber I, but due to the reasons mentioned in chapter 4.1 the next samples have been prepared in preparation chamber II. The crystal oscillators in the effusion cells in chamber I have been calibrated by preparing NiO and Fe_3O_4 films on MgO and measuring the thickness with XRR afterwards. So, the Ni/(Fe + Ni) ratio has been varied by adjusting both electrical powers in a way that the film thickness stayed constant. In table 4.1 an overview about the samples A-E prepared on MgO in chamber I with their varied growth parameters and their Ni/(Fe+Ni) ratio, based on the analysis of the Fe3p and Ni3p peak, is given. The analysis of the respective 3p peaks and the occurrence of the relatively large uncertainty is explained in chapter 2.5.2.

sample	Δf_{Ni} [Hz]	Δf_{Fe}	P_{Ni} [W]	P_{Fe} [W]	d [nm]	t [min]	Ni/(Fe+Ni) [%]
A	12451	11256	28.75	30	39 ± 3	32	62 ± 8
B	10069	12300	31.25	32.5	36 ± 3	17	60 ± 8
C	10736	10400	33.75	30	31 ± 3	17	57 ± 8
D	6590	11649	31.25	36.25	28 ± 3	10.5	53 ± 8
E	6353	13245	30	38.75	34 ± 3	8.3	39 ± 8

Table 4.1.: Growth parameters and Ni/(Fe+Ni) ratios of the samples A-E on MgO prepared in chamber I. Δf_{Ni} and Δf_{Fe} are the frequency changes of the crystal oscillators in the Ni and Fe effusion cells, P_{Ni} and P_{Fe} the electric powers of the two cells, d the film thickness and t the deposition time.

For the crystal oscillators in the effusion cells in chamber II a calibration concerning the film thickness wasn't possible so it was assumed that a deposition at the same emission current yields into a similar film thickness. The growth parameters and Ni/(Fe+Ni) ratios of the samples F-P on MgO, deposited in chamber II, are listed in table 4.2. On the samples F, H and J the XRR measurements for the determination of the film thickness couldn't be done because XRF measurement had been tried before and left a disturbing foil at the surface.

During the preparation of the samples F-M in chamber II the Ni/(Fe+Ni) ratio has been varied by keeping the electric power of the iron effusion cell constant and changing the the power of the nickel cell. Just for sample N-P the electric power of the Ni effusion cell is

fixed and the power of the Fe effusion cell is changed with respect to the previous samples, since a fine adjustment for the Ni/(Fe+Ni) ratio had to be made and the Fe effusion cell is adjustable more precisely. During the deposition of sample O the crystal oscillator of the iron effusion cell stopped working so there is no value for the frequency change of the iron crystal oscillator for the samples O and P and the following samples on STO.

sample	Δf_{Ni} [Hz]	Δf_{Fe}	P_{Ni} [W]	P_{Fe} [W]	d [nm]	t [min]	Ni/(Fe+Ni) [%]
G	4527	4240	27.5	38.75	10±3	12	32±8
H	6815	4627	28.75	38.75	-	12	42±8
I	5045	2110	26.25	38.75	6±3	13	46±8
J	1109	4272	22.5	38.75	-	15	10±8
K	1948	6040	23.75	38.75	10±3	15	7±8
L	3966	7524	26.25	38.75	13±3	15	19±8
M	5661	8833	27.5	38.75	16±3	15	23±8
N	6255	8535	27.5	37.5	16±3	15	21±8
O	6146	-	27.5	36.25	14±3	15	27±8
P	5503	-	27.5	36.25	18±3	15	33±8

Table 4.2.: Growth parameters and Ni/(Fe+Ni) ratios of the samples F-P on MgO prepared in chamber II. Δf_{Ni} and Δf_{Fe} are the frequency changes of the crystal oscillators in the Ni and Fe effusion cells, P_{Ni} and P_{Fe} the electric powers of the two cells, d the film thickness, t the deposition time.

Due to a different analysis during the process of deposition the Ni/(Fe+Ni) ratios (also called Ni contents) were slightly higher compared to the presented analysis so that the deposition wasn't stopped after the preparation of sample G which seems to have the optimal Ni content. Apart from the fact that it wasn't realized that the content has already been optimized in G it is important for the further analysis to have samples with too little and too much iron.

The growth parameters and the Ni/(Fe+Ni) ratios of the samples Q-U on STO, which have been deposited in chamber II, are listed in table 4.3. For the five samples with different thickness grown on STO the electric powers P_{Ni} and P_{Fe} of the nickel and iron effusion cells are kept to 27.5 W and 36.25 W as optimized during the preparation of the samples on MgO.

sample	Δf_{Ni} [Hz]	d [nm]	t [min]	Ni/(Fe+Ni) [%]
Q	1184	4.7±0.5	2.5	27
R	2002	10±0.5	5	31
S	4420	13±1	10	33
T	8353	27±2	20	30
U	17227	60±2	40	28

Table 4.3.: Growth parameters and Ni/(Fe+Ni) ratios of the samples Q-U on STO prepared in chamber II. Δf_{Ni} is the frequency change of the crystal oscillator in the Ni effusion cell, d the film thickness and t the deposition time.

After the preparation of the samples LEED and XPS measurements have been performed

in-situ. For the samples B-D XRD measurements have been carried out at DESY while XRR measurements for all samples have been done in Bielefeld.

5. Results and discussion of $\text{Ni}_x\text{Fe}_{3-x}\text{O}_4$ ($0 < x < 1$) films grown on MgO

The results for the growth of nickel ferrite on MgO, gained through the various methods of measurements, are presented in this chapter. The main focus of the analysis is on the XPS measurements and their quantitative and qualitative interpretation illustrated in chapter 5.1. In chapter 5.2 the LEED images of the films are shown and interpreted. Afterwards the XRR results are summarized in chapter 5.3 and the XRD results in chapter 5.4. The last chapter 5.5 contains the discussion of all obtained results.

5.1. XPS results

This chapter is divided into three parts. The first part deals with the quantitative interpretation of the Fe3p and Ni3p peaks to determine the stoichiometry of the deposited films. Afterwards the Fe2p spectra are analyzed qualitatively since they contain valuable information concerning the oxidation state of the iron in the surface near region. In the last part the attention is given to the Fe3s peak of the films which reveal knowledge regarding exchange splitting and thereby the oxidation state as well.

5.1.1. Quantitative analysis of the Fe3p and Ni3p peaks

The analysis of the stoichiometry of all films is made on the basis of the Fe3p and Ni3p peak. The shown and analyzed 3p spectra in this chapter have been measured with the Al-anode. As mentioned in chapter 2.5.2 the information depths of XPS is limited to the surface near region. Since the growth parameter are constant during the deposition of the films it is assumed that the composition stays constant from the surface down to the bottom of the films. In order to obtain the peak areas for the determination described in chapter 2.5.2 the peaks are approximated with the freeware program XPSPEAK41. Apart from the main, most intensive excitation line ($K_{\alpha 1/2}$ line), less intensive lines contribute to the intensity as well. The approximations performed during the work for this thesis consider just the next intensive $K_{\alpha 3}$ line and only for the main peak. For the films prepared on the insulator MgO there is a further peak for each element due to charging effects (compare chapter 2.5.3). To define the value of charging and the content of the uncharged sample the O1s peak, existing at a binding energy of 530 eV, is approximated first for each film as explained in chapter 2.5.3. The obtained values of charging and the uncharged content on the sample holder are then conditions for the approximations of the further peaks. The value of charging reaches from 9 eV up to 15 eV and the uncharged content lies between 7 and 25 % compared to the main most intensive $K_{\alpha 1/2}$ peak. In figure 5.1 the approximation of the O1s peak is displayed exemplarily. The approximation includes

the main peak of the most intensive $K_{\alpha 1/2}$ line, the $K_{\alpha 3}$ line with an intensity of 6.4% with regard to the $K_{\alpha 1/2}$ line and the peak due to the uncharged content, here just the contribution of the most intensive line.

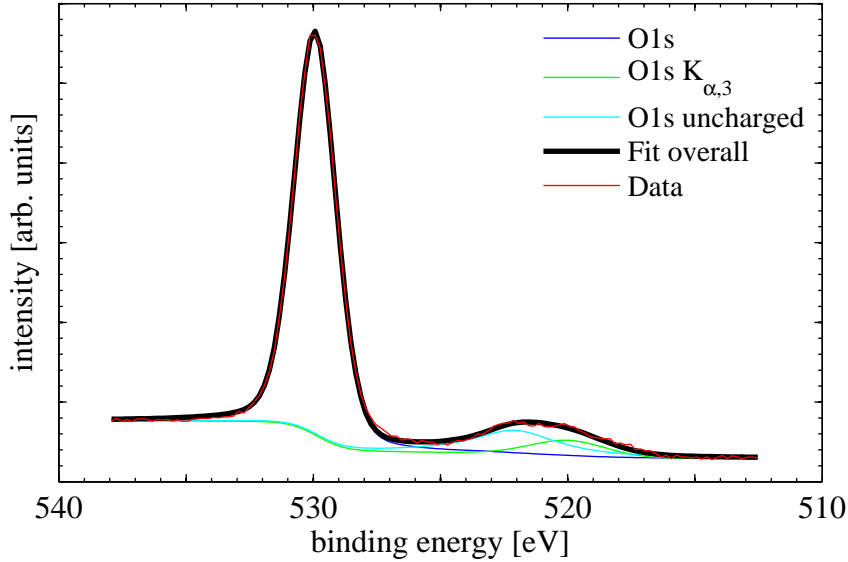


Figure 5.1.: Exemplary approximation of the O1s peak. The measured data (red) is reconstructed (black) by three peaks. Additionally to the main peak of the most intensive $K_{\alpha 1/2}$ line (blue) and the $K_{\alpha 3}$ line (green) the peak due to the uncharged content (cyan) contributes to the intensity.

The Fe3p and Ni3p peak lying at about 55.8 eV and 67.7 eV on MgO are approximated in the same way as described above but with fixed charging values, originating from the approximation of the O1s peak. But not just position and area are fixed with regard to the main peak also the FWHM is held at the same value as the main peak.

Even though the 3p peaks should consist of two peaks because of the spin-orbit coupling there is only one peak for each element. The explanation for the occurrence of just one peak is that the energy difference between the peaks originating from spin-orbit coupling is tiny and unresolvable with the used spectrometer.

In addition to the main peaks of iron and nickel there are two shake-up/shake-off satellites at a binding energy of about 72.5 eV and 81 eV for the Ni3p and one satellite for the Fe3p at about 63.5 eV. The positions of these satellites is fixed for all approximations. The remaining peak fixed at 58.6 eV is necessary to obtain the shape of the main line. Neither the satellite at about 63.5 eV (Fe3p satellite 1) nor the additional peak (satellite 2) to obtain the shape of the main line can be explained by multiplett splitting predicted for Fe 3+ and are attributed to electron correlation effects which are getting more influencing the higher the core lines [46].

As before, the uncharged content of the film on the sample holder is just considered for the most intensive $K_{\alpha 1/2}$ line and the $K_{\alpha 3}$ line just for the main peak. In total, ten peaks are used to approximate the Fe3p and Ni3p peaks which is exemplified in figure 5.2.

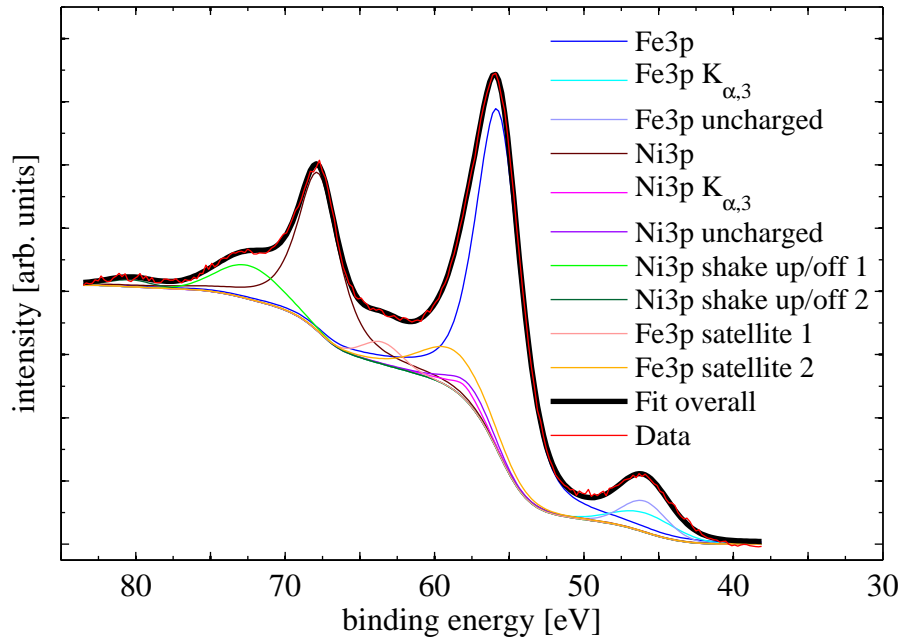


Figure 5.2.: Exemplary approximation of the Fe3p and Ni3p peak. The measured data (red) are reconstructed (black) by ten peaks: the main peaks of the most intensive $K_{\alpha 1/2}$ line (blue for Fe and brown for Ni) and the $K_{\alpha 3}$ line (cyan for Fe and magenta for Ni), the peaks due to the uncharged content (blue-gray for Fe and purple for Ni), the two shake-up/shake-off satellites for Ni (both green), the shake up/off for Fe (orange) and the Fe satellite necessary to shape the main line correctly (yellow).

To obtain the total intensity of each element and to calculate the composition of the films all contributions apart of the uncharged content and the $K_{\alpha 3}$ line for each element are summarized and corrected about the element and orbital specific photoelectric cross sections. The orbital specific cross sections of the involved elements at the photon energy of Al $K_{\alpha} = 1486.6$ eV are listed in table 5.1.

peak	peak position [eV]	cross section
Ni 3p	67.8	2.22
Fe 3p	55.8	1.67

Table 5.1.: Photoelectric cross sections at the photon energy of Al $K_{\alpha} = 1486.6$ eV for the Ni3p and Fe3p peak [47].

The approximation of both 3p peaks by using ten peaks leads to relatively large uncertainties, since even though there are the aforementioned specifications for the positions, the FWHMs and the relative areas, there are still many degrees of freedom.

Figure 5.3 outlines the Fe3p and Ni3p peaks for different Ni/(Fe+Ni) ratios starting with no nickel at the bottom (Fe_3O_4) and ending with 60% nickel at the top. In order to keep the spectra clear the reconstructions aren't included.

The shown spectra have been corrected about the peaks belonging to the uncharged content and the $K_{\alpha 3}$ line with the purpose to show the undisturbed shape of the peaks. As

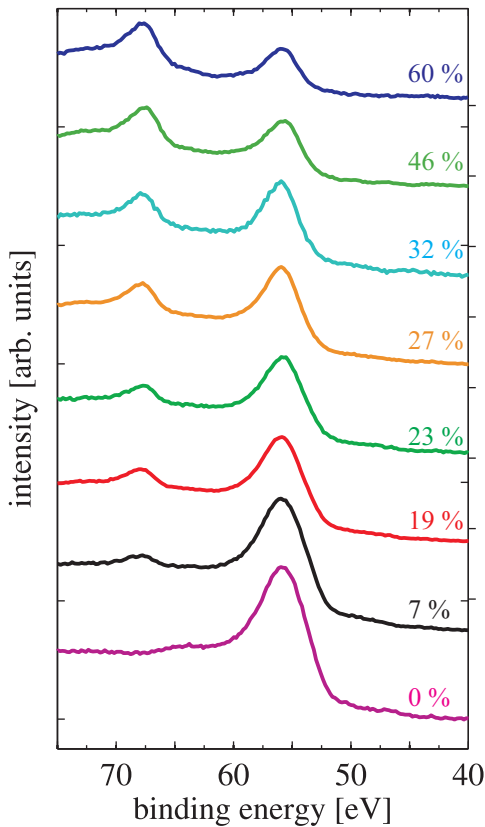


Figure 5.3.: XPS spectra of the Fe3p and Ni3p peaks for different, from bottom to top increasing, Ni/(Fe+Ni) contents. With increasing Ni/(Fe+Ni) content the Ni3p peak at 67.7 eV increases and conversely the Fe3p at 58.8 eV decreases. The sample belonging to the cyan spectra has the optimized Ni/(Fe+Ni) content desirable for NFO.

expected the Ni3p peak increases and the Fe3p peak decreases with increasing Ni/(Fe+Ni) content.

5.1.2. Analysis of the Fe2p peak

The measurement of the Fe2p spectra have been performed with the Mg-anode, since in case of the Al-anode the Fe2p peak superimposes with a Ni Auger peak. In contrast to the spin-orbit splitting of the Fe3p peak the splitting is distinct bigger in the case of the Fe2p peak and two separated peaks exist: the Fe2p_{1/2} and Fe2p_{3/2} peak. The positions of these two peaks and the occurrence of a satellite between them yield information about the oxidation state of the iron. In order to obtain the undisturbed shape of the Fe2p peak, necessary to identify the occurrence of a satellite between the two peaks the Fe2p peak is reconstructed with the program XPSPeak41 as before (see figure 5.4). Within the approximation of the Fe2p peak by using nine peaks in total it has to be excluded that the satellite arises from the K_{α3} line or the uncharged content. In addition to the two main peaks Fe2p_{1/2} and Fe2p_{3/2}, originating from the K_{α1/2} line, each of these peaks has a peak due to the uncharged content which is fixed in position, area and FWHM with regard to the main peak, and a peak resulting from the K_{α3} line. From the remaining four peaks two are satellites for the Fe³⁺- and Fe²⁺-ions fixed at 718.8 eV and 714.7 eV, respectively [30]. As in the case of the Fe3p peak there is a satellite, here at 2.65 eV above the Fe2p_{3/2} peak, to obtain the correct shape of the Fe2p_{3/2} [46], which area is held constant at 10.4% of the main Fe2p_{3/2} peak, determined by reference to magnetite.

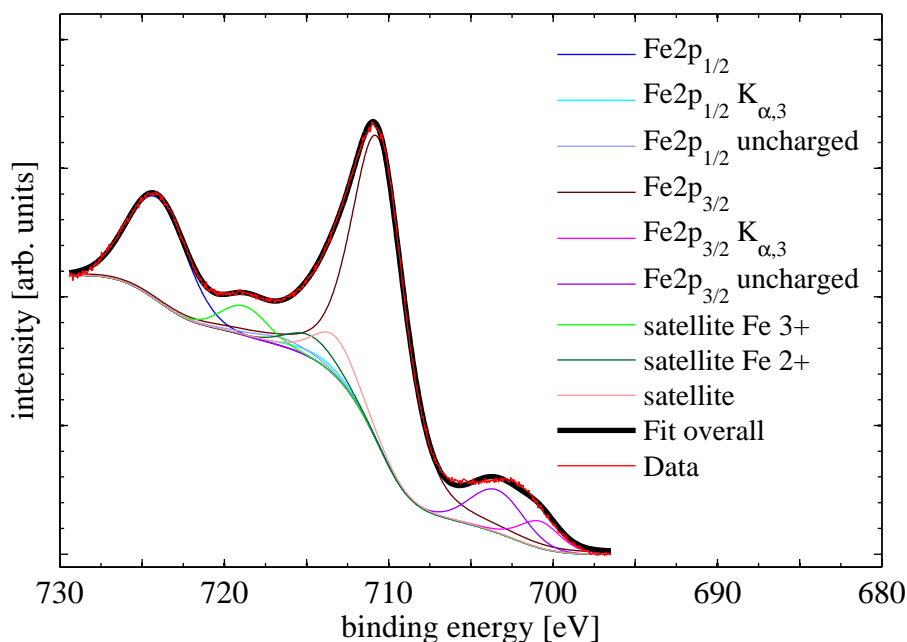


Figure 5.4.: Exemplary approximation of the Fe2p peak for the sample with a Ni/(Fe+Ni) content of 27%. The measured data (red) are reconstructed (black) by nine peaks: the two main peaks of the most intensive $K_{\alpha 1/2}$ line (blue for Fe2p_{1/2} and brown for Fe2p_{3/2}) and the $K_{\alpha 3}$ line (cyan for Fe2p_{1/2} and magenta for Fe2p_{3/2}), the peaks due to the uncharged content (blue-gray for Fe2p_{1/2} and purple for Fe2p_{3/2}), two satellites originating from Fe³⁺ (neon green) and Fe²⁺ (green) [30] and a satellite necessary to obtain the shape of the Fe2p_{3/2} peak correctly (orange).

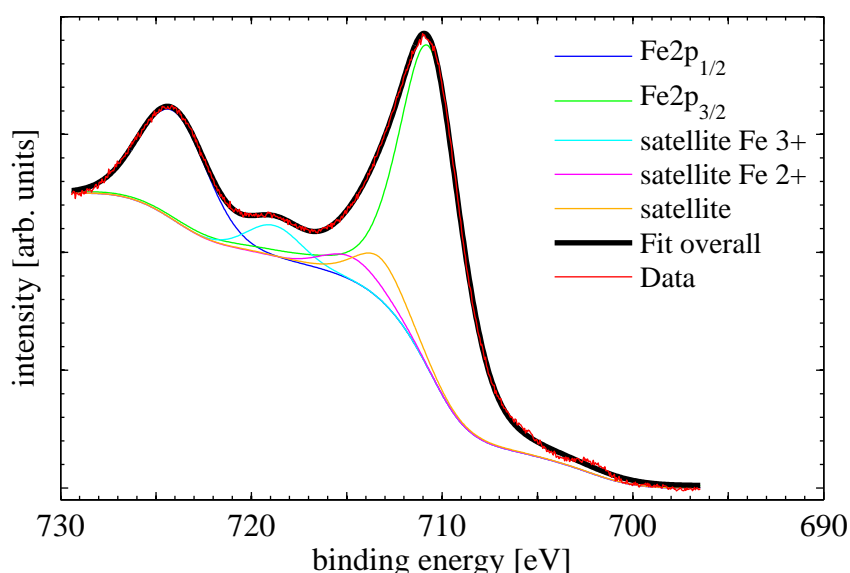


Figure 5.5.: Exemplary approximation of the corrected Fe2p peak for a Ni/(Fe+Ni) content of 27%. The spectra has been corrected about the uncharged contents of the main lines and the $K_{\alpha 3}$ lines. Thereby the shape of the peak is undisturbed and formed by the two main lines, the two peaks for the two oxidation states of iron and the additional peak to obtain the correct shape.

For the reason to be able to interpret the spectra correctly all spectra are corrected about the uncharged contents of the main lines and the $\text{K}_{\alpha 3}$ lines and result in a spectrum as shown in figure 5.5.

The satellite due to the Fe^{2+} ions is just essential for the films with low $\text{Ni}/(\text{Fe}+\text{Ni})$ contents. In perfect NiFe_2O_4 the satellite shouldn't occur, since all iron ions are in the 3+ oxidation state. When the $\text{Ni}/(\text{Fe}+\text{Ni})$ content drops below 33.3 % it is assumed that iron additionally exists in the 2+ oxidation state as it is the case in magnetite and the mentioned satellite becomes indispensable. In magnetite the satellites belonging to the two oxidation states superimpose so that in total no satellite is visible.

Figure 5.6 illustrates the corrected Fe2p spectra for some films with different $\text{Ni}/(\text{Fe}+\text{Ni})$ content. As before, the reconstructions of the peak aren't displayed to keep the figure clear. The dashed lines indicate the peak positions of the $\text{Fe}2\text{p}_{1/2}$ and the $\text{Fe}2\text{p}_{3/2}$ peak in the oxidation state of magnetite.

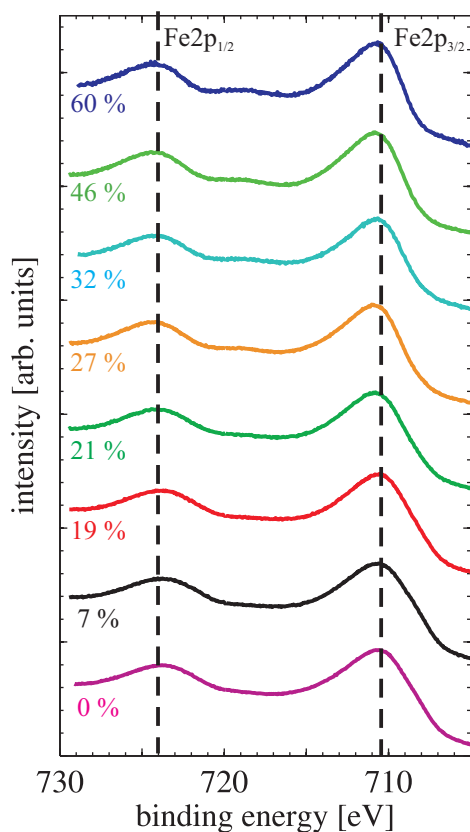


Figure 5.6.: XPS spectra of the Fe2p peak for different, from bottom to top increasing, $\text{Ni}/(\text{Fe}+\text{Ni})$ contents. With increasing $\text{Ni}/(\text{Fe}+\text{Ni})$ content both peaks, the $\text{Fe}2\text{p}_{1/2}$ and $\text{Fe}2\text{p}_{3/2}$, shift to higher binding energies. Likewise, with increasing $\text{Ni}/(\text{Fe}+\text{Ni})$ content a more and more recognizable satellite at about 718.8 eV belonging to iron in the 3+ oxidation state evolves. The sample belonging to the cyan spectra has the optimized $\text{Ni}/(\text{Fe}+\text{Ni})$ content desirable for NiFe_2O_4 . The dashed lines indicate the peak positions of the $\text{Fe}2\text{p}_{1/2}$ and the $\text{Fe}2\text{p}_{3/2}$ peak in the oxidation state of magnetite.

When comparing the corrected Fe2p spectra in figure 5.6 it is obvious that with increasing $\text{Ni}/(\text{Fe}+\text{Ni})$ content the peak positions of both peaks shift to higher binding energies in comparison to magnetite (spectra at the bottom). The peak positions of magnetite are at 724.0 eV and 710.6 eV, indicated by the dashed lines. Furthermore, a more and more recognizable satellite at about 718.8 eV belonging to iron in the 3+ oxidation state evolves with increasing $\text{Ni}/(\text{Fe}+\text{Ni})$ content. Within the reconstruction this progression is accompanied by a decrease of the Fe^{2+} satellite which vanishes at $\text{Ni}/(\text{Fe}+\text{Ni})$ contents above 32 %.

In order to have a more precise method to evaluate the oxidation state of iron inside the

films the peak positions of the $\text{Fe}2p_{1/2}$ and the $\text{Fe}2p_{3/2}$ peak have been determined and are shown in figure 5.7.

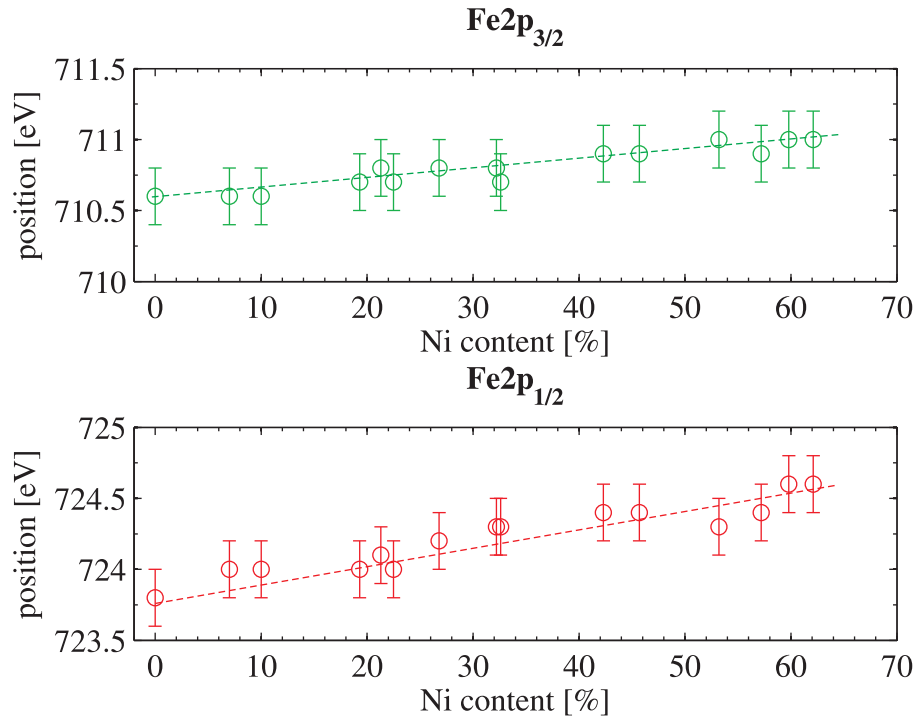


Figure 5.7.: Peak positions of the $\text{Fe}2p_{1/2}$ and the $\text{Fe}2p_{3/2}$ peak for the different $\text{Ni}/(\text{Fe}+\text{Ni})$ contents. The dashed lines indicate the trendlines for the change of the respective peak positions. With increasing $\text{Ni}/(\text{Fe}+\text{Ni})$ content the positions shift to higher binding energies and thereby to the reference positions for iron in the 3+ oxidation state as it is the case in NiFe_2O_4 .

To validate the statement of the positions and the shape of the peaks reference values and reference spectra for Fe_3O_4 (magnetite), Fe_2O_3 (maghemite) and FeO (wustite) are given in table 5.2 and in figure 5.8. The latter just contains iron in the 2+ oxidation state, maghemite just iron in the 3+ oxidation state, as it should be in perfect NiFe_2O_4 , and magnetite contains both (one third 2+ and two thirds 3+).

iron oxide	Fe $2p_{1/2}$ [eV]	Fe $2p_{3/2}$ [eV]	satellite [eV]
Fe_3O_4	724.0	710.6	—
Fe_2O_3	724.6	711.0	719
FeO	722.6	709	714.7

Table 5.2.: Peak and satellite positions of the iron oxides magnetite (Fe_3O_4), maghemite (Fe_2O_3) and wustite (FeO) [30].

Considering both the peak positions and the satellites, it is obvious, that for low $\text{Ni}/(\text{Fe}+\text{Ni})$ contents the oxidation state of iron in the samples is magnetite likely and for $\text{Ni}/(\text{Fe}+\text{Ni})$ contents above 32% iron more and more exists in the pure 3+ oxidation state. The satellite at 714.7 eV, indicating iron in the pure 2+ oxidation state, like it can be seen in the

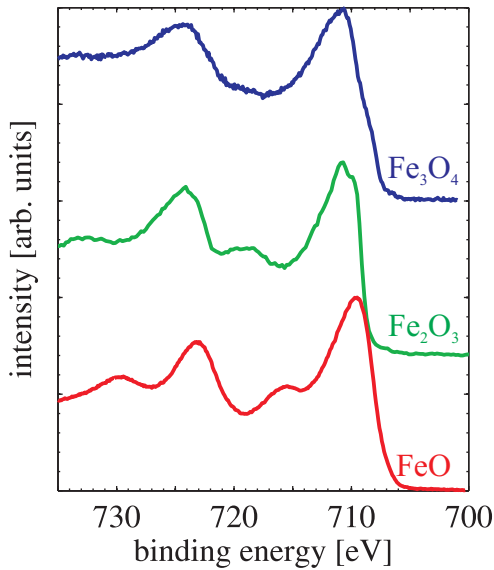


Figure 5.8.: Reference spectra of the iron oxides magnetite (Fe_3O_4) [48], maghemite (Fe_2O_3) [48] and wustite (FeO) [49].

reference spectra of FeO , isn't recognizable for all samples. So, the films reveal iron in the 3+ oxidation state for $\text{Ni}/(\text{Fe}+\text{Ni})$ contents above 32 % and magnetite likely composition, hence 3+ and maximal one third 2+ ions, for lower contents.

5.1.3. Analysis of the Fe3s peak

The shown and analyzed 3s spectra have been measured with the Al-anode. The Fe3s peak is splitted into one main line at about 93 eV and a quite intensive satellite at about 100 eV. On the higher binding energy side the Ni3s peak is positioned which is also splitted into a main line at about 112 eV and a satellite at about 117 eV. The binding energy difference between the respective main line and the satellite is defined as the exchange splitting (compare chapter 2.5.3). The progression of the splitting with varying $\text{Ni}/(\text{Fe}+\text{Ni})$ contents provides information about the change of the oxidation state of the two elements in dependence of the $\text{Ni}/(\text{Fe}+\text{Ni})$ content. In order to quantify the exchange splitting of both cations the spectra are reconstructed in the same way as before. In total ten peaks are used: the Ni3s and Fe3s main line and their satellites due to the exchange splitting with apart from the Fe3s main line their respective uncharged content fixed by the values determined within the approximation of the O1s peak and their contribution of the $\text{K}_{\alpha 3}$ line. The uncharged content and the contribution of the Fe3s main line don't superimpose with the other peaks and aren't considered for this reason. An example of the reconstruction of the Fe3s and Ni3s peak, which is corrected about the uncharged contents and the contributions of the $\text{K}_{\alpha 3}$ line, is presented in figure 5.9. In figure 5.10 the Ni3s and Fe3s spectra for different, from bottom to top increasing, $\text{Ni}/(\text{Fe}+\text{Ni})$ contents are illustrated without their reconstructions. As expected, the Ni3s peak increases and the Fe3s peak decreases with increasing $\text{Ni}/(\text{Fe}+\text{Ni})$ content. A change in the asymmetry

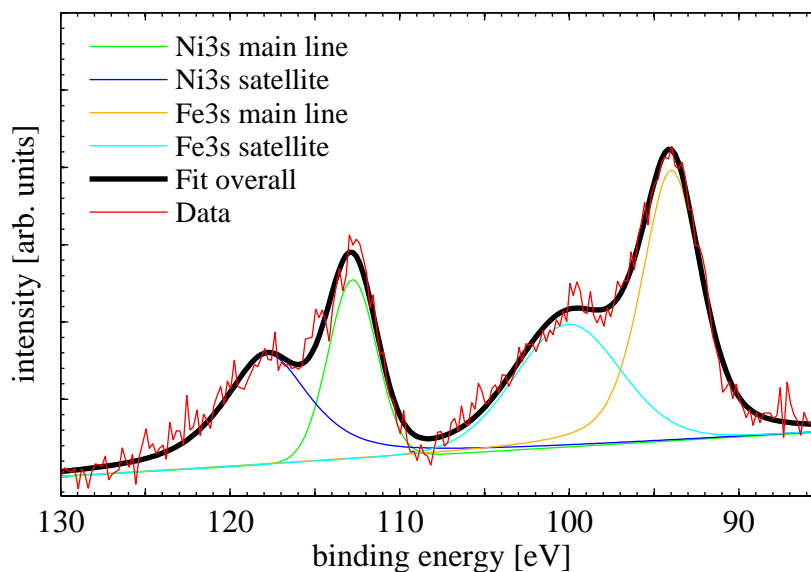


Figure 5.9.: Exemplary reconstruction of the Fe3s and Ni3s peak for a Ni/(Fe+Ni) content of 32%. The contributions of the uncharged content and the $K_{\alpha 3}$ line have been subtracted to receive the real shape of the two asymmetric 3s peaks. The two asymmetric 3s lines consist of the Ni3s main line (green), the Ni3s satellite due to the exchange splitting (blue), the Fe3s main line (yellow) and its satellite (cyan).

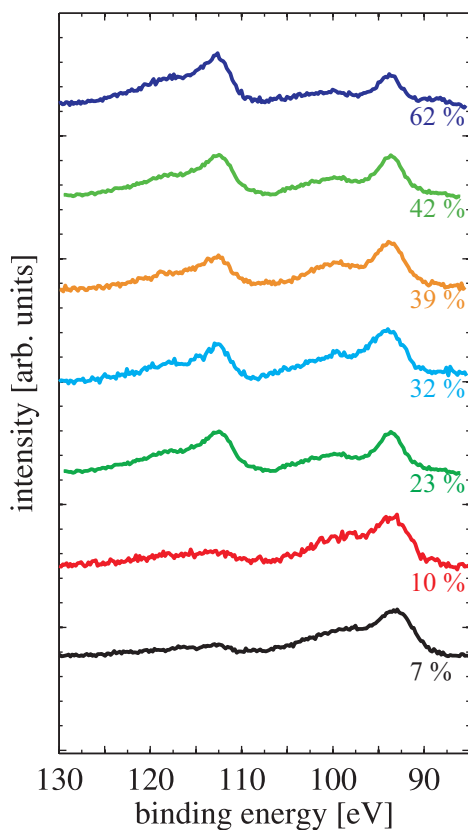


Figure 5.10.: XPS spectra of the Ni3s and Fe3s peak for different, from bottom to top increasing, Ni/(Fe+Ni) contents. With increasing Ni/(Fe+Ni) content the Ni3s peak at about 112 eV increases and conversely the Fe3s at about 93 eV decreases. The progress of the exchange splitting is not recognizable without the reconstructions. The sample belonging to the cyan spectra has the optimized Ni/(Fe+Ni) content desirable for NFO.

and thereby in the exchange splitting is not recognizable with the unaided eye and the analysis of the reconstruction is required, which is shown in figure 5.11.

The analysis of the reconstruction shows that the exchange splitting in the Fe3s peak starts with about 5.3 eV for a Ni/(Fe+Ni) content of 7% and goes more or less continuously up to a value of about 7 eV at a Ni/(Fe+Ni) content of 60%. The progression is indicated by a trendline in figure 5.11. For the NFO likely film with 32% nickel the splitting comes to 6.1 eV. In the literature the following experimental values for the splitting can be found for the different oxidation states of iron: Fe^{2+} about 5.4 eV, Fe^{3+} about 6.3 eV and about 7 eV for Fe^{4+} [34].

That means that for low nickel contents the exchange splitting is at the value for Fe^{2+} , at perfect NFO at the value for Fe^{3+} and for high nickel contents even goes close to the value of Fe^{4+} . Even though the oxidation state of the iron of the films with low and high nickel contents can't be completely 2+ and 4+ respectively with regard to the magnetite structure confirmed by the XRD measurements (compare chapter 5.4) the tendency of the exchange splittings underlines the results from the Fe2p spectra. A low nickel content means some iron is in the 2+ oxidation state and for perfect NFO there is just 3+ which coincides well with the value determined by the Fe3s splitting. For nickel contents higher than 32% the splitting points on the occurrence of Fe^{4+} , which are unlikely to be formed, so the results of the splitting have to be treated with caution. Nevertheless, the tendency of an increasing oxidation state of iron with an increasing nickel content goes along with the results from the analysis of the Fe2p spectra.

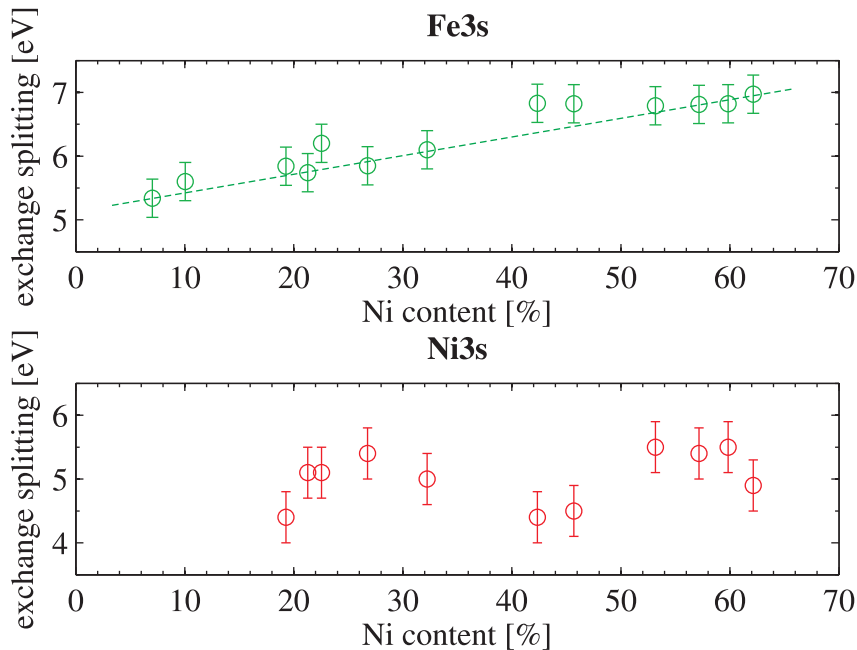


Figure 5.11.: Exchange splitting of the Fe3s and Ni3s peak. The dashed line in the illustration at the top indicates the trendline of the exchange splitting of the Fe3s peak which increases with rising Ni content from around 5.3 eV to about 7 eV. The exchange splitting of the Ni3s peak exhibits some variations which are still in the scope of the errorbars of the other points. No moderate trend is obvious.

The exchange splitting of the Ni3s peak changes less than the one of the Fe3s peak and within the scope of the error bars there is no change in the oxidation state, so it should be 2+ over the whole range of nickel contents.

5.2. LEED results

LEED measurements have been performed on all cleaned substrates and on every prepared film in an electron energy range of 110 eV to 250 eV in order to characterize the crystal surface structure.

The diffraction pattern for all MgO(001) substrates look the same, so in figure 5.12 one LEED image of a MgO substrate is shown exemplarily. The electron energy used for all in the following shown LEED images is 111 eV.

The LEED image of the substrate illustrates a (1×1) structure, which arises from the quadratic surface unit cell of the MgO. Since the diffraction spots are sharp and clearly distinguishable from the background the heated surface of the substrate exhibits a well-ordered, crystalline structure.

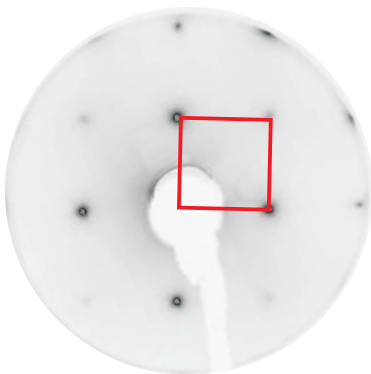


Figure 5.12.: Exemplarily LEED image of a MgO(001) substrate. The image is taken with an electron energy of 111 eV and reveals the (1×1) structure (red) of the quadratic surface unit cell.

The LEED patterns of the films with varying Ni/(Fe+Ni) content don't display large differences. In figure 5.13 the LEED patterns of three films with different nickel contents are presented. The nickel contents in the shown films are above the optimal (a - 53%), below the optimal (c - 10%) and nearly within the optimal value of 33.3% (b - 33%).

All films clearly reveal the (1×1) structure of the film material (blue) which unit cell length is 8.34 Å in the case of stoichiometric NiFe₂O₄. In addition, the twice as big reciprocal unit cell of the substrate material MgO is indicated (red). For the reason that MgO has a unit cell length of 4.2117 Å in real space the structure of the film appears half as large as the one of MgO in reciprocal space, thus in the LEED image. The film c) with a pretty low nickel content furthermore features slightly the $(\sqrt{2} \times \sqrt{2})R45^\circ$ superstructure (green) which is characteristic only for the iron oxide magnetite [50]. Figure 5.14 shows a LEED pattern of a magnetite film grown on MgO(001) in order to compare the pattern to the film with a nickel content of 10%.

Beside the arrangement of the diffraction spots one can analyze the size of the diffraction spots. The sharper the spots, the higher is the crystalline quality of the surface. When

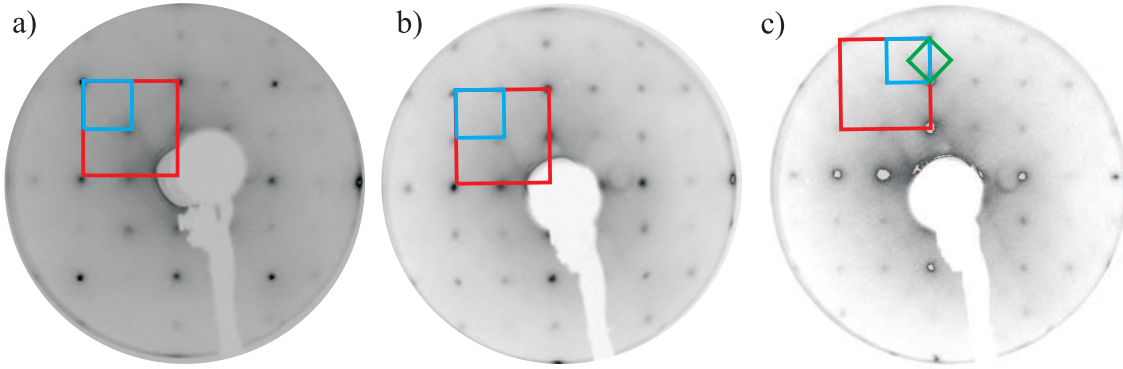


Figure 5.13.: LEED patterns of films with nickel contents of 53% (a), 33% (b) and 10% (c), all taken at an electron energy of 111 eV. All films reveal the (1×1) structure (blue) of the quadratic surface unit cell of the iron oxide $\text{Ni}_x\text{Fe}_{3-x}\text{O}_4$ ($0 < x < 1$). Moreover, the unit cell of the substrate material MgO is indicated in red. The length of the unit cell of the iron oxide is halved with respect to the one of MgO, since in real space it's the other way around. The film c) with a pretty low nickel content furthermore features slightly the $(\sqrt{2} \times \sqrt{2})\text{R}45^\circ$ superstructure (green) which is characteristic for the iron oxide magnetite [50].

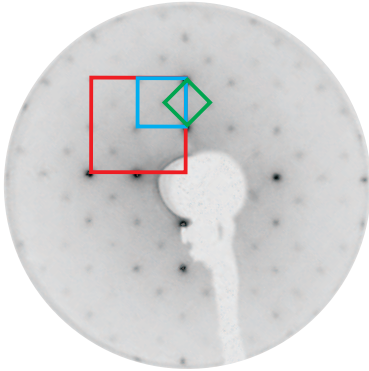


Figure 5.14.: Exemplarily LEED image of a magnetite film grown on MgO(001). The image is taken with an electron energy of 111 eV and reveals the (1×1) structure of all iron oxides (blue) and a clear $(\sqrt{2} \times \sqrt{2})\text{R}45^\circ$ superstructure (green) which is characteristic only for the iron oxide magnetite [50]. Furthermore, the unit cell of the substrate material MgO is indicated (red).

looking at all shown LEED images one could think that the MgO has the worst crystalline quality but in this case the spots are broadened because MgO is an insulator which means that charging effects on the fluorescence screen are responsible for the broadening. Comparing the spot sizes of the three films it seems as if the NFO likely film (b) has slightly sharper spots than the other two maybe indicating a gently higher crystalline quality at the surface.

To conclude it can be said that all films exhibit a surface with a high crystalline quality and the (1×1) structure typical for all iron oxides. The film with a very low nickel content shows a weak $(\sqrt{2} \times \sqrt{2})\text{R}45^\circ$ superstructure in addition which suggests that the Ni^{2+} ions are replaced by Fe^{2+} ions in that film at least at parts of the surface. If the magnetite likely structure present at the surface is reaching further in the film can't be said from the LEED measurements, since it is extremely surface sensitive.

5.3. XRR-Results

The analysis of the XRR measurements have been carried out with the software "iXRR" (compare reference [20]). Thereby, the measured data is reconstructed by adjusting the complex refraction indices, the roughnesses of the substrate and the film and the film thickness. The results of the refraction indices and the roughnesses are secondary. The primary focus is on the film thickness of the prepared samples. In figure 5.15 the XRR measurements and their reconstruction of some samples with Ni contents between 7% and 46% are illustrated.

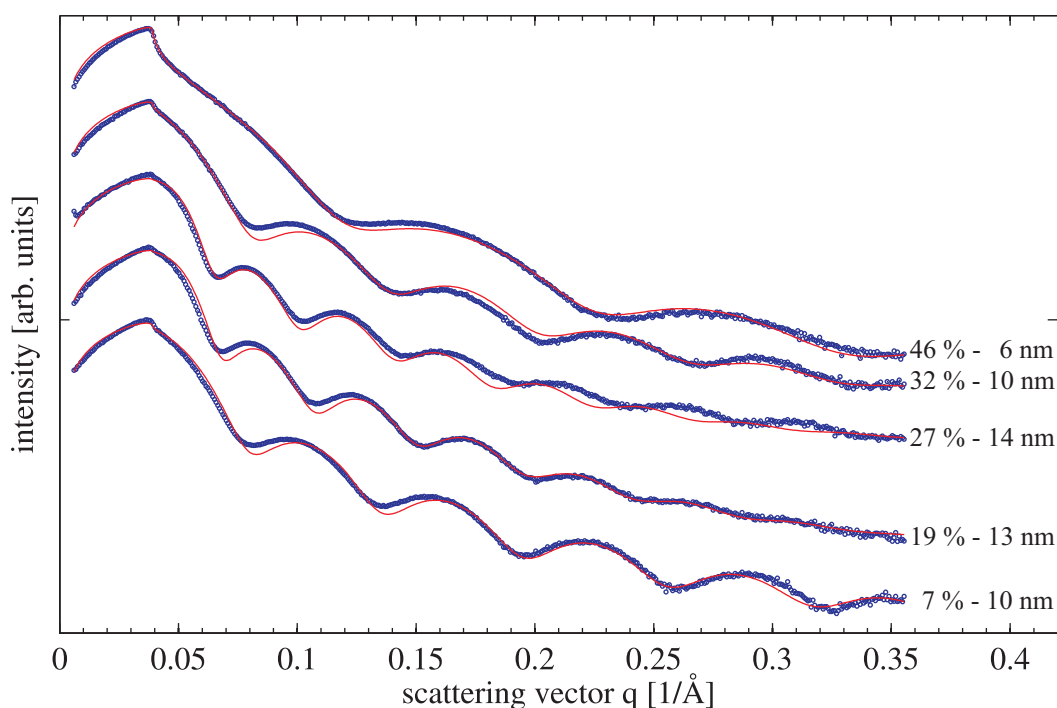


Figure 5.15.: Exemplary XRR measurements and their reconstruction. The blue points indicate the measured data while the red line represents the approximation. Depending on the film thickness, stated behind each curve, the periodicity of the oscillations is larger or smaller. The reconstructions coincide very well with the measured data.

According to the film thickness the periodicity of the oscillations is larger or smaller. The reconstructions of all shown samples coincide very good with the measured data and the adapted values for the complex refraction index of the film on top of the substrate correspond to the literature values for nickel ferrite. The parameters of the reconstructions and the literature values for the refraction index are shown in the appendix (see A.0.1.). The film thickness d of all prepared films have already been given in tables 4.1 and 4.2 in chapter 4.3 where all samples have been listed with their growth parameters. The thinnest and thickest film prepared on MgO reveal a thickness of 7 nm and 39 nm, respectively.

5.4. XRD results

5.4.1. Analysis of the data

Within the XRD measurements the 2D detector records one image for each incidence angle. The analysis of these 2D images has been performed with the program "ImageStack". Figure 5.16 illustrates the principle the program uses for the analysis. A rectangle, the region of interest (ROI), is chosen and its position and size is inherited for all images. The intensities of all pixels within this ROI are summarized for each image and yield in one data point for the respective incidence angle. A second ROI can be placed outside of the reflexes in order to subtract a background. As already mentioned in chapter 4.2 the angle of incidence and reflection are changed during the progress of a measurement which leads to the movement of the reflexes through the images (compare figure 5.16).

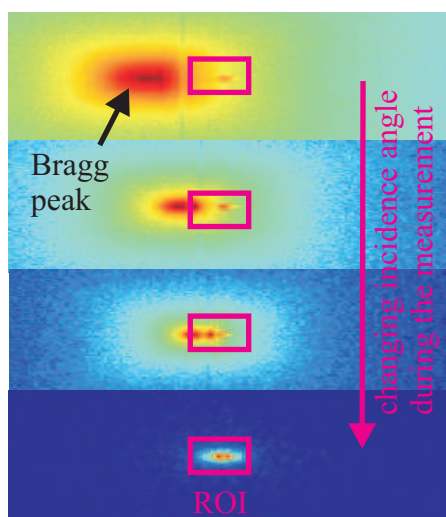


Figure 5.16.: Exemplary illustration of the analysis of the images recorded by the 2D detector. During the progress of the measurement, with the change of the incidence angle, the Bragg peaks move through the detection area. On each image belonging to the respective incidence angle a region of interest (ROI) with fixed position and size is placed. The position and size of the ROI is chosen on the basis of the image belonging to the incidence angle with the most intensive Bragg peak. The intensities of the pixels inside the ROI are summarized for each image and build the data point for the respective incidence angle.

The advantage of a 2D-detector over a point detector is that a wide range of the reciprocal space can be scanned in one measurement while for a point detector several measurements are necessary to obtain the similar information such as the shape of a reflex. Moreover, the summarized intensities from the 2D detector are more convenient for quantitative analysis, since the better statistic of the large detection area reduces insecurities and fluctuations.

5.4.2. (002)- and (004)-reflexes

The data points obtained from the 2D images are reconstructed with the help of the program "RodsNPlots" (for more information see [51]) after the angles of reflection have been converted into positions in the reciprocal space. In figure 5.17 the XRD measurements of three samples with Ni contents between 53 % and 60 % are shown for $1.7 < L < 2.3$ in relative lattice units on the basis of MgO(001).

The extract of the (00L)-rod looks quite equal for the three measured samples with the

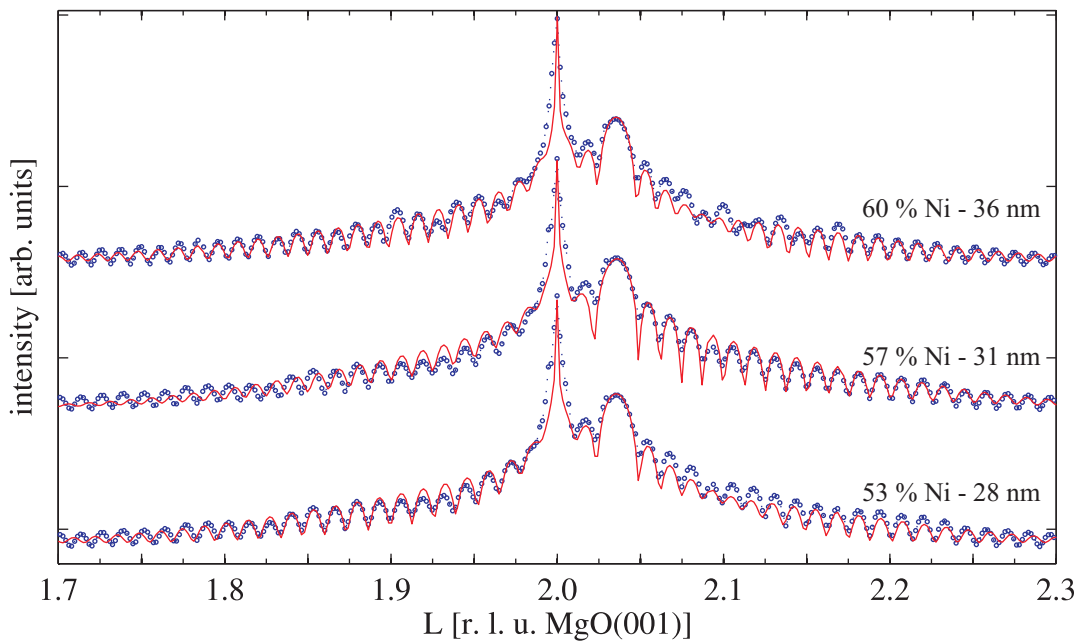


Figure 5.17.: XRD measurement of the (002)-reflex of MgO for three samples with a Ni content between 53% and 60%. The blue points show the measured data while the red lines are the reconstructions made with the program "RodsNPlots". The position and shape of the (002)-reflex and the film peak on the right side of the substrate peak don't differ for the three samples. The data of all three samples show distinct fringes.

(002)-reflex of the substrate at $L = 2$ and the film peak at around $L = 2.035$. Furthermore, all three samples exhibit clear fringes.

A second extract of the (00L)-rod from $3.9 < L < 4.3$ belonging to two of the three shown samples is illustrated in figure 5.18. For MgO the (001)- and (003)-reflexes are so called "forbidden reflexes". The structure of the unit cell leads to the cancellation of the intensities at those positions in the reciprocal space.

The measured data around the (004)-reflex of MgO of both samples look quite equal with regard to position and shape of the substrate and film peak. In both cases fringes are recognizable. On the left side of the substrate peak the reconstruction and the measured data deviate with regard to the intensity of the fringes.

From the position L_{film} of the film peak the out-of-plane layer distance c_{film} of the film can be calculated:

$$c_{\text{film}} = \frac{L_{\text{substrate}} \cdot c_{\text{substrate}}}{L_{\text{film}}}. \quad (5.1)$$

Here $L_{\text{substrate}}$ and $c_{\text{substrate}}$ are the position of the substrate peak and the substrate out-of-plane layer distance.

One parameter the program "RodsNPlots" adapts within its calculations is the number of layers the film is made of. The lower the number of layers the greater the periodicity of the crystal oscillations (fringes). With the knowledge of the structure of the unit cell of the film material the number of layers can be converted into the film thickness d_{crys} .

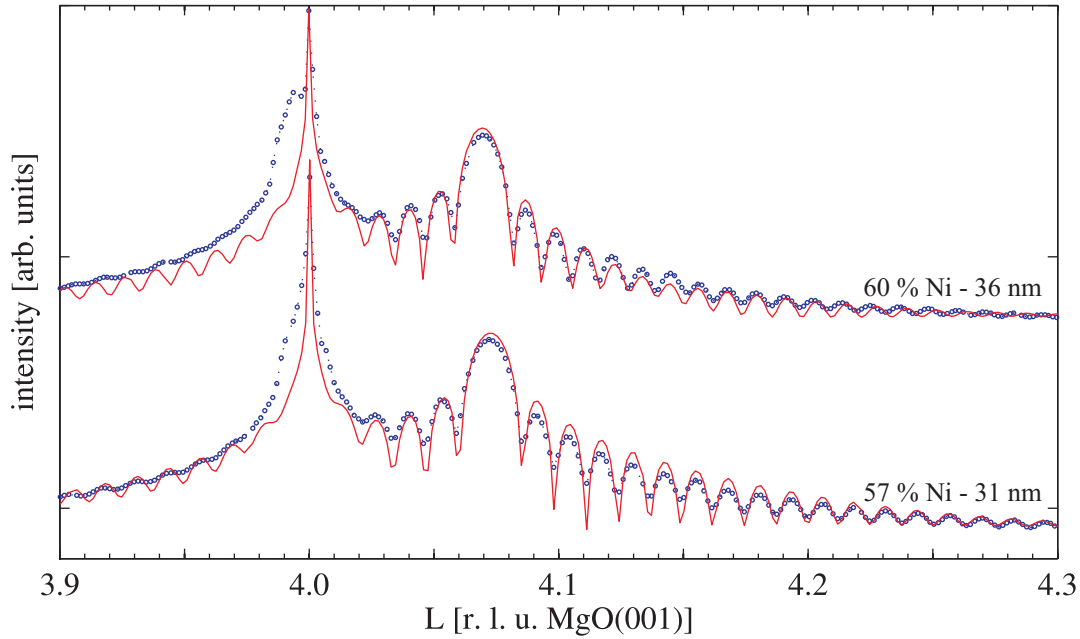


Figure 5.18.: XRD measurement of the (004)-reflex of MgO for two samples with Ni contents of 57% and 60%. The blue points show the measured data while the red lines are the reconstructions made with the program "RodsNPlots". The position and shape of the (004)-reflex and the film peak on the right side of the substrate peak don't differ for the two samples. The data of the two samples show fringes. On the left side of the substrate peak the reconstruction and the measured data deviate with regard to the intensity of the fringes.

In contrast to the film thickness d determined within the XRR measurement the film thickness d_{crys} is the film thickness of solely the crystalline part of the film. The reason behind this is that the detected intensity in XRD measurements consists of the x-rays scattered at the periodically arranged crystal planes which means there is no contribution from amorphous parts of the film. In XRR measurements the reflections at the interfaces occur due to a difference in the electron densities of the materials adjacent to one another. Since the electron density is the same for amorphous and crystalline parts of the films the film thickness d determined by an XRR measurement includes both contributions. Based on the previous explanation the film thickness d , originating from an XRR measurement, should be at least as big as the film thickness d_{crys} , obtained from an XRD measurement.

In table 5.3 the positions $L_{\text{substrate}}$ and L_{film} of the substrate and film peak, the resulting out-of-plane layer distance a_{film} of the film, the crystalline film thickness d_{crys} and for comparison the film thickness d are listed.

The out-of-plane layer distance c_{film} of the film is about 2.07 \AA for all three films.

Consequently, the observed out-of-plane layer distance c_{film} of all films are about 0.7% smaller than the value of $c_{\text{NiFe}_2\text{O}_4} = 2.085 \text{ \AA}$ from the literature [1]. Nickel ferrite has a Poisson ratio ν of 0.35 [52], so the volume of the unit cell is maintained in case of a deformation of the crystal lattice. Keeping in mind the lattice mismatch of 1% between

Bragg reflex	Ni/(Fe+Ni) content [%]	$L_{\text{substrate}}$ [r.l.u. MgO(001)]	L_{film} [r.l.u. MgO(001)]	c_{film} [Å]	d_{crys} [Å]	d [Å]
(002)	60	2	2.035	2.0695	35±1	36±3
	57	1.9998	2.036	2.0685	34±1	31±3
	53	2.0018	2.035	2.0715	32±1	28±3
(004)	60	3.9998	4.069	2.07	35±1	36±3
	57	4.0002	4.072	2.0685	34±1	31±3

Table 5.3.: Summary of the XRD results. $L_{\text{substrate}}$ and L_{film} are the positions of the substrate and film Bragg peak on the L-axis in the reciprocal space, c_{film} the out-of-plane layer distance of the film and d_{crys} and d the film thickness obtained by XRD and XRR.

MgO(001) and nickel ferrite, so a tensile strain of the nickel ferrite in in-plane direction, the result of a compressive strain in out-of-plane direction is reasonable.

The second aspect unfolded by the XRD measurements is that all three analyzed films are completely crystalline, since the film thicknesses d_{crys} and d determined by XRD and XRR coincide within the scope of the errors of measurement. That implies that the three films are free of amorphous parts even though there is too much nickel with regard to a perfect nickel ferrite structure.

5.5. Discussion

In this chapter the results obtained from all performed measurements are discussed and related to each other.

According to the quantitative analysis of the Fe3p and Ni3p peaks the perfect Ni/(Fe+Ni) ratio for the RMBE preparation of stoichiometric nickel ferrite at an oxygen atmosphere of 5×10^{-6} mbar and a substrate temperature of 250 °C has been obtained with evaporation powers of 27.5 W and 36-39 W for the Ni and Fe effusion cells, respectively. The analysis of the Fe2p and Fe3s spectra reveal that below a Ni content of 33% the oxidation state of the iron is not purely 3+, as it should be in perfect nickel ferrite, whereas for Ni contents above the optimal value of 33% the oxidation state of the iron more and more goes to purely 3+. This statement is made on the basis of the peak positions of the Fe2p_{1/2} and Fe2p_{3/2} peak which shift with increasing Ni content from the respective values for magnetite to the values for maghemite, where all iron is in the 3+ oxidation state [30] (compare figure 5.7). At the optimal Ni content the shift towards the positions of Fe³⁺ is completed within the scope of the errorbars. A second feature for the oxidation state of the iron are the respective satellites for Fe³⁺ and Fe²⁺ ions located at about 719 eV and 715 eV in the Fe2p spectra. Within the reconstruction of the Fe2p spectra the Fe²⁺ satellite has been unrenounceable up to a Ni content of 32% in order to receive the correct shape of the spectra. Looking at the total shape of the spectra (compare figure 5.6), the Fe³⁺ satellite emerges and intensifies starting from a Ni content of 27%. Below that Ni content the satellites belonging to the two oxidation states offset each other since both ions exist parallel, like in magnetite.

This result from the Fe2p spectra is underlined by the analysis of the exchange splitting in the Fe3s spectra. Here, too, a small Ni content accompanies a low splitting in the Fe3s spectra (compare figure 5.11), meaning a low oxidation state, which increases with increasing Ni content and reaches the value for Fe^{3+} at a Ni content of 32 %. The described progression goes on for Ni contents above 32 %, indicating that the oxidation state of iron is even higher than 3+. With regard to the current material system that can't take place so the Fe3s splitting can't be used solely to determine the oxidation state of iron. But since it coincides with the Fe2p analysis, it can be said that at a Ni content of 32 % the iron exists in the 3+ oxidation state. According to the splitting in the Ni3s spectra its oxidation state stays constant at 2+ over the whole range of analyzed Ni contents (compare figure 5.11).

The LEED measurements confirm a well structured surface of all films since a clear (1×1) structure is visible. With regard to the unit cell length of the substrate MgO the reciprocal unit cell length of the (1×1) structure of the films is halved. This is associated with the inverse lengths ratio of the two considered unit cells in real space. For Ni contents below 10 % an additional $(\sqrt{2} \times \sqrt{2})\text{R}45^\circ$ superstructure, characteristic for the iron oxide magnetite [50], suggests that magnetite exists at the surface or that small amounts of nickel don't disturb this superstructure (compare figure 5.13).

The XRR measurements have only been executed to determine the film thickness and to check whether the films consist of one material with the same refraction index or if several layers exist. The measured data of all films have been reconstructed by one single layer with the refraction indices for nickel ferrite [53].

The XRD results show a high crystallinity of the three analyzed films with Ni contents between 53 % and 60 % since distinct fringes are recognizable. The number of layers necessary to obtain the periodicity of the fringes, indicating the crystalline part of the film, go along with the film thicknesses determined by the XRR measurements. Within the scope of the inaccuracy of measurement the two values coincide and the whole films are crystalline.

The out-of-plane layer distance of all prepared films on MgO is 2.07 \AA which is slightly smaller than the bulk out-of-plane layer distance of nickel ferrite, which has a value of 2.085 \AA .

The relation

$$\frac{\Delta c_{\text{film}}}{c_{\text{film}}} = \frac{2\nu}{\nu - 1} \cdot \frac{\Delta a_{\text{film}}}{a_{\text{film}}} \quad (5.2)$$

can be used to calculate the expected deformation Δc_{film} of the out-of-plane layer distance c_{film} of the film. Here ν is the poisson ratio, a_{film} the bulk in-plane lattice constant of the film material and Δa_{film} the difference between the bulk lattice constants of the film and the substrate material.

On the assumption that nickel ferrite grows pseudomorphically on MgO, meaning nickel ferrite adapts the in-plane lattice constant predefined by the MgO lattice, the expected Δc_{film} has a value of -0.025 \AA . This results in an out-of-plane layer distance of 2.06 \AA . Keeping in mind that the Ni content of the investigated films is higher than in stoichiometric NiFe_2O_4 this result is in good agreement with the value of 2.07 \AA obtained through the XRD measurements.

Hence, the tensile strain of the films in in-plane direction is compensated by a compressive strain in out-of-plane direction and the films are nearly completely strained.

The strain in both directions should decrease with the stable formation of dislocations above the critical thickness h_c [54]:

$$h_c = b \cdot \frac{(1 - \nu \cdot \cos^2(\alpha))(\ln(\frac{h_c}{b}) + 1)}{2\pi\epsilon(1 + \nu) \cdot \cos(\alpha)}. \quad (5.3)$$

Here $b = \frac{a_{\text{NFO}}}{\sqrt{2}}$ is the magnitude of the Burgers vector, $\epsilon = 0.001$ the lattice misfit between NFO and MgO, $\alpha = 90^\circ$ the angle between the dislocation line and the Burgers vector, $\lambda = 45^\circ$ the angle between the Burgers vector and the direction that is both normal to the dislocation line and that lies within the plane of the interface and $\nu = 0.35$ the Poisson ratio [52].

The resulting value of the critical thickness h_c is 20.3 nm which is roughly half of the film thickness of the three films so the films should exhibit strain relaxation. Since the growth of nickel ferrite on MgO is rarely studied so far, a comparison concerning the strain relaxation is made with respect to the system $\text{Fe}_3\text{O}_4/\text{MgO}(001)$, because the structure is identical and the lattice constant of magnetite is comparable to that of nickel ferrite. The observation that the magnetite films stay unrelaxed far above the critical thickness is made from several other groups. Arora et al. report about strain relaxation in the considered system, likewise deposited by RMBE, starting at film thicknesses of 700 nm even though the theoretical predicted critical thickness is 70 nm [55]. Furthermore, Schuckmann et al. reveal data for a compressed out-of-plane lattice constant of magnetite films grown on MgO up to film thicknesses of 120 nm which show no relaxation [56]. The explanation of Arora et al. for the missing relaxation are the differences in the crystal structure symmetry between magnetite and MgO. They suggest that the lower crystal symmetry of the inverse spinel structure of magnetite compared to that of MgO leads to the formation of antiphase boundaries (APBs) and thereby areas within the films that have opposite signs of stress, which would reduce the effective stress impacting on the films. Consequently, the formation of APBs may reduce the stress within the films and they maintain lattice matching between film and substrate at large thicknesses.

Due to the similarities between the two materials magnetite and nickel ferrite it seems reasonable with the drawn comparisons that nickel ferrite on MgO stays strained for film thicknesses above the critical one.

Surprising is the previously mentioned observation that the three films with too high Ni contents between 53 % and 60 % are completely crystalline according to the XRD reconstructions and that the XRR reconstructions could be done with one single layer. In nickel ferrite the Ni^{2+} ions occupy the sites which are taken by Fe^{2+} in magnetite. If the amount of nickel inside the films is higher than the expected stoichiometric amount one would estimate that the structure is disturbed in some way for example by interstitials, since the excess nickel has to be located somewhere. Improbable is the replacement of Fe^{3+} ions by Ni^{2+} ions since the charge wouldn't be balanced in that case and Ni doesn't exist in the 3+ oxidation state. Imaginable would be the replacement of Fe^{3+} ions by Ni^{2+} ions with a simultaneous formation of dislocations of Fe^{3+} sites in order to maintain the charge balance over a larger volume. Considering the extent of the Ni excess, about 56 % instead of 33 %, this reorganization of the sites would lead to XRD results differing from

the obtained inverse spinel structure. That's why the excess Ni has to go somewhere else. The formation of a second layer on top of the film or below seems to be unlikely due to the XRR measurements which can be reconstructed by a single layer. Kuschel et al. report about NiO grains or clusters at the surface of $\text{Fe}_3\text{O}_4/\text{NiO}/\text{STO}(001)$ systems arising from Ni interdiffusion caused by annealing [57]. Perhaps the excess Ni forms clusters inside the well structured films but then one would expect a disturbance of the crystallinity in some way.

Summarizing, it can be stated that according to the XPS results the stoichiometric deposition of nickel ferrite has been successful and that the oxidation state of iron in that composition is 3+. The ordering at the surface as well as the ordering in out-of-plane direction is very good for the analyzed samples which all exhibit too much nickel. The films, assumed to grow pseudomorphically and thereby tensile strained on MgO, exhibit a compression in out-of-plane direction which maintains for film thicknesses above the critical thickness of strain relaxation. The films analyzed by XRD, all showing a distinct amount of excess nickel, seem to be completely crystalline and consisting of one single layer. Where and in which form the excess nickel is located has to be solved in further investigations.

The next step within the analysis of the growth of nickel ferrite on MgO is going to be the determination of the magnetic properties by vibrating sample magnetometry (VSM) in order to specify the relation between the Ni content and the magnetic behaviour. X-ray magnetic circular dichroism (XMCD) would reveal more detailed information concerning the cationic valencies and their spatial coordination and could confirm the oxidation state of iron and maybe solve the question of the excess nickel. As mentioned within the introduction theoretical calculations predict a high magnetic permeability and insulating properties for nickel ferrite which are important for the application of nickel ferrite in the thermoelectric power generation or in spin-filters. Consequently, it would also be interesting to examine the electrical conductance of the prepared samples. In order to investigate the morphology and interface properties of the nickel ferrite films it would be interesting to perform image-generating measurements like atomic-force microscopy (AFM) and transmission electron microscopy (TEM) to analyze possible APBs [55].

6. Results and discussion of NiFe_2O_4 films grown on SrTiO_3

The performed measurements and their results for the growth of nickel ferrite on STO are illustrated in this chapter. For the reason that the Ni content has been optimized during the growth on MgO and now on STO the film thickness has been varied, the main focus of the analysis is on the XRD measurements instead of the XPS measurements. The XPS measurements, displayed in chapter 6.1, have been performed in order to check that the composition of the films and the oxidation states of the cations stay constant. The results, taken from the LEED images of the films, are shown and interpreted in chapter 6.2. Afterwards the XRR results are summarized in chapter 6.3. The results from the XRD measurements, presented in chapter 6.4, reveal information about the ordering of the crystal in out-of-plane direction. The discussion of all results in chapter 6.5 completes this chapter.

6.1. XPS results

The XPS measurements for the growth of nickel ferrite on STO don't reveal new information since the stoichiometry of the films has already been optimized for the respective growth on MgO. So, the Fe3p and Ni3p peaks have been interpreted quantitatively to verify the stoichiometry while the qualitative analysis of the Fe2p spectra confirm the oxidation state of the iron inside the films. The reconstruction of all spectra have been implemented as for the spectra on MgO (see chapter 5.1) with the only difference that on STO no charging effects exist, so that within the reconstruction no peaks due to charging have to be considered.

On the left-hand side in figure 6.1 the Fe3p and Ni3p peak of the five films on STO and of a comparable film on MgO, corrected about the peaks arising from the $\text{K}\alpha_3$ line, are shown. For the reason of clarity the corrected spectra without their reconstructions are displayed for the films, all exhibiting Ni contents between 27% and 33%. The film thickness increases from the bottom to the top. The corrected Fe2p spectra of the films on STO, and for comparison of the film on MgO in which the Ni content is optimized, are presented on the right-hand side in figure 6.1.

The Fe3p and Ni3p spectra of the films on STO and of the film on MgO, measured with the Al-anode, are equal with regard to the peak positions and relative peak areas.

The Fe2p spectra, measured with the Mg-anode, reveal slight variations in the peak positions but within the inaccuracy of measurement all positions coincide. The $\text{Fe}2\text{p}_{1/2}$ peak of all films is positioned at 724.4 ± 0.3 eV and the $\text{Fe}2\text{p}_{3/2}$ peak at 710.8 ± 0.2 eV. Furthermore, a satellite at about 719 eV is noticeable in all shown Fe2p spectra. Considering the peak and satellite positions given in table 5.2 and the reference spectra of different iron

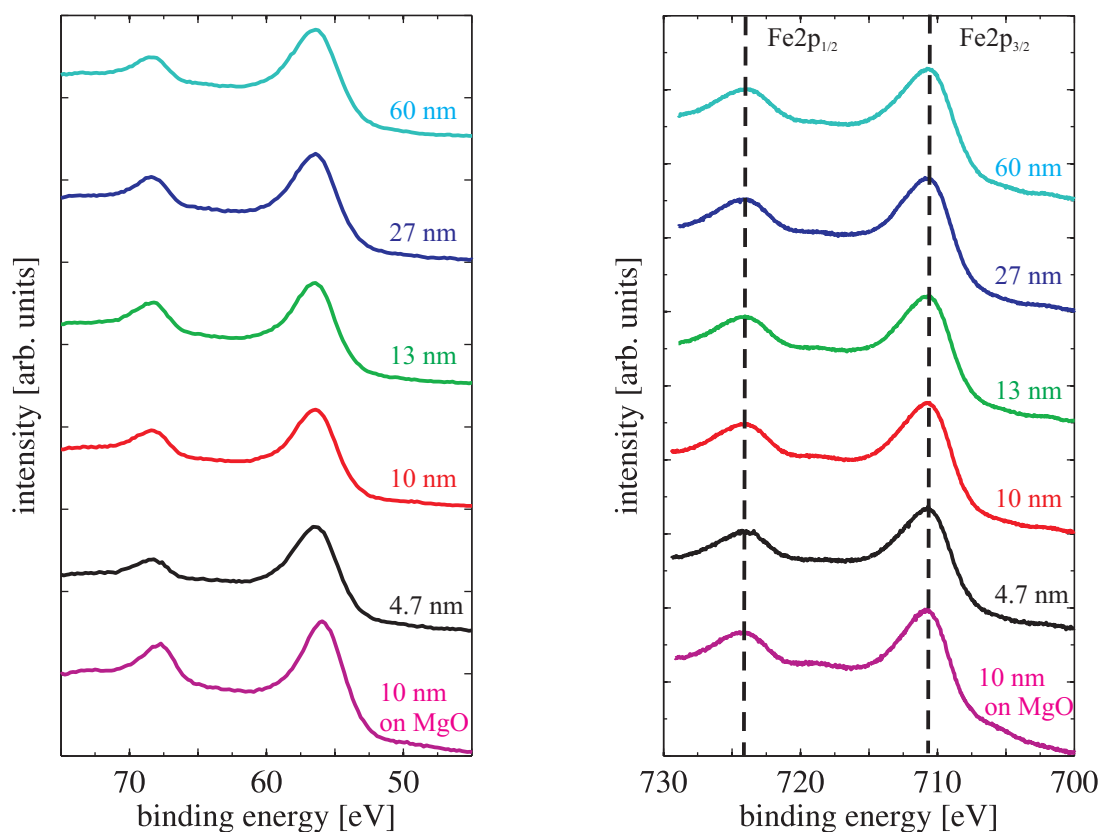


Figure 6.1.: XPS spectra of the Fe3p and Ni3p peak (on the left-hand side) and of the Fe2p peak (on the right-hand side) for nickel ferrite films on STO. From bottom to top the film thickness increases while the Ni content is between 27 % and 33 %. For comparison the respective spectrum of a nickel ferrite film with optimized Ni content grown on MgO is added. The dashed lines illustrate the peak positions of the $\text{Fe}2p_{1/2}$ and $\text{Fe}2p_{3/2}$ peak, which don't shift for different film thicknesses and are the ones for iron in the 3+ oxidation state. In all Fe2p spectra the satellite at about 719 eV, indicating Fe3+ ions, is noticeable. As the Fe2p spectra the 3p spectra show no differences for the different thicknesses.

oxides in figure 5.8 it can be confirmed that the oxidation state of the iron inside all films on STO is 3+, likewise inside the shown film on MgO. This result can be underlined by the fact that for the reconstruction of the Fe2p peak the Fe^{2+} satellite at about 714.7 eV wasn't necessary to obtain the shape of the spectra of all films on STO, whereas for the films on MgO with Ni contents lower than the optimum it was unrenounceable. Additionally to the shown spectra the Ni3s and Fe3s spectra for the films have been measured with the Al-anode. As in the case of the films on MgO the exchange splitting of both peaks has been determined. Their values, 5 ± 0.4 eV for Ni3s and 6.2 ± 0.3 eV for Fe3s, correspond with the respective values obtained for the nickel ferrite film with equivalent Ni content on MgO.

In summary, the XPS measurements confirm that the films on STO reveal the same stoichiometry and oxidation states of the cations as the optimized film on MgO.

6.2. LEED results

LEED measurements have been performed on all cleaned substrates and on every prepared film in an electron energy range of 90 eV to 220 eV in order to characterize the crystal surface structure.

The diffraction pattern for all STO(001) substrates look the same, so in figure 6.2 a) one LEED image of a STO substrate is shown exemplarily. The electron energy used for all following LEED images is 102 eV.

The LEED image of the substrate illustrates a (1×1) structure, which arises from the quadratic surface unit cell of STO. Since the diffraction spots are sharp and clearly distinguishable from the background the heated surface of the substrate is crystalline and well-ordered.

The LEED pattern of the films with different film thickness don't display large differences so in figure 6.2 b) and c) the LEED patterns of two films with a film thickness of 13 nm and 60 nm are illustrated.

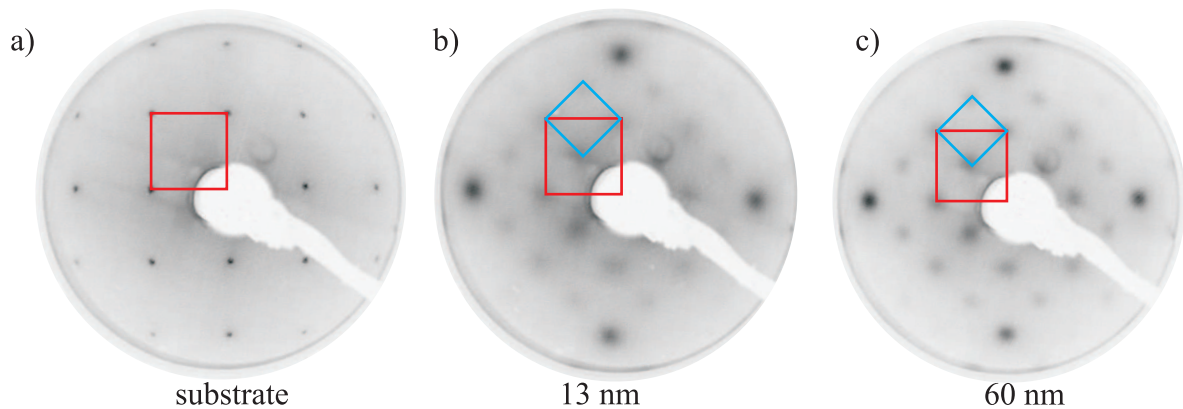


Figure 6.2.: Exemplarily LEED image of a STO(001) substrate (a) and a nickel ferrite film with a thickness of 13 nm (b) and 60 nm (c). The images are taken with an electron energy of 102 eV and in all images the quadratic unit cell of the substrate material STO is indicated (red). The LEED images of the nickel ferrite films exhibit the (1×1) structure (blue) of all iron oxides grown on STO. The surface unit cells of the substrate STO (red) and nickel ferrite (blue) are rotated against each other about 45° , consequently also visible in the LEED patterns.

All films reveal the (1×1) structure of the film material (blue) which unit cell length is 8.34 \AA in the case of stoichiometric NiFe_2O_4 . In addition, the reciprocal unit cell of the substrate material STO is indicated (red). For the reason that STO has a unit cell length of 3.9017 \AA in real space the structure of the film appears roughly half as large as the one of STO in reciprocal space, thus in the LEED image. The surface unit cells of the substrate STO (red) and nickel ferrite (blue) are rotated against each other about 45° , which is consequently visible in the LEED patterns as well. When comparing the LEED images of the two shown films it is noticeable that the diffraction spots for the thicker film are slightly sharper. This tendency is recognizable over the whole range of prepared film thicknesses. The sharper and smaller the spots, the higher is the crystalline quality of the

surface. This result indicates that the ordering of the surface increases with increasing film thickness.

6.3. XRR results

The analysis of the XRR measurements have been executed in the same manner as in chapter 5.3 with the software "iXRR" (compare reference [20]). As in the case of the films on MgO the results of the refraction indices and the roughnesses are secondary and the primary focus is on the film thickness of the prepared films. In figure 6.3 the XRR measurements and their reconstructions are presented.

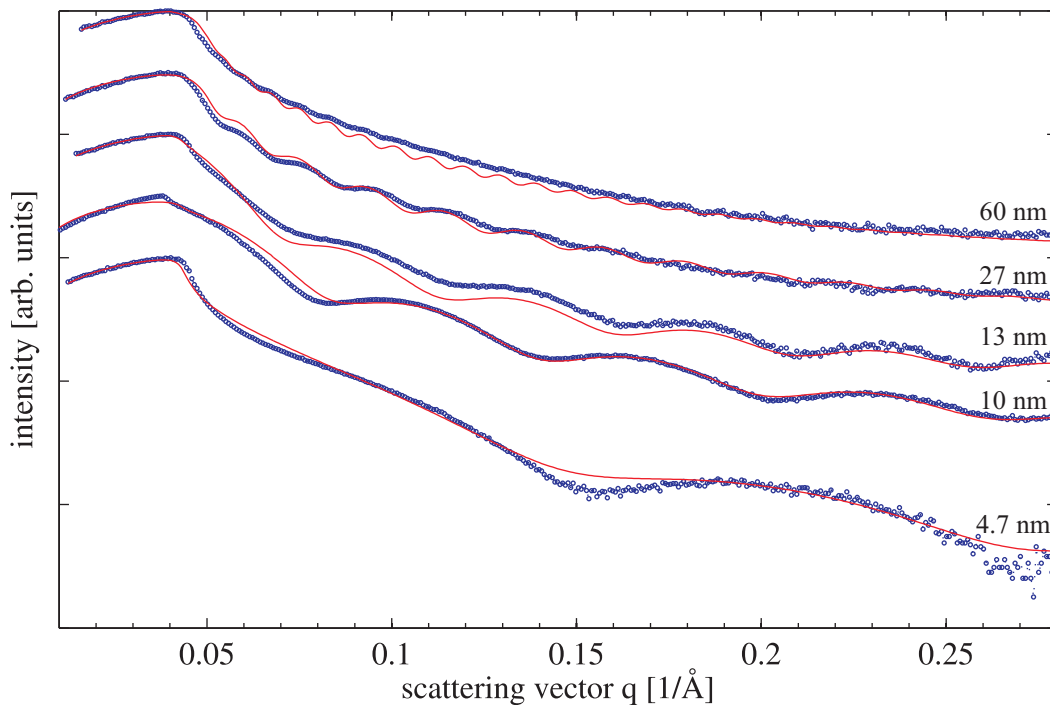


Figure 6.3.: XRR measurements and their reconstruction. The blue points indicate the measured data while the red line represents the approximation. The reconstructions coincide very well with the measured data.

The reconstructions of all films coincide very well with the measured data and the adapted values for the complex refraction index of the film on top of the substrate correspond to the literature values for nickel ferrite. The parameters of the reconstructions and the literature values for the refraction index are shown in the appendix (see A.0.2.). The film thickness d of all prepared films have already been given in tables 4.3 in chapter 4.3. The thinnest and thickest film prepared on STO reveal a thickness of 5 nm and 60 nm.

6.4. XRD results

The XRD measurements of the films on STO, performed with the diffractometer at the Universität Bielefeld, based on the 2θ -geometry, reveal the respective diffracted intensity in dependence of the incidence angle. The diffracted intensities are reconstructed with the software ReflexFit (for more information see [58]). The reconstruction consists of the substrate Bragg peak and a leftwards shifted film peak. In figure 6.4 and 6.5 the XRD results of all prepared films around the (002)- and (004)-reflexes of STO are shown with their reconstruction. From bottom to top the film thickness increases and the film peak (green) shifts to lower L values in the reciprocal space.

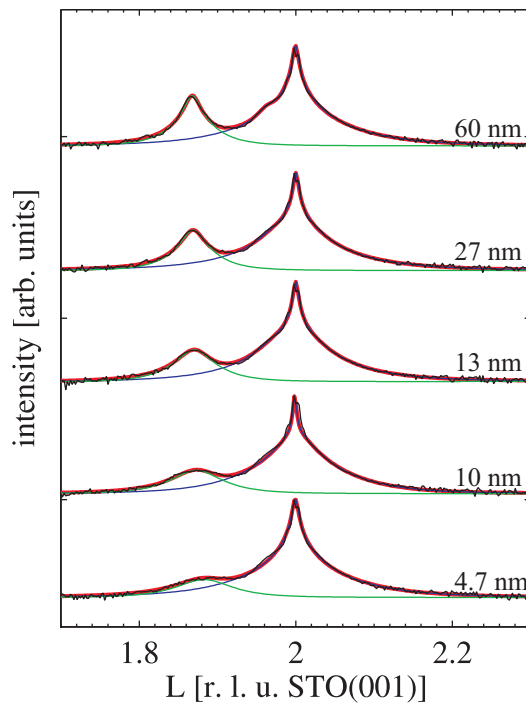


Figure 6.4.: XRD measurements of the prepared films around the (002)-reflex of STO. The measured intensities (black) are reconstructed (red) consisting of the substrate Bragg peak (blue) at $L = 2$ and the film peak (green) at about $L = 1.88$. With increasing film thickness the film peak gets more intensive and shifts to lower L values.

With increasing film thickness the intensity of the film peaks at about $L = 1.88$ and $L = 3.73$ increases. That implies that as expected the crystalline film material of the films increases with increasing film thickness d . The second noticeable feature in both illustrations is that the film peak moves to lower L values with increasing film thickness, meaning that the out-of-plane lattice constant rises with the film thickness. With equation 5.1 in chapter 5.4.2 the out-of-plane layer distance c_{film} of the film can be calculated from the positions $L_{\text{substrate}}$ and L_{film} of the substrate and film Bragg peak. The calculated out-of-plane layer distance c_{film} of the films based on the film peak at about $L = 1.88$ is depicted in figure 6.6 in dependence of the film thickness.

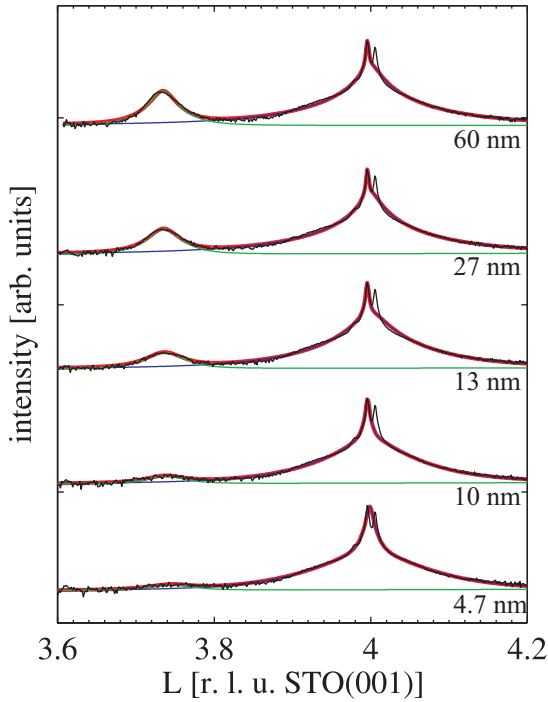


Figure 6.5.: XRD measurements of the prepared films around the (004)-reflex of STO. The measured intensities (black) are reconstructed (red) consisting of the substrate Bragg peak (blue) at $L = 4$ and the film peak (green) at about $L = 3.73$. With increasing film thickness the film peak gets more intensive and shifts to lower L values.

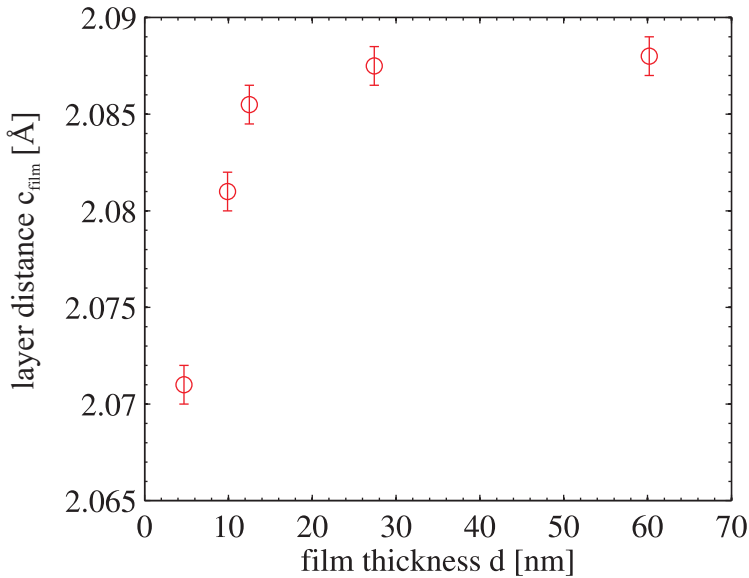


Figure 6.6.: Progression of the out-of-plane layer distance c_{film} of the films based on the film peak at about $L = 1.88$ in dependence of the film thickness d , determined by XRR measurements. The out-of-plane layer distance for a film thickness of 5 nm lies at about 2.07 Å and increases at about 2.0875 Å for a film thickness of 60 nm. At the latter the layer distance seems to flatline.

The out-of-plane layer distance increases from about 2.07 Å at a film thickness of 5 nm to 2.0875 Å at a thickness of 60 nm. At the latter value the progression seems to stagnate. The out-of-plane layer distance of nickel ferrite and STO are 2.085 Å and 1.9505 Å, respectively (compare chapter 3.1 and 3.3). Comparing these values to the obtained out-of-plane layer distances it is obvious that for low film thicknesses the nickel ferrite film is squeezed together in out-of-plane direction. With increasing film thickness the film undergoes strain relaxation and reaches the out-of-plane layer distance of 2.085 Å at a film thickness of about 13 nm. For thicker films the out-of-plane layer distance is even slightly larger than 2.085 Å. Since the films prepared on STO reveal slightly too much iron the out-of-plane

layer distance $c_{\text{Fe}_3\text{O}_4}$ of magnetite with $a_{\text{Fe}_3\text{O}_4}/4 = 2.0975 \text{ \AA}$ is taken into account. In figure 6.7 the out-of-plane layer distance c_{film} is illustrated in dependence of the Ni content x in $\text{Ni}_x\text{Fe}_{3-x}\text{O}_4$. It is simplistically assumed that the out-of-plane layer distance decreases linearly with increasing Ni content.

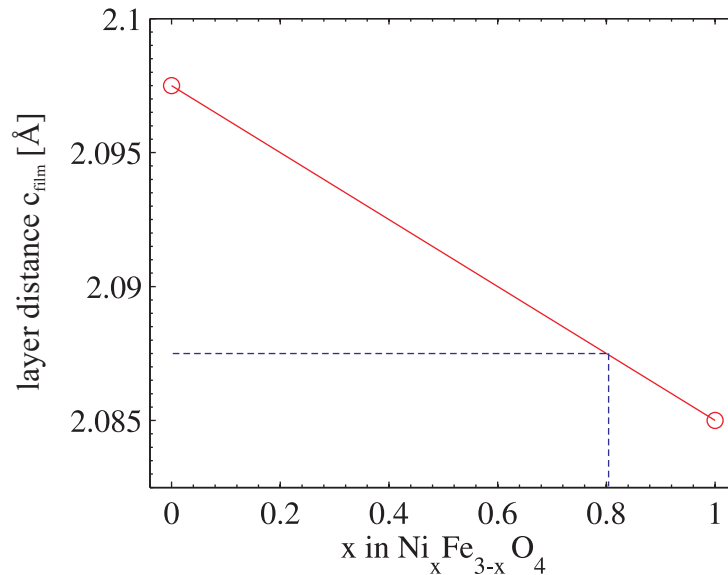


Figure 6.7.: Progression of the out-of-plane layer distance for the transition from magnetite to nickel ferrite. The dashed blue line indicates the value of the out-of-plane layer distance obtained during the XRD measurements on STO (2.0875 \AA). The lines intersect at $x = 0.8$ belonging to a $\text{Ni}/(\text{Fe}+\text{Ni})$ content of 27%.

The obtained boundary value of 2.0875 \AA for the out-of-plane layer distance intersects with the theoretical progression of the constant at $x = 0.8$ belonging to a $\text{Ni}/(\text{Fe}+\text{Ni})$ content of 27% which coincides with the value of 28% determined by the XPS measurement of the respective thickest film on STO.

In addition to the positions of the peaks the full width at half maximum (FWHM) of the film peak within the reconstructions of the XRD measurements has been analyzed in dependence of the film thickness. In all cases the film peak has been reconstructed by a Lorentz peak. Figure 6.8 displays the inverse FWHM of the film peak next to the (002)- and (004)- substrate Bragg peak for the five films on STO with different film thickness.

With increasing film thickness d the inverse FWHM increases non-linearly, indicating that the crystalline part of the film rises, since $d_{\text{crys}} \propto 1/\text{FWHM}$. The lower the FWHM, the narrower is the distribution of the out-of-plane layer distance c_{film} , meaning the better the crystalline order in out-of-plane direction. According to the FWHM the crystalline order of the nickel ferrite films on STO in out-of-plane direction increases with rising film thickness.

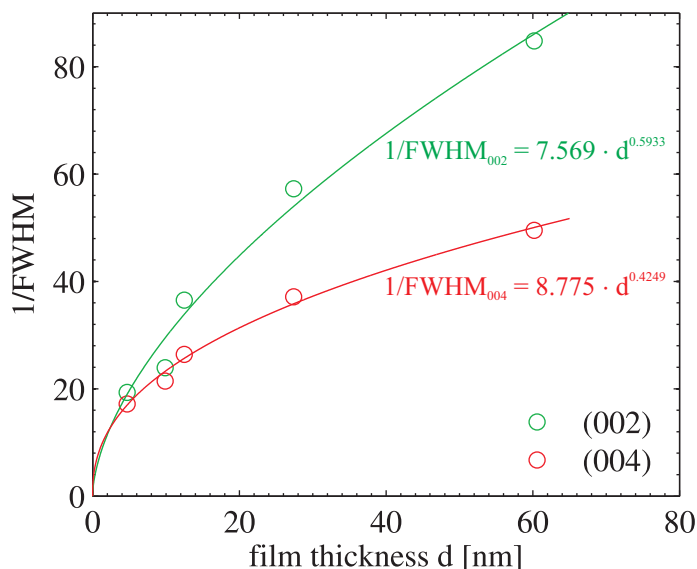


Figure 6.8.: Inverse FWHM of the film peak next to the (002)- and (004)- substrate Bragg peak in dependence of the film thickness d . With increasing film thickness d the inverse FWHM increases, meaning that the FWHM decreases. The progression is a non-linear relation.

6.5. Discussion

The results obtained from all performed measurements are discussed in this chapter.

The XPS measurements confirm the stoichiometry and the oxidation states of the cations of the nickel ferrite films on STO as observed for the optimized films on MgO. The Ni3p and Fe3p peaks don't vary for the five films and reveal Ni contents between 27 % and 33 %. The Fe2p_{1/2} and Fe2p_{3/2} peaks of all films are located at 724.4 ± 0.3 eV and 710.8 ± 0.3 eV and the satellite at about 719 eV, attributed to Fe³⁺ ions, is recognizable in all spectra (compare figure 6.1) with the result that the oxidation state of the iron is 3+ [30]. For the reconstruction of the Fe2p spectra the satellite located at about 714.7 eV, arising from Fe²⁺ ions, isn't necessary to obtain the correct shape, thereby underlining the 3+ oxidation state.

As expected the LEED images of all films exhibit a (1×1) structure which unit cell is rotated around 45° and which length is roughly halved with respect to the reciprocal MgO surface unit cell. With increasing film thickness the sharpness of the reflexes increases, indicating a rising order of the atoms at the surface with increasing film thickness.

The XRR measurements have all been reconstructed by one single layer with the refraction indices for nickel ferrite [53] and the obtained film thicknesses reach from 4.7 nm up to 60 nm.

The results obtained from the XRD measurements are unexpected. For the reason that the lattice constant of nickel ferrite is more than two times larger than the one of STO one would expect pseudomorphic growth of nickel ferrite on STO with a compression in in-plane and tensile stress in out-of-plane direction in order to compensate the compression

arising from the lattice mismatch. In contrast, the layer distance in out-of-plane direction is compressed. That means that the pseudomorphic growth has to be questioned. The layer distance in out-of-plane direction increases with increasing film thickness (compare figure 6.6). The thinnest film of about 5 nm shows a layer distance of about 2.07 Å. At a film thickness of about 13 nm the literature value of the layer distance with 2.085 Å is obtained. For the prepared film of 60 nm the layer distance even reaches a value of 2.0875 Å. At this point the progression seems to stagnate. Keeping in mind that the films on STO exhibit on average slightly too much iron relativizes this value. The layer distance of magnetite is slightly larger than the one of nickel ferrite. Expecting a linear progression with increasing Ni content between these two values the measured layer distance for the film of 60 nm belongs to a Ni content of 27% which is in great accordance with the obtained value of 28% through the XPS analysis (compare figure 6.7) and explains the slightly larger layer distance.

According to the measured out-of-plane layer distance nickel ferrite doesn't grow pseudomorphically on STO but rather is compressed in out-of-plane direction. Hoppe et al. and Lüders et al. report the same behaviour of the out-of-plane lattice distance of nickel ferrite films grown on STO by pulsed laser deposition and rf sputtering [15], [59]. While Hoppe et al. claim auxetic behaviour of nickel ferrite due to the compressed out-of-plane lattice distance in combination with the expected in-plane compression caused by pseudomorphic growth Lüders et al. indeed show measurements concerning the in-plane layer distance. Unfortunately, the inaccuracy of measurement is so high that the in-plane layer distance could be either compressed or tensile strained. Again a comparison is drawn to the quite similar $\text{Fe}_3\text{O}_4/\text{STO}$ system due to the rarely number of studies concerning nickel ferrite thin films. Schuckmann et al. obtained both in-plane and out-of-plane layer distances for the growth of Fe_3O_4 on STO and also report about a compression of the films in out-of-plane direction which is accompanied by tensile strain in in-plane layer direction [56]. Both layer distances relax with increasing film thickness but even at a thickness of 120 nm the films are still partly strained in both directions. This result suggests that the Fe_3O_4 doesn't grow pseudomorphically on STO but rather is tensile strained in in-plane direction and thereby doesn't show auxetic behaviour which fits to the positive Poisson ratio reported for Fe_3O_4 . This result enables the large possibility that nickel ferrite on STO behaves in the same manner, since its Poisson ratio is positive too [52]. The analysis of the in-plane layer distance is the next step within further investigations.

The analysis of the FWHM of the film peaks next to the substrate Bragg (002)- and (004)-reflexes reveals a non-linear rise of the inverse $\text{FWHM} \propto d_{\text{crys}}$ with rising film thickness, implying an enhancement of the crystalline order in out-of-plane direction with increasing film thickness. This observation is plausible, since the films relax more and more with increasing film thickness so that with rising film thickness evermore film material is deposited with the same out-of-plane layer distance and the distribution of the out-of-plane layer distance narrows within this progression.

Recapitulatory, one can conclude that the nickel ferrite films prepared on STO behave structurally in the same manner as the related magnetite films. The relaxation of the films in out-of-plane direction with increasing film thickness is reasonable. For both Fe_3O_4 and NiFe_2O_4 on STO the reason for the probably non-pseudomorphic growth and in-plane tensile strain and observed matching out-of-plane compression has to be found.

Several further investigations concerning the structure in in-plane and out-of-plane direction have to be done in order to explain the unexpected observed behaviour. In order to compare the applicability and quality of the nickel ferrite films prepared by RMBE to other deposition techniques, measurements concerning the magnetic (VSM) and electric properties of the films are essential. Especially the magnetic properties for film thicknesses in the range of monolayers reveal great scientific interest, since the saturation magnetization is supposed to be distinctly higher compared to the bulk material [59], [60].

Although the LEED measurements already showed a well structured surface, image-generating techniques like AFM and TEM would be desirable to get more detailed information.

In contrast to the preparation on MgO, so far no statement concerning the absolute value of the crystalline film thickness d_{crys} could be made. Therefore, the high resolution of synchrotron radiation is necessary.

7. Conclusion

The subject matter of this thesis is the investigation of the growth of ultrathin $\text{Ni}_x\text{Fe}_{3-x}\text{O}_4$ ($0 < x < 1$) films on $\text{MgO}(001)$ in order to find the growth parameters for the deposition of stoichiometric nickel ferrite (NiFe_2O_4). The growth of stoichiometric nickel ferrite with different film thicknesses on $\text{SrTiO}_3(001)$ is the second emphasis of the current thesis.

The used method is the co-evaporation of nickel and iron with reactive molecular beam epitaxy in an oxygen atmosphere of 5×10^{-6} mbar and a substrate temperature of 250°C . The $\text{Ni}/(\text{Fe}+\text{Ni})$ ratio is varied by adjusting the electrical power of the two effusion cells. In total, fifteen films on MgO with $\text{Ni}/(\text{Fe}+\text{Ni})$ ratios between 7 % and 60 % and five films on SrTiO_3 with $\text{Ni}/(\text{Fe}+\text{Ni})$ ratios between 27 % and 33 % and film thicknesses between 5 and 60 nm are prepared. For each film LEED, XPS, XRR and XRD measurements are performed. The XRR measurements only serve as determination of the film thickness.

The LEED measurements of all films exhibit a sharp (1×1) diffraction pattern so the crystalline quality of all films is pretty good at the surface. For the films grown on SrTiO_3 the sharpness of the reflexes and thereby the ordering at the surface increases with rising film thickness.

For the growth of the $\text{Ni}_x\text{Fe}_{3-x}\text{O}_4$ ($0 < x < 1$) films on MgO the XPS measurements have priority since the analysis of the $\text{Fe}3p$ and $\text{Ni}3p$ peaks supply the $\text{Ni}/(\text{Fe}+\text{Ni})$ ratio and the $\text{Fe}2p$, $\text{Ni}3s$ and $\text{Fe}3s$ spectra reveal information about the oxidation states of iron and nickel within the film. Above a $\text{Ni}/(\text{Fe}+\text{Ni})$ ratio of 32 % the results confirm that iron exists purely in the 3+ oxidation state, as it should be in stoichiometric nickel ferrite. Below that ratio iron exists in the 3+ and 2+ oxidation states like in the structural identical iron oxide magnetite. The oxidation state of nickel (2+) doesn't change with varying $\text{Ni}/(\text{Fe}+\text{Ni})$ ratio.

According to the XRD and XRR measurements of three films with a $\text{Ni}/(\text{Fe}+\text{Ni})$ ratio between 53 % and 60 % the films consist of a single, completely crystalline layer and the out-of-plane layer distance is with 2.07 \AA about 0.7 % smaller than the bulk layer distance of 2.085 \AA [1]. This compression in out-of-plane direction goes along with the lattice mismatch of 1 % existing between the two materials and leading to tensile strain for the non-auxetic nickel ferrite in in-plane direction.

For the films grown on SrTiO_3 the XPS results verify the presence of iron in the pure 3+ oxidation state. For the reason of the relatively large lattice mismatch of -7 % between the two materials the XRD results for the different film thicknesses are the focus. Based on the lattice mismatch one would assume pseudomorphic growth of the films with a compression in in-plane direction and in compensation tensile strain in out-of-plane direction. Against these assumptions the XRD results expose a compression in out-of-plane direction for thin films and call the pseudomorphic growth of the films on SrTiO_3 in question. At a film thickness of 5 nm the positions of the film Bragg peaks lead to a layer distance in out-of-plane direction of 2.07 \AA which increases up to 2.0875 \AA at a

film thickness of 60 nm. Consequently, the out-of-plane layer distance of the 60 nm film is even slightly larger than the bulk value of 2.085 Å which can be explained by the fact that the Ni/(Fe+Ni) ratio is 28 % and thereby the composition is shifted towards the iron oxide magnetite with the according out-of-plane layer distance of 2.0975 Å. In addition to the film thickness dependent layer distance the FWHM of the film Bragg peaks is analyzed. It decreases non-linearly with increasing film thickness and thereby indicates that the distribution of the out-of-plane lattice constant narrows so the crystallinity in out-of-plane direction rises with increasing film thickness.

The further approach is to prepare nickel ferrite films on SrTiO₃ with film thicknesses below 5 nm and to perform XRD and also grazing incidence XRD measurements of all prepared film thicknesses at a synchrotron in order to collect information about the structure in in-plane and out-of-plane direction. The next focus is going to be the characterization of the magnetic properties of all films. Furthermore, investigations concerning the electrical conductance, the morphology and the interface properties of all prepared films are necessary to compare the quality of the films prepared by RMBE to other deposition techniques. Therefore, the performance of VSM, AFM and TEM is convenient.

Bibliography

- [1] X. W. Li, A. Gupta, G. Xiao, W. Qian, V. P. Dravid. *Fabrication and properties of heteroepitaxial magnetite (Fe_3O_4) tunnel junctions*. Applied Physics Letters **73** (22), 3282 (1998).
- [2] N. W. Ashcroft, N. D. Mermin. *Solid State Physics*. Saunders College (1976).
- [3] K. Uchida, J. Xiao, H. Adachi, J. Ohe, S. Takahashi, J. Ieda, T. Ota, Y. Kajiwara, U. Umezawa, H. Kawai, G. E. W. Bauer, S. Maekawa, E. Saitoh. *Spin Seebeck insulator*. Nature Materials **9**, 894–897 (2010).
- [4] K. Uchida, S. Takahashi, K. Harii, J. Ieda, W. Koshibae, K. Ando, S. Maekawa, E. Saitoh. *Observation of the spin Seebeck effect*. Nature **455**, 778–781 (2008).
- [5] J. Xiao, G. E. W. Bauer, K. Uchida, E. Saitoh, S. Maekawa. *Theory of magnon-driven spin Seebeck effect*. Physical Review B **81** (2010).
- [6] K. Uchida, H. Adachi, T. Kikkawa, A. Kirihara, M. Ishida, S. Yorozu, S. Maekawa, E. Saitoh. *Thermoelectric generation based on spin Seebeck effects*. Condensed Matter Physics **arXiv:1604.00477** (2016).
- [7] H. Adachi, K. Uchida, E. Saitoh, S. Maekawa. *Theory of the spin Seebeck effect*. Reports on Progress in Physics **76** (2013).
- [8] V. A. M. Brabers. *Handbook of Magnetic Materials*. Elsevier, Amsterdam (1995).
- [9] G. Dixit, J. P. Singh, R.C. Srivastava, H. M. Agrawal, R. J. Choudhary, A. Gupta. *Annealing effect on the structural and magnetic properties of nickel ferrite thin films*. Surf. Interface Anal. **42**, 151–156 (2010).
- [10] C. Dong, G. Wang, D. Guo, C. Jiang, D. Xue. *Growth, structure, morphology, and magnetic properties of Ni ferrite films*. Nanoscale Research Letters **8** (2013).
- [11] J. L. Gunjekar, A. M. More, K. V. Gurav, C. D. Lokhande. *Chemical synthesis of spinel nickel ferrite ($NiFe_2O_4$) nano-sheets*. Applied Surface Science **254**, 5844–5848 (2008).
- [12] G. Caruntu, I. Dumitru, G. G. Bush, D. Caruntu, C. J. O'Connor. *Magnetic characterization of nanocrystalline nickel ferrite films processed by a spin-spraying method*. Journal of Physics D: Applied Physics **38**, 811–815 (2005).
- [13] H. Itoh, T. Takeda, S. Naka. *Preparation of nickel and Ni-Zn ferrite films by thermal decomposition of metal acetylacetonates*. Journal of Materials Science **21**, 3677–3680 (1986).
- [14] F. Bertram. *Röntgenstrukturanalyse von Oxidschichten*. Masterarbeit, Universität Osnabrück (2009).

- [15] M. Hoppe, S. Döring, M. Gorgoi, S. Cramm, M. Müller. *Enhanced ferrimagnetism in auxetic $NiFe_2O_4$ in the crossover to the ultrathin-film limit*. Physical Review B **91** (2015).
- [16] C. Kittel. *Introduction to Solid State Physics*. John Wiley & Sons, Inc (2005).
- [17] S. Hunklinger. *Festkörperphysik*. De Gruyter (2014).
- [18] K. Oura, V. G. Lifshits, A. A. Saranin, A. V. Zotov, M. Katayama. *Surface Science - An Introduction*. Springer-Verlag Berlin Heidelberg (2003).
- [19] L. G. Parratt. *Surface Studies of Solids by Total Reflection of X-Rays*. Physical Review **95**, 359 (1954).
- [20] F. Bertram. *Röntgenreflektometrie an ultradünnen Schichten*. Bachelorarbeit, Universität Osnabrück (2007).
- [21] L. Spieß, G. Teichert, R. Schwarzer, H. Behnken, C. Genzel. *Moderne Röntgenbeugung - Röntgendiffraktometrie für Materialwissenschaftler, Physiker und Chemiker*. Vieweg + Teubner | GWV Fachverlage GmbH, Wiesbaden (2009).
- [22] W. Demtröder. *Experimentalphysik 2 - Elektrizität und Optik*. Springer-Verlag Berlin Heidelberg (2006).
- [23] O. Schuckmann. *Plasmamodifizierung von Praseodym- und Ceroxidschichten*. Masterarbeit, Universität Osnabrück (2012).
- [24] H. Lüth. *Solid Surfaces, Interfaces and Thin Films*. Springer-Verlag Berlin Heidelberg (2010).
- [25] R. Buss. *Studies on the Epitaxial Growth of Ultrathin Metal Oxide Films*. Universität Osnabrück, 2015.
- [26] D. A. Shirley. *High-resolution x-ray photoemission spectrum of the valence bands of gold*. Physical Review B **5**, 4709 – 4714 (1972).
- [27] S. Tanuma, C. J. Powell, D. R. Penn. *Calculations of Electron Inelastic Mean Free Paths for 31 Materials*. Surface and Interface Analysis **11**, 577–589 (1988).
- [28] M. P. Seah, W. A. Dench. *Quantitative Electron Spectroscopy of Surfaces: A Standard Data Base for Electron Inelastic Mean Free Paths in Solids*. Surface and Interface Analysis **1** (1979).
- [29] S. Tanuma, C. J. Powell, D. R. Penn. *Calculation of electron inelastic mean free paths (IMFPs) VII. Reliability of the TPP-2M IMFP predictive equation*. Surface and Interface Analysis **35**, 268–275 (2002).
- [30] T. Yamashita, P. Hayes. *Analysis of XPS spectra of Fe^{2+} and Fe^{3+} ions in oxide materials*. Applied Surface Science **254**, 2441–2449 (2008).
- [31] S. Hüfner, G. K. Wertheim. *Systematics of core line asymmetries in XPS spectra of Ni*. Physics Letters **51A**, 301–303 (1975).
- [32] J. H. Van Vleck. *The Dirac Vector Model in Complex Spectra*. Physical Review **45**, 405–419 (1934).

-
- [33] V. R. Galakhov, M. Demeter, S. Bartkowski, M. Neumann, N. A. Ovechkina, E. Z. Kurmaev, N. I. Lobachevskaya, Ya. M. Mukovskii, J. Mitchell, D. L. Ederer. *Mn 3s exchange splitting in mixed-valence manganites*. Physical Review B **65** (2002).
- [34] V. R. Galakhov, S. Uhlenbrock, S. Bartkowski, A V. Postnikov, M. Neumann, L. D. Finkelstein, E. Z. Kurmaev, A. A. Samokhvalov, L. I. Leonyuk. *X-ray photoelectron 3s spectra of transition metal oxides*. arXiv:cond-mat/9903354 (1999).
- [35] G. C. Allen, M. T. Curtis, A. J. Hooper, P. M. Tucker. *X-ray Photoelectron Spectroscopy of Iron-Oxygen Systems*. Journal of the Chemical Society, Dalton Transactions **14**, 1525–1530 (1974).
- [36] J. C. Vickerman, S. Gilmore. *Surface Analysis - The Principal Techniques*. John Wiley & Sons Ltd (2009).
- [37] W. Spiess. *Synchrotronbasierte XRD Untersuchungen zur Epitaxie von ultradünnen Magnetitschichten auf reinen und NiO bedeckten SrTiO₃(001) Kristallen*. Universität Osnabrück, 2015.
- [38] J. Rodewald. *Oxidation epitaktischer Eisenschichten auf Ag(001)*. Universität Osnabrück, 2014.
- [39] R. Gross, A. Marx. *Festkörperphysik*. Oldenbourg Wissenschaftsverlag GmbH (2012).
- [40] M. Klaua, D. Ullmann, J. Barthel, W. Wulfhekel, J. Kirschner, R. Urban, T. L. Monchesky, A. Enders, J. F. Chochran, B. Heinrich. *Growth, structure, electronic, and magnetic properties of Mg/Fe(001) bilayers and Fe/MgO/Fe(001) trilayers*. Physical Review B **64**, 134411 (2001).
- [41] Y. A. Abramov, V. G. Tsirelson, V. E. Zavodnik, S. A. Ivanov, I. D. Brown. *The chemical bond and atomic displacements in SrTiO₃ from X-ray diffraction analysis*. Acta crystallographica Section B, Structural science **51(6)**, 942–951 (1995).
- [42] <http://www.emg.ing.tu-bs.de/bilder/forschung/material/srtio3.png>, 24.06.2016. .
- [43] K. van Benthem, C. Elsässer, R. H. French. *Bulk electronic structure of SrTiO₃: Experiment and theory*. Journal of Applied Physics **90(12)**, 6156–6164 (2001).
- [44] O. H. Seeck, C. Deiter, K. Pflaum, F. Bertram, A. Beerlink, H. Franz, J. Horbach, H. Schulte-Schrepping, B. M. Murphy, M. Greve, O. Magnussen. *The high-resolution diffraction beamline P08 at PETRA III*. Journal of Synchrotron Radiation **19**, 30–38 (2012).
- [45] B. Zimmermann. *Epitaktisches Wachstum und Charakterisierung ultradünner Eisenoxidschichten auf Magnesiumoxid (001)*. Dissertation, Universität Osnabrück (2010).
- [46] N. S. McIntyre, G. D. G. Zetaruk. *X-ray Photoelectron Spectroscopic Studies of Iron Oxides*. Analytical Chemistry **49**, 1521–1529 (1977).
- [47] J. H. Scofield. *Hartree-Slater subshell photoionization cross-sections at 1254 and 1487 eV*. Journal of Electron Spectroscopy and Related Phenomena **8**, 129–137 (1976).
- [48] S. Uhlenbrock. *Untersuchungen zur elektronischen Struktur einfacher Übergangsmetall-Oxide unter besonderer Berücksichtigung des Nickel-Oxids*. Dissertation, Universität Osnabrück (1994).
-

- [49] K. C. Prince, M. Matteucci, K. Kuepper, S. G. Chiuzaian, S. Bartkowski, M. Neumann. *Core-level spectroscopic study of FeO and FeS₂*. Physical Review B **71**, 085102–1–085102–9 (2005).
- [50] B. Stanka, W. Hebenstreita, U. Diebold, S. A. Chambers. *Surface reconstruction of Fe₃O₄(001)*. Surface Science **448**, 49–63 (2000).
- [51] A. Greuling. *Röntgenstrukturanalyse von Isolatorschichten*. Universität Osnabrück, 2007.
- [52] S. S. Yattinahalli, S. B. Kapatkar, S. N. Mathad. *Structural and Mechanical Properties of a Nano Ferrite*. Advanced Science Focus **2**, 42–46 (2014).
- [53] B. L. Henke, E. M. Gullikson, J. C. Davis. *X-ray interactions: photoabsorption, scattering, transmission, and reflection at E=50-30000 eV, Z=1-92*. Atomic Data and Nuclear Data Tables **54 (2)**, 181–342 (1993).
- [54] J. W. Matthews, A. E. Blakeslee. *Defects in epitaxial Multilayers*. Journal of Crystal Growth **27**, 118–125 (1974).
- [55] S. K. Arora, R. G. S. Sofin, I. V. Shvets. *Anomalous strain relaxation behavior of Fe₃O₄ /MgO (100) heteroepitaxial system grown using molecular beam epitaxy*. Journal of Applied Physics **100** (2006).
- [56] O. Schuckmann, T. Schemme, N. Pathé, F. Timmer, F. Bertram, T. Kuschel, O. Gutowsky, U. Rütt, J. Wollschläger. *HESXRD studies on ultrathin magnetite films grown on Nb doped SrTiO₃ (001)*. Technical report Deutsches Elektronen Synchrotron (2013).
- [57] O. Kuschel, R. Buß, W. Spiess, T. Schemme, J. Wöllermann, K. Balinski, T. Kuschel, A. T. D’Diaye, J. Wollschläger, K. Kuepper. *From Fe₃O₄/NiO bilayers to NiFe₂O₄-like thin films through Ni interdiffusion*. Physical Review B **94** (2016).
- [58] S. Gevers. *SPA-LEED-Untersuchungen von Praseodymoxidschichten auf Si(111)-Substraten*. Diplomarbeit, Universität Osnabrück (2007).
- [59] U. Lüders, M. Bibes, J.F. Bobo, M. Cantoni, R. Bertacco, J. Fontcuberta. *Enhanced magnetic moment and conductive behavior in NiFe₂O₄ spinel ultrathin films*. Physical Review B **71** (2005).
- [60] S. Venzke, R. B. van Dover, J. M. Phillips, E. M. Gyorgy, t. Siegrist, C.-H. Chen, D. Werder, R. M. Fleming, R. J. Felder, E. Coleman, R. Opila. *Epitaxial growth and magnetic behavior of NiFe₂O₄ thin films*. Journal of Materials Research **11**, 1187–1198 (1996).

A. Appendix

A.0.1. XRR data NiFe₂O₄ on MgO

sample	σ_s [Å]	δ_{film} [10^{-5}]	$\delta/\beta_{\text{film}}$	d [Å]	σ_{film} [Å]
A	15.8	1.645	19.79	389.5	2.36
B	8.93	1.613	13.75	359.01	6.61
C	15	1.605	16.35	305.49	15
D	6.91	1.528	9.59	281.28	8.57
E	22.13	1.726	10	342	0
G	5.32	1.623	12.4	96.03	1.21
I	3.53	1.607	18.31	57.02	3.20
K	3.38	1.684	8.39	100.53	0
L	7.39	1.734	10	132.4	2.77
M	10	1.763	8	162.85	1.97
N	11.05	1.614	10.22	160.73	3.65
O	7	1.700	8.01	138.87	0
P	5.00	1.635	14.16	177.50	1.41

Table A.1.: Parameters of the XRR reconstruction. σ_s and σ_{film} are the roughnesses of the substrate and the film, δ_{film} the dispersion of the film, $\delta/\beta_{\text{film}}$ the ratio of the dispersion and the absorption of the film and d the film thickness.

A.0.2. XRR data NiFe₂O₄ on STO

sample	σ_s [Å]	δ_{film} [10^{-5}]	$\delta/\beta_{\text{film}}$	d [Å]	σ_{film} [Å]
Q	0	1.514	8.02	46.92	7.84
R	5.62	1.673	13.92	95.85	1.29
S	0	1.378	34.27	123.06	0
T	7.8	1.371	27.7	274.4	2.05
U	2.3	1.423	15.66	602.09	1.66

Table A.2.: Parameters of the XRR reconstruction. σ_s and σ_{film} are the roughnesses of the substrate and the film, δ_{film} the dispersion of the film, $\delta/\beta_{\text{film}}$ the ratio of the dispersion and the absorption of the film and d the film thickness.

NFO:

$$\delta = 1.60 \cdot 10^{-5}$$

$$\delta/\beta = 10.9$$

[53]

Ich versichere, dass ich die eingereichte Masterarbeit selbstständig und ohne unerlaubte Hilfe verfasst habe. Anderer als der von mir angegebenen Hilfsmittel und Schriften habe ich mich nicht bedient. Alle wörtlich oder sinngemäß den Schriften anderer Autoren entnommenen Stellen habe ich kenntlich gemacht.

Osnabrück, 20. Oktober 2016

Tabea Nordmann

Danksagung

An dieser Stelle möchte ich mich bei all den Menschen bedanken, die mich bei der Erstellung dieser Masterarbeit unterstützt haben.

Ein großer Dank gilt Prof. Dr. Wollschläger für die Möglichkeit in seiner Arbeitsgruppe "Dünne Schichten und Grenzflächen" diese Arbeit anzufertigen und der immer ein offenes Ohr für mich hatte und mit seiner lockeren Art immer wieder zum Lachen gebracht hat. Außerdem bedanke ich mich bei Herrn Dr. Karsten Küpper, der die Position des Zweitgutachters übernommen hat.

Besonders möchte ich mich bei meinem Betreuer Jari Rodewald für die große Hilfe bei allen experimentellen und auswertungsbezogenen Fragen, für die vielen ideenreichen Diskussionen sowie das aufmerksame Korrekturlesen dieser Arbeit bedanken. Ebenfalls für das Korrekturlesen geht ein großes Dankeschön an Jan Beinke.

Vielen Dank an die restlichen Mitglieder der Arbeitsgruppe für die Hilfsbereitschaft, die angenehme Arbeitsatmosphäre sowie die vielen netten Gespräche zwischendurch. Bei Kristina Sprenger und Kevin Ruwisch möchte ich mich für die zahlreichen gemeinsamen, produktiven Stunden und die gelungenen Ablenkungen zwischendurch bedanken.

Ein herzlicher Dank geht an meine Familie, die mir immer fürsorglich zur Seite steht. Zuletzt möchte ich meinem Freund Daniel danken, der mich immer unterstützt und in jeder Situation die richtigen Worte findet.